

DARK MATTER CHARACTERISATION FROM X-RAY OBSERVATIONS



A thesis submitted for the degree of
Doctor of Philosophy (PhD)
August 26, 2009

Signe Riemer-Sørensen
Supervisor: Kristian Pedersen
Co-supervisor: Steen H. Hansen

Dark Cosmology Centre, Niels Bohr Institute
Faculty of Science, University of Copenhagen

ABSTRACT

The observational evidence that dark matter comprises most of the mass in the Universe is strong, but its nature remains a mystery. In this thesis two different approaches have been followed to characterise the dark matter:

i) Using X-ray observations of dark matter dense regions in various astrophysical objects, the dark matter emission has been constrained in general. For specific candidates such as sterile neutrinos and axions the emission constraints have been converted to constraints in the characterising parameter space.

ii) The validity of basic assumptions made when deriving the mass of galaxy clusters from X-ray observations have been tested. In the specific case of Abell 1689, high quality data allowed for the identification and exclusion of substructure improving the agreement between the mass profiles obtained from X-ray and gravitational lensing analyses.



Signe Riemer-Sørensen

August 26, 2009

Dark Cosmology Centre, Niels Bohr Institute, University of Copenhagen

CONTENTS

Abstract	i
Contents	iii
Abbreviations and acronyms	vii
Summary	ix
Dansk resumé	xi
1 Basic cosmology and dark matter	1
1.1 Λ CDM	1
1.2 Dark matter	3
1.2.1 Required properties of dark matter	4
1.2.2 Candidates	5
1.2.3 Direct detection	5
1.2.4 Indirect detection	6
1.2.5 The NFW-profile	7
2 X-ray observations	9
2.1 X-ray observatories	9
2.2 Chandra details	10
2.2.1 Telemetry modes	11
2.2.2 Gratings	11
2.3 Analysis of X-ray Data	12
2.3.1 Tools	12
2.3.2 The raw data and reprocessing	12
2.3.3 Bad pixels, good time intervals and point source removal	13
2.3.4 Instrumental response	14
2.3.5 Extracting spectra and instrumental response files	15
2.3.6 Background subtraction	15
2.3.7 Spectral model comparison	16
3 Sterile neutrinos	17
3.1 Cold, hot, and warm dark matter	17
3.2 Theory of sterile neutrinos	19
3.2.1 The Standard Model of particle physics	19
3.2.2 Standard model neutrino physics	20
3.2.3 Sterile neutrinos	20
3.2.4 ν MSM and neutrino masses	21

3.2.5	Two-type neutrino mixing	22
3.3	Observational signatures	23
3.3.1	Radiative decay	23
3.3.2	Sterile neutrino dark matter mass	24
3.3.3	Constraining the decay rate from emitted photons	24
3.3.4	Lyman α constraints	25
3.4	Different scenarios and their constraints	26
3.4.1	Line emission constraints	26
3.4.2	Oscillations - The Dodelson-Widrow scenario	26
3.4.3	Resonant production	27
3.4.4	Production at the electro-weak scale	28
3.4.5	Alternative scenarios	29
4	Observational constraints on sterile neutrinos	31
4.1	Line emission	31
4.1.1	Distinguishing between emission lines origins	31
4.2	The Milky Way dark matter halo	33
4.2.1	Blank sky data	33
4.2.2	Model fitting and line flux determination	34
4.2.3	Observed halo mass and mean distance	35
4.2.4	Decay rate of sterile neutrinos in the Milky Way halo	35
4.2.5	Comparing data and model	36
4.2.6	Other constraints	36
4.2.7	Conclusions on Milky Way halo constraints	38
4.3	The dark matter blob of Abell 520	38
4.3.1	The spectrum of Abell 520	38
4.3.2	Flux determination	38
4.3.3	Background subtraction	40
4.3.4	Mass of the blob	41
4.3.5	Decay rate	41
4.3.6	Constraining mass and mixing angle	42
4.3.7	Conclusions from Abell 520	42
4.4	Why it is difficult to use gratings	43
4.4.1	The generic example cluster Abell 1835	43
4.4.2	Grating observations	43
4.4.3	Conclusions on gratings	44
4.5	First constraints from the Draco dwarf galaxy	44
4.5.1	X-ray analysis	45
4.5.2	Observed mass	48
4.5.3	Results	48
4.5.4	Future observations?	49
4.5.5	Summary	50
4.6	Possible improvements on line constraints	50
5	Solar axions as dark matter	51
5.1	Axions	51
5.1.1	Peccei-Quinn axions	51
5.1.2	Kaluza-Klein axions	52
5.1.3	Solar axions	53

5.2	Data analysis	54
5.3	Masses of the regions	56
5.4	Lifetimes	56
5.5	Comparing to the model	56
5.6	Summary	57
6	Clusters of galaxies	59
6.1	Clusters of galaxies and their properties	59
6.2	Cluster mass	59
6.3	Determination of gas properties	60
6.4	From observation to mass	61
6.5	Other observational methods	61
6.5.1	Gravitational lensing	61
6.5.2	Sunyaev-Zel'dovich effect	62
7	The discrepancy between lensing and X-ray mass estimates of Abell 1689	63
7.1	Motivation	63
7.1.1	Data	64
7.2	X-rays	65
7.2.1	X-ray observations	65
7.2.2	X-ray image and surface brightness	65
7.2.3	Background	66
7.2.4	Hardness ratio maps	66
7.2.5	Temperature profile	68
7.2.6	X-ray mass profile	69
7.2.7	NFW fit and projection	70
7.2.8	Investigations of the NE region	71
7.2.9	Discussion of X-ray results	71
7.3	Additional observations of Abell 1689	72
7.3.1	Strong and weak lensing analyses	72
7.3.2	Lensing mass profiles	73
7.3.3	Lensing results and discussion	74
7.3.4	Redshift distribution of cluster galaxies	75
7.4	Discussion	75
7.5	Conclusions	76
8	The perfect cluster Abell 1703	77
8.1	Abstract	77
8.2	Introduction	77
8.3	Cluster properties	79
8.3.1	X-ray	79
8.3.2	Gravitational lensing	80
8.3.3	Sunyaev-Zel'dovich effect	81
8.4	Feasibility	81
9	Concluding remarks	83
	Acknowledgements	87
	Coauthor statements	89

Bibliography

99

ABBREVIATIONS AND ACRONYMS

ACIS	Advanced CCD Imaging Spectrometer (onboard <i>Chandra</i>)
ACS	Advanced Camera for Surveys (onboard HST)
arf	Auxiliary Response File (for <i>Chandra</i> spectra)
BBN	Big Bang Nucleosynthesis
CCD	Charge Coupled Device
CDM	Cold Dark Matter
CERN	European Organization for Nuclear Research, Conseil Européene pour la Recherche Nucleaire
CIAO	Chandra Interactive Analysis of Observations
CFHT	Canada-France-Hawaii Telescope
CMB	Cosmic Microwave Background
CP	Charge conjugation and Parity
CXO	<i>Chandra</i> X-ray Observatory
Dec.	Declination
DM	Dark Matter
d. o. f.	Degrees Of Freedom
EI	Emission Integral
ESA	European Space Agency
.fits	Flexible Image Transport System (file format)
fov	Field Of View
FWHM	Full Width Half Maximum
HDM	Hot Dark Matter
HEASARC	High Energy Astrophysics Science Archive Research Centre
HEG	High Energy Grating (onboard <i>Chandra</i>)
HETG	High Energy Transmission Grating (onboard <i>Chandra</i>)
HRC	High Resolution Camera (onboard <i>Chandra</i>)
HRI	High Resolution Imager (onboard ROSAT)
HST	Hubble Space Telescope
KK	Kaluza-Klein
LEP	Large Electron Positron Collider (at CERN)
LETG	Low Energy Transmission Grating (onboard <i>Chandra</i>)
LHC	Large Hadron Collider (at CERN)
MEG	Medium Energy Grating (onboard <i>Chandra</i>)
<i>mekal</i>	MEWe-KAastra-Liedahl (emission model for hot plasma)
MSW	Mikheev-Smirnov-Wolfenstein (resonant neutrino production)
NASA	National Aeronautics and Space Administration
NE	North Eastern (part of Abell 1689)
NFW	Navarro-Frenk-White (density profile)

Obs id	Observation identification number (for <i>Chandra</i> data)
R. A.	Right Ascension
RASS	ROSAT All Sky Survey
rmf	Redistribution Matrix File (for <i>Chandra</i> spectra)
ROSAT	ROentgen SATellite
SDSS	Sloan Digital Sky Survey
S/H	Soft to Hard X-ray photon ratio
SUSY	SUper SYmmetric (extension of the Standard Model)
SW	South Western (part of Abell 1689)
SZ	Sunyaev-Zel'dovich
QCD	Quantum Chromo Dynamics
QED	Quantum Electro Dynamics
VLT	Very Large Telescope
<i>wabs</i>	Photoelectric absorption model with Wisconsin cross-sections
WDM	Warm Dark Matter
WFPC2	Wide Field Planetary Camera 2 (onboard HST)
WIMP	Weakly Interacting Massive Particle
Λ CDM	Λ (Lambda) Cold Dark Matter
ν MSM	Neutrino Minimal Standard Model

All given uncertainties are 1σ unless otherwise stated.

SUMMARY

This thesis presents my work on characterising dark matter from X-ray observations.

The current cosmological paradigm, the Λ Cold Dark Matter (Λ CDM) model, is very successful when it comes to explaining observations. Yet, the identities of two of its main components, namely dark matter and dark energy, remain a mystery. The dark matter accounts for 80% of the total mass in the Universe, but none of the particles in the otherwise successful Standard Model of particle physics have the right properties to explain the entire range of observational aspects of the dark matter. To solve this problem, a new theory is required at a fundamental level of elementary particle physics.

There are two main approaches to reveal the dark matter identity. The first one is to ask the particle physics theoreticians for a well motivated theory (from a particle physics point of view) including a candidate for the dark matter, and test it against observations. Hopefully, the theory can be either confirmed or rejected. However, in most cases all we can do is to reject a part of the allowed parameter space thus constraining the model.

The second approach is to observe the effects of the dark matter and derive model independent properties. The obtained properties can then be used as input for the particle physics models.

This thesis consist of two major parts each following one of the two described approaches to characterise dark matter using X-ray observations and some introductory material (Ch. 1, Ch. 2, Ch. 3, Ch. 6).

I have searched for X-ray emission signals predicted from decaying or annihilating dark matter for various particle candidates (Ch. 4). No line signal was found resulting in some general constraints on the allowed line emission from dark matter in the 0.3 – 10 keV range. For a specific candidate such as the sterile neutrinos, these constraints can be converted to a constraint in the mass-mixing angle parameter space. In order to improve the constraints, I have studied various types of astrophysical objects (the Milky Way halo, colliding galaxy clusters, spheroidal dwarf galaxies), different observational methods (imaging spectroscopy and gratings), and different analysis methods. Within this part of the thesis is also a small study on the allowed amount of continuous emission from dark matter (Ch. 5). This was converted to a constraint on the lifetime of a given type of axions, which could then be ruled out as a dark matter candidate.

In the second part, I have investigated the large scale distribution of dark matter by studying clusters of galaxies. Their mass profiles can be determined through several independent methods such as X-rays, weak and strong gravitational lensing, but these methods do not always agree. I did a case study of a deep X-ray observation of the galaxy cluster Abell 1689, for which earlier mass determination were in notable disagreement (Ch. 7). The deep X-ray observations allowed the identification and removal of substructure before reconstructing the mass profile. The resulting mass profile is in agreement with the lensing profiles within the error bars over the entire range of observed radii.

DANSK RESUMÉ

Denne afhandling præsenterer mit arbejde med at karakterisere mørkt stof fra astrofysiske røntgenobservationer.

Det nuværende kosmologiske paradigme, Λ CDM modellen (Lambda Cold Dark Matter), har stor succes når det kommer til at forklare observationer. Ikke desto mindre udgør naturen af to af hovedkomponenterne, nemlig mørkt stof og mørk energi, stadig en gåde. Det mørke stof udgør 80% af Universets samlede masse, men ingen af partiklerne i den ellers succesrige Standardmodel for partikelfysik har de rigtige egenskaber til at kunne forklare alle de observationelle beviser på det mørke stof. For at løse dette problem, er det nødvendigt med en ny teori på et fundamentalt partikelfysisk niveau.

Overordnet set er der to fremgangsmåder til at afsløre det mørke stofs natur. Den første er at bede de teoretiske partikelfysikere om en velmotiveret teori (fra et partikelfysisk synspunkt) med en mørkt stof kandidat, og teste den mod observationer. Forhåbentlig kan teorien enten bekræftes eller afvises. Desværre må vi som oftest nøjes med at udelukke en del af det ellers tilladte parameterrum for teorien.

Den anden fremgangsmåde er at observere effekterne af det mørke stof og derfra udlede model-uafhængige egenskaber. Disse egenskaber kan stilles som krav til partikelfysikteoriene.

Denne afhandling består af to hovedafsnit som hver følger en af de to beskrevne fremgangsmåder til at karakterisere det mørke stof ved brug af røntgenobservationer samt noget introducerende afsnit (Ch. 1, Ch. 2, Ch. 3, Ch. 6).

Jeg har undersøgt røntgenspektre for linjeemission fra henfaldende eller annihilierende mørkt stof som forudsagt for adskillige partikelkandidater (Ch. 4). Ingen emissionslinjer blev fundet, hvilket resulterede i en række meget generelle begrænsninger af den tilladte linjeemission fra mørkt stof i energiintervallet 0.3 – 10 keV. For specifikke kandidater såsom sterile neutrinoer kan disse begrænsninger omregnes til en begrænsning i masse-mixingvinkel parameterrummet. For at forbedre disse begrænsninger har jeg undersøgt forskellige typer af astrofysiske objekter (Mælkevejens halo, kolliderende galaksehobe, dværggalakser osv.), forskellige observationelle metoder (CCD- og gitterspektroskopi), samt forskellige statistiske analysemetoder. I denne del af afhandlingen indgår også et mindre studie af den tilladte kontinuerte emission fra mørkt stof (Ch. 5). Det resulterede i en begrænsning på levetiden af en speciel type axioner, som derved kunne udelukkes som mørkt stof kandidat.

I den anden del af afhandlingen har jeg undersøgt stor-skala fordelingen af mørkt stof ved at studere galaksehobe. Deres masseprofiler kan bestemmes ved hjælp af flere uafhængige metoder, såsom røntgenstråling og svage eller stærke gravitationelle linse effekter, men det er ikke altid at disse metoder stemmer overens. Jeg undersøgte galaksehoben Abell 1689, hvor tidligere massebestemmelser var i uoverensstemmelse med hinanden (Ch. 7). Meget dybe røntgenobservation tillod identifikation og fjernelse af substrukturer før rekonstrueringen af masseprofilen. Den resulterende masse profil er i overensstemmelse med masseprofilerne bestemt ved hjælp af gravitationelle linser (inden for usikkerhederne) for hele det observerede radius-interval.

1

BASIC COSMOLOGY AND DARK MATTER

Cosmology is the description of the Universe on a large scale. The current cosmological paradigm, the Lambda Cold Dark Matter model (Λ CDM) is favoured by a large number of observations. Nonetheless, the identity of two of its essential parameters, the dark matter and dark energy, remain unknown. This section contains a very brief introduction to the model and its relevant parameters with focus on the dark matter sector as well as an introduction to dark matter and its properties.

1.1 Λ CDM

Observations of the galaxy distribution (Fig. 1.1) show that on scales larger than the order of Mpc , the Universe is homogeneous and isotropic. Unless we live at an extremely special location, this tells us that the evolution of the Universe must be identical in all directions.

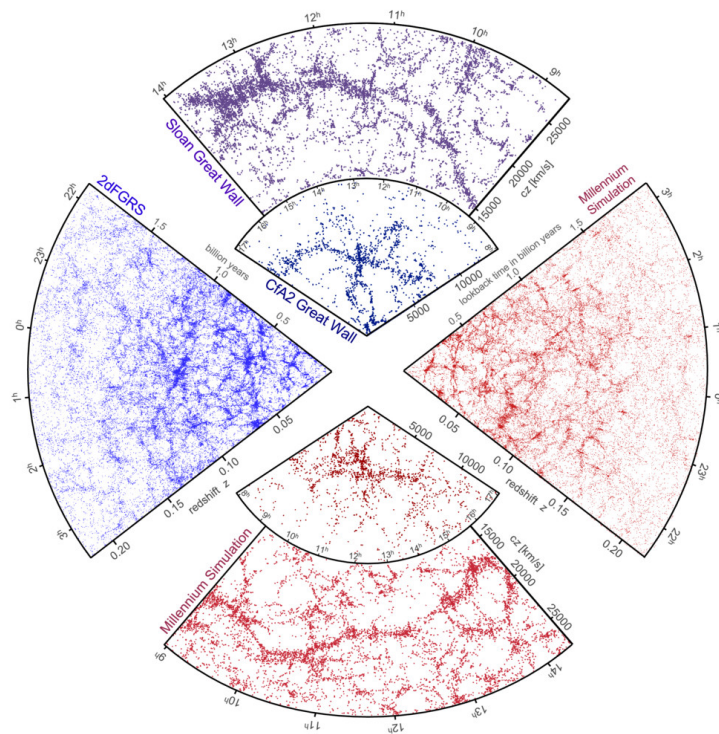


Figure 1.1: The large scale structure of the Universe as determined from galaxy surveys (blue) compared to the dark matter structures seen in numerical simulations (red, Springel et al., 2006).

Comparing observed astronomical spectra to laboratory spectra, there is a general redshifting of the astronomical spectra, from which we conclude, that everything is moving away from us, and hence that the Universe is expanding. The expansion rate is given by the Hubble parameter, which today is measured to be $H_0 = (71.9 \pm 0.027) \text{ km sec}^{-1} \text{ Mpc}^{-1}$ (Dunkley et al., 2009). Often H_0 is given in terms of $h = H_0/(100 \text{ km sec}^{-1} \text{ Mpc}^{-1})$. The value and evolution of the Hubble parameter is connected to the contents of the Universe, and described through the Friedmann equation (derived from the Robertson-Walker metric) and the fluid equation (derived from conservation of energy). Today the generally accepted cosmological model is the Λ CDM (see e. g. Ryden, 2003; Davis et al., 2007), in which the components dominating the evolution history are radiation, dark matter, and a cosmological constant.

In Λ CDM the expansion started approximately 13.7 Giga years ago from the Big Bang (Fig. 1.2). At that time, the Universe was a hot and very dense particle plasma. As it expanded and cooled, the interaction rate between the particles dropped, and the particles decoupled from the plasma to form the elements and structures we observe today.

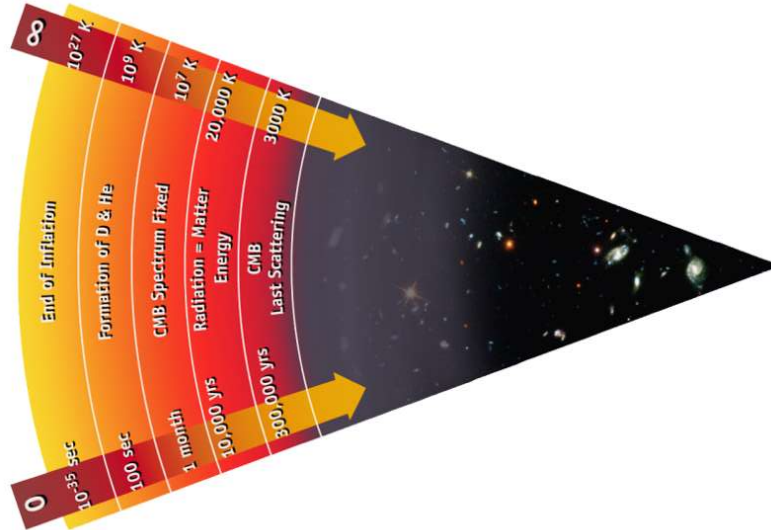


Figure 1.2: The expansion history of the Universe. The upper arrow indicates temperature and the lower time since Big Bang. The triangular shape illustrates an observation today.

The parameters of Λ CDM are mainly determined through fits to the Cosmic Microwave Background (CMB). The CMB was emitted approximately 300,000 years after Big Bang, when the Universe had cooled sufficiently for protons and neutrons to decouple from the plasma and form atomic nuclei. Short after, the recombination took place, in which the electrons coupled to the nuclei, forming neutral atoms. The binding of the electrons left the photons free to propagate without scattering off electrons and the Universe became transparent. Today we observe these photons from all directions as shown in Fig. 1.3. Remarkably the photons exhibit a nearly perfect blackbody spectrum with a peak temperature of 2.73 keV (Hinshaw et al., 2009). The small irregularities observed in the CMB are due to density fluctuations, which collapsed and developed into the structures we observe today. From the CMB temperature map, the angular power spectrum of the temperature fluctuations can be derived and compared to theoretical predictions, which depend on the values of parameters like the curvature, the matter density $\Omega_m h^2$, the baryon density $\Omega_b h^2$, the cosmological constant Λ , the scalar spectral index n_s , the optical depth due to reionisation, and the Hubble parameter H_0 .

For this thesis the important parameters are the present day values of the density parameters,

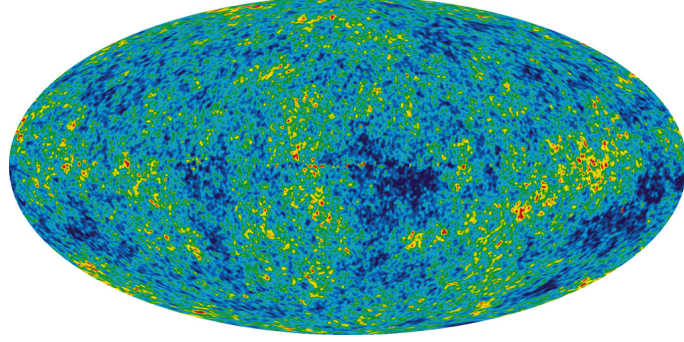


Figure 1.3: The CMB all-sky temperature map as observed with WMAP. The colour differences indicate temperature fluctuations from the average value of 2.73 keV after the map has been corrected for the Earth movement with respect to the CMB (NASA/WMAP Science Team, 2008).

$\Omega(t) = \rho(t)/\rho_c$, for the dominating components of the Universe namely the dark matter and dark energy. ρ_c is the critical energy density providing a flat Universe: $\rho_c = 3H^2(t)/(8\pi G)$, where G is the gravitational constant. For a flat Universe with several components, the density parameters sum to exactly one, which is within 1% of today's measurements (Dunkley et al., 2009): $\Omega_b h^2 = 0.02273 \pm 0.00062$ (baryons), $\Omega_{CDM} h^2 = 0.1099 \pm 0.0062$ (cold dark matter), $\Omega_\Lambda = 0.742 \pm 0.030$ (dark energy). In the Solar neighbourhood the dark matter density is $0.39 \pm 0.03 \text{ GeV cm}^{-3}$ (Catena & Ullio, 2009).

The first stars formed after some 100 Mega years and possibly also the first quasars. The ultraviolet radiation from those re-ionized the Universe, but at this point electron density was so low, that the Universe remained transparent. Super nova observations show that presently the expansion of the Universe is accelerating, which indicates that the dark energy is dominating (Riess et al., 1998).

Throughout my work I have assumed a Λ CDM model with the best fitting parameter values at the given time when the work was done. The variations are minor, and the used parameters are given as footnotes in the relevant chapters.

1.2 DARK MATTER

The energy density of visible matter in the Universe (stars, gas, dust, etc.) is not enough to outweigh the dark energy and make the Universe flat, as observed from the CMB (Dunkley et al., 2009). It turns out that about nine tenth of the total matter does not emit light and is only observed through its gravitational effects. Consequently it is called dark matter.

In the 1930's the astronomer, Fritz Zwicky, studied the velocity dispersion as a function of radius for the Coma Cluster of galaxies (Fig. 1.4). What he found was that the dispersion of radial velocities was very large - around 1000 km sec^{-1} . The mass of the visible stars and gas inside the cluster does not provide a gravitational potential large enough to confine the galaxies with such velocities in the cluster. He came to the conclusion that the cluster must contain a lot of "dunkle Materie" later translated to "dark matter". Today we know, that not only clusters, but also galaxies are dominated by dark matter and therefore their formation and evolution are driven by gravity.

The total observed matter density $\Omega_M h^2 \approx 0.1$ deviates significantly from the baryon density $\Omega_b h^2 \approx 0.02$ required for concordance between the observed light element abundances (H, D, ^3He , ^4He , ^7Li) and those predicted by Big Bang Nucleosynthesis (BBN, D'Amico et al., 2009). Consequently the dark matter cannot be baryonic, which excludes most of the Standard Model particles, and the neutrinos are too light to provide enough mass. The identity of the dark matter

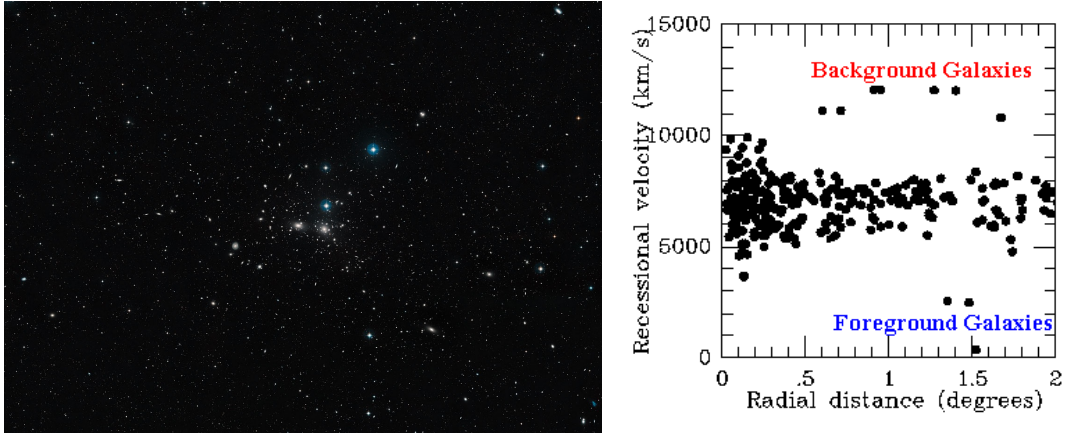


Figure 1.4: (Left) A wide field image of the region around the Coma Cluster also called Abell 1656. The field of view is approximately 2.7×2.85 degrees (Hubble Space Telescope, 2009). (Right) The velocity dispersions of the Coma Cluster galaxies is of the order of 1000 km sec^{-1} (Haynes, 2009).

remains a mystery though there are many proposed candidates, mostly in the form of exotic new types of particles. There could be more than one species of dark matter, but no clear evidence has been found to support this, and throughout this thesis I have assumed the simplest scenario with only one species.

1.2.1 REQUIRED PROPERTIES OF DARK MATTER

Even though the dark matter identity is unknown, there are some general properties a candidate must possess (see e. g. Taoso et al., 2008):

- By definition it must be dark in the sense that it does not take part in any Standard Model interaction with photons (or only very weakly).
- Its interaction with baryons must be very small or zero. Interactions with baryons would in most cases lead to indirect photon emission violating the darkness criteria. Also, it would affect the BBN and structure formation.
- The dark matter self-interaction must be very small or zero. The dark matter distribution in halos require a collision-less particle-like behaviour.
- Its properties must lead to the Universe we observe today e. g. the observed dark matter energy density, element abundance, structures such as galaxies and clusters, stellar formation history, etc.

One of the most striking observations favouring the existence of dark matter, is the Bullet Cluster shown in Fig. 1.5. Actually it consist of two galaxy clusters that collided some hundred million years ago. The galaxy cluster to the right passed through the galaxy cluster to the left. In the process, the intra-cluster gas, which is the dominating baryonic content, was displaced due to friction. However, the gravitational potential of the galaxies still follows that of the clusters. This is only possible if the clusters have a non-interacting heavy component (dark matter). The Bullet Cluster also gives an upper limit for the amount of self-interaction allowed for the dark matter of $\sigma m < 0.7 \text{ cm}^2 \text{ g}^{-1}$ where σ is the cross-section, and m the particle mass (Markevitch et al., 2004; Randall et al., 2008).

Λ CDM is based on a classical understanding of gravity. Instead of introducing dark matter, some of the observed effects can also be explained by modifications of the theory of gravity. How-

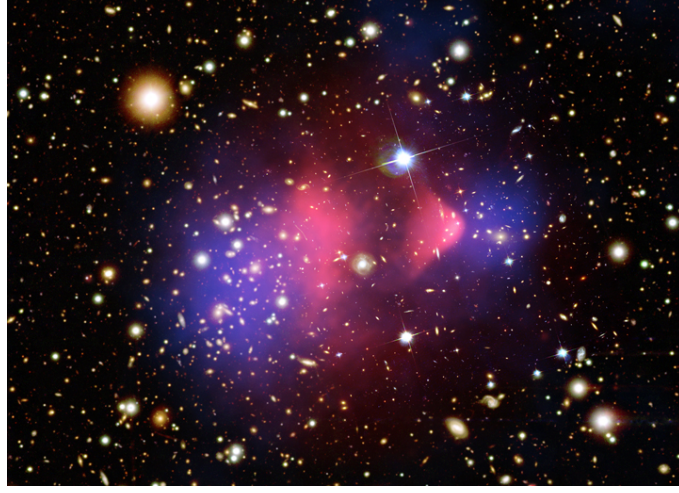


Figure 1.5: *The Bullet Cluster. Some hundred million years ago, the galaxy cluster to the right passed through the galaxy cluster to the left. The galaxies follows the gravitational potential (blue). The gas (red), which is the main baryonic content of the cluster, is clearly displaced from the gravitational potential because of friction during the collision (NASA, 2007).*

ever, currently none of the modified gravity models can simultaneously explain observations at all scales without the need for any dark matter (Dodelson & Liguori, 2006).

1.2.2 CANDIDATES

There are hundreds of dark matter candidates fulfilling the above criteria. Most of them can be (more or less) motivated from particle physics. The major families are Super Symmetric (SUSY) particles, axions, sterile neutrinos or Kaluza-Klein (KK) particles. I have mainly worked with sterile neutrinos and axions, which are introduced in detail in the relevant chapters (Ch. 3 and Ch. 5).

Particles with a mass in the GeV to TeV range, which for a given small cross-section provides the observed dark matter energy density, are commonly denoted as WIMPs (Weakly Interacting Massive Particle). Generally WIMPs are in thermal equilibrium in the early Universe and freeze out due to the expansion of the Universe. The resulting energy density is independent of the particle mass (D’Amico et al., 2009):

$$\Omega_{DM} \approx 0.1 \left(\frac{3 \times 10^{-26} \text{cm}^3 \text{sec}^{-1}}{\langle \sigma v \rangle} \right), \quad (1.1)$$

where $\langle \sigma v \rangle$ is the thermal average of the cross-section and relative velocities. For particles at the electro-weak scale such as those predicted by e. g. SUSY, this provides the observed dark matter density. In typical theories, the WIMPs can annihilate providing a testable albeit often experimentally challenging signature as discussed in the next sections.

1.2.3 DIRECT DETECTION

In Λ CDM the visible part of the Milky Way is embedded in a dark matter halo. If the halo consist of WIMPs, the observed dark matter energy density provides a local spatial density of $n_{DM} \approx 0.004(100 \text{ GeV}/M_{DM})\text{cm}^{-3}$ (D’Amico et al., 2009) corresponding to roughly one particle per liter. The relative velocity between the Earth and the dark matter halo is $v \approx 200 \text{ km sec}^{-1}$ and consequently we are continuously bombarded by WIMPs. One could hope to detect this

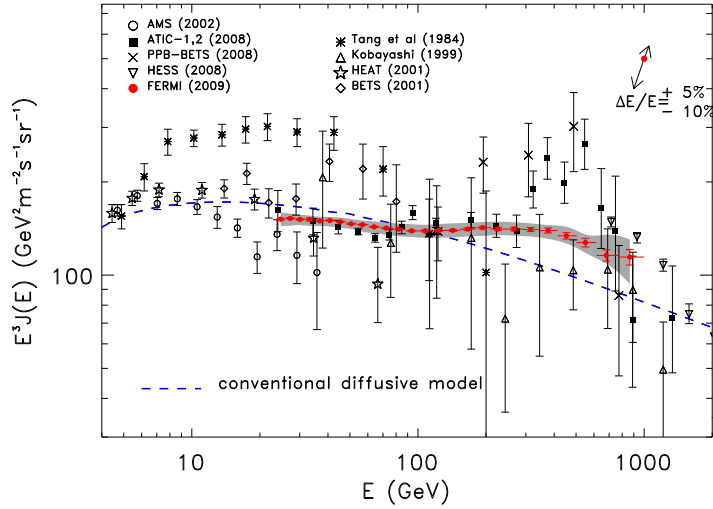


Figure 1.6: The cosmic ray electron plus positron spectrum observed with ATIC (black solid squares), H. E. S. S (triangles), Fermi LAT (red filled circles), and older experiments. The grey band is the systematic errors on the Fermi results. The two-headed error in the top-right corner indicates the possible rigid shift of the spectrum due to uncertainty in the energy calibration of Fermi. There is a similar uncertainty for the H. E. S. S results (Abdo et al., 2009).

WIMP wind experimentally by looking for a nucleus recoiling after an elastic scattering between the WIMP and the material in a low-background detector. This method is called direct detection and currently a range of experiments are running (CDMS, CRESST, DAMA, Xenon, etc.). So far only one experiment named DAMA has claimed a positive signal (Bernabei et al., 2008), which for most common dark matter models is in contradiction to the non-detection in the other experiments (Savage et al., 2009).

1.2.4 INDIRECT DETECTION

Another possible signature is particle or photon emission from decaying or annihilating dark matter. Depending on the specific model, the signature is either mono-energetic with an energy related to the dark matter particle mass, or a broad spectral feature at lower energies from cascade interactions. The signature can be detected either in primary or secondary photon or particle spectra.

For the primary particle spectra, the locally produced anti-particle fractions are not easily mimicked by astrophysical processes. Recently the positron to electron fraction observed with PAMELA (Adriani et al., 2009) and the total electron plus positron spectra from ATIC (Chang et al., 2008), H. E. S. S., (Aharonian et al., 2009), and Fermi (Abdo et al., 2009) shown in Fig. 1.6 have received quite some attention due to a possible excess compared to model predictions. However, caution must be advocated since neither the local astrophysical production of charged particles nor their propagation are well understood.

The charged particle propagation induces high energy photons by inverse Compton scattering and bremsstrahlung providing a broad bump feature in the γ -ray spectrum. A similar bump can originate from cascade decays following the annihilation. In both cases a cut-off is expected at the dark matter mass. The bump can be searched for with e. g. the recently launched Fermi Gamma-ray Space Telescope. Even though the γ -ray bump feature is easier mimicked by astrophysical sources than the corresponding particle spectra, the γ -rays propagate in straight lines

making it possible to distinguish different sources spatially. The combination of particle and photon signatures provides a consistency check for a possible dark matter signal.

The flux from annihilating dark matter, F , is generally given by (an additional factor of $1/2$ enters if the dark matter is not its own anti-particle):

$$\frac{dF}{dE} = B \frac{\langle\sigma v\rangle}{8\pi m^2} \frac{dN}{dE} \int_{los} \rho_{DM}^2(r(l,\theta)) dl, \quad (1.2)$$

where N is the number of particles or photons per energy produced per annihilation, ρ_{DM} is the density profile as a function of radius to be squared and integrated along the line of sight, l . The density profile is squared as each annihilation requires two particles. Eqn. 1.2 can be factorised into a part depending only on the particle physics properties of the dark matter, the integral depending only on the dark matter distribution, and a boost factor, B .

The annihilation cross-sections predicted by particle physics are usually so small that current observatories are far from sensitive enough to detect the signal. To account for this, a boost factor is often introduced, which can originate in modified particle physics or in dark matter substructures. Examples of the former are internal bremsstrahlung (Bringmann et al., 2008) or resonance effects such as the Sommerfeld enhancement (Lattanzi & Silk, 2009), which can increase the possible annihilation rate by several orders of magnitude. Since the flux is proportional to the density squared any substructure in the dark matter halo will boost the flux compared to a smooth halo as illustrated by Fig. 1.7.

For decaying dark matter, only one particle is required and the flux is directly proportional to the density profile:

$$\frac{dF}{dE} = \frac{d\Gamma_\gamma}{dE} \frac{\Omega_{fov}}{8\pi} \int_{los} \rho_{DM}(r(l,\theta)) dl, \quad (1.3)$$

where Γ_γ is the decay rate into photons and Ω_{fov} is the observed field of view.

The astrophysical part of Eqn. 1.2 and Eqn. 1.3 depends heavily on the assumed distribution of the dark matter, which is discussed in the next section.

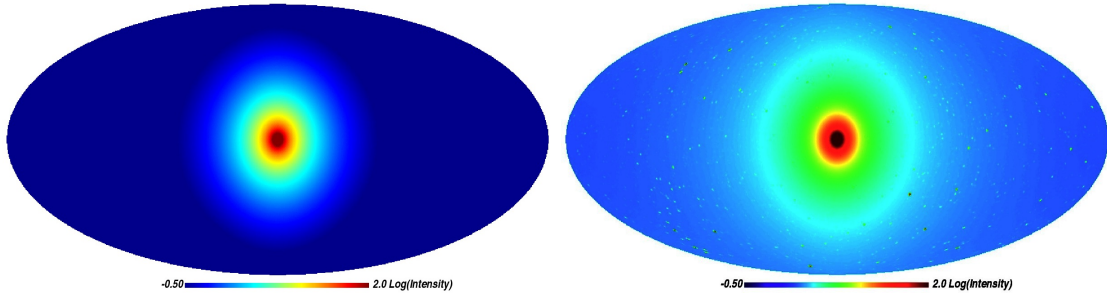


Figure 1.7: All-sky maps of the γ -ray emission from dark matter annihilation as predicted by the Aquarius simulation. (Left) The smooth main halo's diffuse emission. (Right) The expected total emission including the smooth main halo contribution as well as resolved and unresolved substructure (Springel et al., 2008).

1.2.5 THE NFW-PROFILE

The exact density distribution of the dark matter within the halos is still unknown. Especially in the central parts where simulations predict a cusp which is very challenging to observe and has not yet been firmly established observationally (Spekkens et al., 2005). One of the generally accepted profiles is the Navarro-Frenk-White (NFW) profile (Navarro et al., 1996). Assuming spherical symmetry the generalised density distribution is given by:

$$\rho_{DM}(x) = \frac{\rho_0}{x^\alpha (1 + x^\gamma)^{(\beta-\alpha)/\gamma}}, \quad (1.4)$$

where $x = r/r_s$. The scale radius, r_s , is a free parameter. For a standard NFW-profile $\alpha = 1.0$, $\beta = 3.0$, and $\gamma = 1.0$. Unless otherwise stated, those values have been adopted throughout this thesis.

The mass of a sphere is $M(< r) = \int_0^r \rho_{DM}(r') 4\pi r'^2 dr'$, which for the NFW-profile can be integrated to (e. g. Voigt & Fabian, 2006):

$$M_{tot}(< r) = 4\pi\rho_0 r_s^3 \left(\ln(1+x) - \frac{x}{1+x} \right). \quad (1.5)$$

Often the NFW-profile is expressed in terms of the concentration parameter c_f , relating a given overdensity with respect to the average density $f = \rho/\bar{\rho}$ (Navarro et al., 1996):

$$\rho_0 = \rho_c \frac{f}{3} c_f^3 \left(\ln(1+c_f) - \frac{c_f}{1+c_f} \right)^{-1}. \quad (1.6)$$

There are other popular profiles such as the Einasto (also known as Sersic profile, Merritt et al., 2006) and the Moore profile (Moore et al., 1999). As is seen from Fig. 1.8 the profiles mainly differ in the very centre and at large radii. For the applications in this thesis, the NFW-profile is sufficient, since the centre is never very well resolved by the observations, and they never extend to large radii.

Observations are 2D projections of the sky into a plane where density profiles are 3D. In order to compare theory and observations, the 3D density profile must be projected to a 2D surface density profile, $\Sigma(R)$, as a function of projected radius, R , from the 3D density, ρ_{DM} (Karttunen et al., 1996):

$$\Sigma(R) = \int_0^{R_{out}} \frac{\rho_{DM}(r)}{\sqrt{r^2 - R^2}} dr^2, \quad (1.7)$$

where the upper integration limit, R_{out} , is the chosen outer radius of the cluster. $\Sigma(R)$ can then be integrated over the field of view to determine the total observed mass.

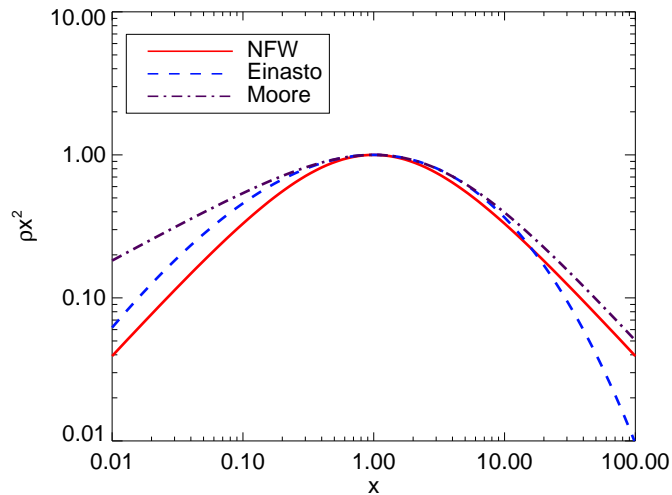


Figure 1.8: Examples of different dark matter profiles as a function of $x = r/r_{-2}$ where r_{-2} is the radius where the slope of the profile is -2 and ρ has been normalised to its value at the same radius (plot kindly provided by Ole Høst).

2

X-RAY OBSERVATIONS

This thesis is largely based on the analysis of X-ray observations of a range of objects. This chapter contains a general introduction to X-ray observatories, the data outcome and the analysis tools. If one is already familiar with these subjects, the chapter can be skipped.

2.1 X-RAY OBSERVATORIES

X-rays are absorbed by the Earth's atmosphere and therefore X-ray observations are carried out from space. For the time being there are two general purpose X-ray observatories operating onboard satellites: *XMM-Newton* (ESA) and *Chandra* (NASA, Fig. 2.1).

The concept behind the two observatories is the same. The incoming X-ray photons are collected and focused by grazing incidence telescopes (Fig. 2.2). The focal planes are equipped with CCD cameras allowing for measurements of the energy and the position of each incoming photon individually. This permits spatially resolved spectroscopy with medium resolution ($\Delta E_\gamma \approx 0.1$ keV) in the energy range $E_\gamma \approx 0.1 - 12$ keV (Arnaud, 2005). Higher resolution spectroscopy of point-like objects can be performed with gratings inserted between the mirrors and the CCDs.

Of the two observatories, *Chandra* has the best spatial resolution (0.5 arcsec versus 8 arcsec for *XMM*), but as it is only equipped with one telescope, where *XMM* has three telescopes operating

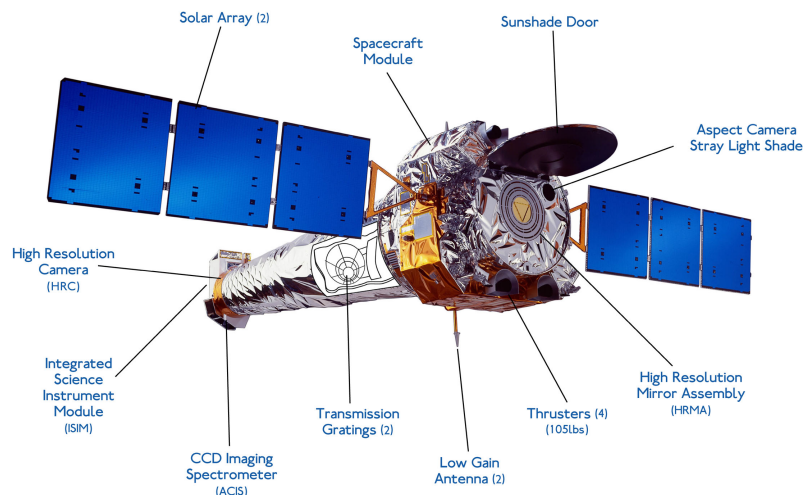


Figure 2.1: The Chandra X-ray telescope (NASA, 2007).

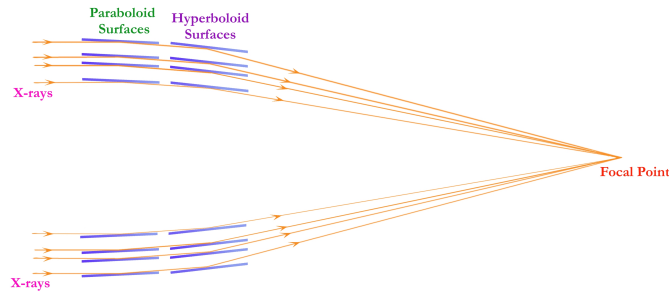


Figure 2.2: The principle of the grazing X-ray mirrors on board Chandra (NASA, 2007).

in parallel, its effective area is 3-5 times smaller than for *XMM*. The total on-orbit background level of *Chandra* is generally lower than that of *XMM* but depends on the specific observation (CXO Proposers' Observatory Guide, 2008; Ehle et al., 2007). I have only worked with *Chandra* data, so the following sections focus on *Chandra*.

2.2 CHANDRA DETAILS

The *Chandra* X-ray telescope is approximately 10 m long with solar panels attached to both sides (Fig. 2.1). It was launched by NASA in 1999 to an elliptical orbit of 16,000 km – 139,000 km, which is about a third of the distance to the moon. It has one single telescope with iridium-coated mirrors. In the focal plane it is possible to change between two detector arrays; the High Resolution Camera (HRC) with a very high spatial resolution and the Advanced CCD Imaging Spectrometer (ACIS) with a good spectral resolution. For bright point sources the spectral resolution can be improved by a factor of 50 by applying one of the two transmission gratings, LETG and HETG. *Chandra* provides calibrated data for the energy interval 0.1 – 10.0 keV (CXO Proposers' Observatory Guide, 2008). In this thesis only data from observations with the ACIS camera are treated because of their better spectral resolution.

The ACIS camera consists of two CCD arrays, ACIS-I with 4 chips and ACIS-S with 6 chips, arranged as shown in Fig. 2.3. The ten chips each covers a square field of approximately $(8.4 \text{ arcmin})^2$ but during observations only six of the ten chips can be active due to telemetry constraints. Two of the ten chips (ACIS-S1 and S3) have been treated specially and are back-illuminated thereby increasing and extending their sensitivity to lower energies than the rest of the chips which are front-illuminated.

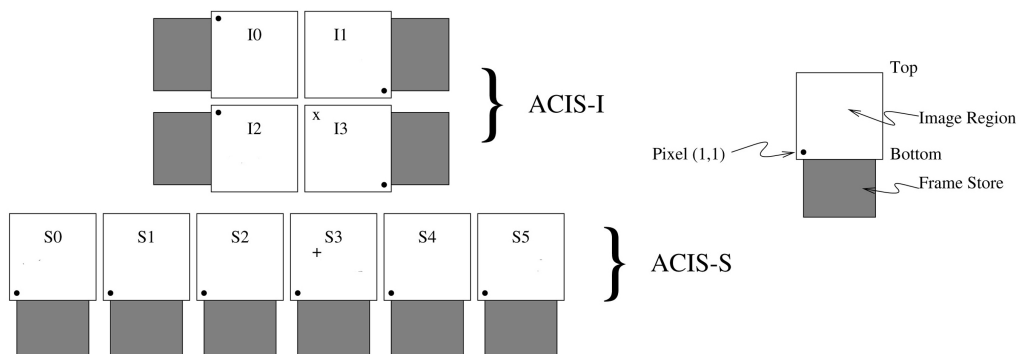


Figure 2.3: A schematic view of the Chandra ACIS focal plane layout. The "x" at the I3 chip and the "+" at the S3 chip represents the default aiming points for observations with ACIS-I and ACIS-S respectively (NASA, 2007).

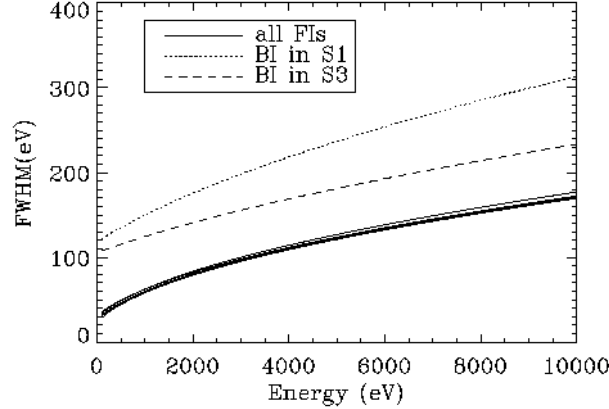


Figure 2.4: The resolution of the Chandra ACIS chips given as the FWHM as a function of photon energy (CXO Proposers' Observatory Guide, 2008).

The spectral resolution of the ACIS chips given in terms of the Full Width Half Maximum (FWHM) is shown in Fig. 2.4. For ACIS-S3 the resolution as a function of photon energy, E_γ , can be approximated by the straight line (CXO Proposers' Observatory Guide, 2008, Ch. 6):

$$\Delta E_{FWHM} = 0.012E_\gamma + 0.12 \text{ keV} . \quad (2.1)$$

2.2.1 TELEMETRY MODES

Chandra has a number of telemetry modes of which only two are relevant for this thesis: FAINT and VFaint (Very FAINT). They have different event grading schemes and thereby different background event selection options (CXO Proposers' Observatory Guide, 2008, ch. 6.14). In the FAINT mode recorded events are graded from the pixel values in a 3x3 pixel island. In the VFaint mode the events are also graded from a 3x3 pixel island, but the pixel values in 5x5 islands are saved allowing for a more precise grading during ground processing. The advantage of the VFaint mode is a reduced number of background events (for lowest and highest energies) with the loss of only a few percent of good events (CXO Proposers' Observatory Guide, 2008, ch. 6.14). Data observed in the VFaint mode should always be reprocessed manually before analysis instead of using the pipeline in order to lower the background level.

2.2.2 GRATINGS

The X-rays arriving from a point source can be deflected in a grating allowing for a very high spectral resolution. The High Energy Transmission Grating (HETG) onboard *Chandra*, intercepts the X-rays reflected from the mirrors, changing their incoming angle by amounts that depend sensitively on the photon energy. One of the focal plane detectors (HRC or ACIS-S) records the location of the diffracted X-rays, enabling a precise determination of their energies with an accuracy better than $E_\gamma/\Delta E_{FWHM} \approx 1000$ at 1 keV (CXO Proposers' Observatory Guide, 2008, Ch. 8).

The HETG consists of 336 gold grating facets mounted on a multiple ring formed assembly that can be swung into position between the *Chandra* mirrors and the CCDs. The inner two rings are the High Energy Grating (HEG) facets, and the outer two rings are the Medium Energy Grating (MEG) facets. The facets are made of thin gold bars mounted closely on plastic membranes. The gold bars are partially transparent to X-rays, so the diffraction is quite efficient, and more X-rays are captured by the CCDs.

Grating part	Thickness [Å]	Spacing [Å]	Resolution, FWHM [Å]	Default Bin Size [Å]
HEG	1200	2000	0.012	0.0025
MEG	2000	4000	0.023	0.005

Table 2.1: Grating details and resolutions for HEG and MEG (CXO Proposers' Observatory Guide, 2008; Chandra X-ray Centre, 2009c).

The HETG gratings are designed to cover an energy range from 0.4 keV to 10 keV with HEG covering the interval $E_\gamma = 0.8 - 10.0$ keV and MEG covering $E_\gamma = 0.4 - 5.0$ keV. The very high spectral resolution is used in the study of detailed energy spectra, distinguishing individual X-ray lines from specific atomic transitions. The exact resolutions of the HEG and MEG spectrometers are given in Tab. 2.1.

The default pipeline bin size of HEG and MEG is oversampled by a factor of 4–5 so the binning is finer than the actual instrumental resolution. To account for this and to improve statistics, the data can be rebinned by a factor of " x " where the value $x = 4.8$ corresponds to the instrumental resolution. This gives an energy resolution of:

$$\Delta E_{FWHM}^{HEG} = \frac{x(E_\gamma/\text{keV})^2}{4972} \text{ keV} \quad \text{and} \quad \Delta E_{FWHM}^{MEG} = \frac{x(E_\gamma/\text{keV})^2}{2486} \text{ keV}. \quad (2.2)$$

2.3 ANALYSIS OF X-RAY DATA

Most *Chandra* data are proprietary the first year, where after they become public available through NASA's High Energy Astrophysics Science Archive Research Centre, HEASARC (NASA, 2008). The database can be queried for coordinates or object names and available data can then be downloaded as .fits files. Each observation is identified by a four digit observation id.

2.3.1 TOOLS

The data files are processed with the Chandra Interactive Analysis of Observations, called CIAO¹. It is a mission independent command-line based data analysis system designed to handle N-dimensional data files (Fruscione et al., 2006). For each of my projects I have at the given time used the newest version of CIAO and calibration database. The version numbers are given in the relevant sections. CIAO is very well documented with guides for all standard analysis purposes available (*Chandra* X-ray Centre, 2009a).

The modelling and fitting tool "Sherpa" is central to the CIAO system. Sherpa performs forward fitting of models to data in N dimensions. Sherpa includes the "S-Lang" language which can be used for scripting and data manipulation (Freeman et al., 2001; Davis, J. E., 2008). Another spectral fitting package included in CIAO is the tcl-based Xspec used for spectral analysis and fitting (Arnaud et al., 2009; tcl.tk, 2009).

For visualisation I have found the ds9 application (Smithsonian Astrophysical Observatory, 2009) and *fv* quite useful (Irby, B., 2008a).

2.3.2 THE RAW DATA AND REPROCESSING

The obtained data consist of the "raw" data files called secondary files, and the default pipeline processed data files called primary files, which are "level2" files to be used straight away for data analysis. If the newest calibration has not been applied by the pipeline, the data files should be reprocessed to level2 files manually (*Chandra* X-ray Centre, 2009e). The reprocessing includes a

¹CIAO derives from "s'ciavo" meaning "I am your servant" in Venetian

check for the presence of cosmic-ray background events, corrections for spatial gain variations due to charge transfer inefficiency and a re-computation of event grades.

2.3.3 BAD PIXELS, GOOD TIME INTERVALS AND POINT SOURCE REMOVAL

Before the actual data analysis can take place it is necessary to take care of bad pixels in the CCDs, flares from X-ray variable sources or cosmic rays disturbing the observation, and point source removal. The first step of the preparation is to locate the bad-pixel file among the primary files, and set up the system to use this file containing observation specific information about the CCD pixels.

When dealing with extended sources, point sources should be removed during the data preparation. CIAO features three algorithms for point source identification: Wavelets, Voronoi tessellation, and sliding-cell search. I have used the wavelet algorithm (*wav_detect*) since it is the most effective all-round point source identifier (*Chandra X-ray Centre, 2009d*). The point sources are assumed to have a Gaussian shape and are then identified on statistical basis. An example of the point sources identified by *wav_detect*, is shown in Fig. 2.5. If any point sources are removed, it is important to remove the same regions in the blank sky background data, if applied.

Thanks to the orbit of *Chandra* the periods of flaring particle background are rare compared to *XMM*, but they still have to be identified and excluded. This is done separately for each chip with a tool called *lc_sigma_clipping* by plotting the light curve (number of received photons as a function of time) and cut away those time intervals where the number of photons deviates more than 3σ from the mean as shown in Fig. 2.6 (*Chandra X-ray Centre, 2009b*).

Now the data are ready for image or spectral analysis.

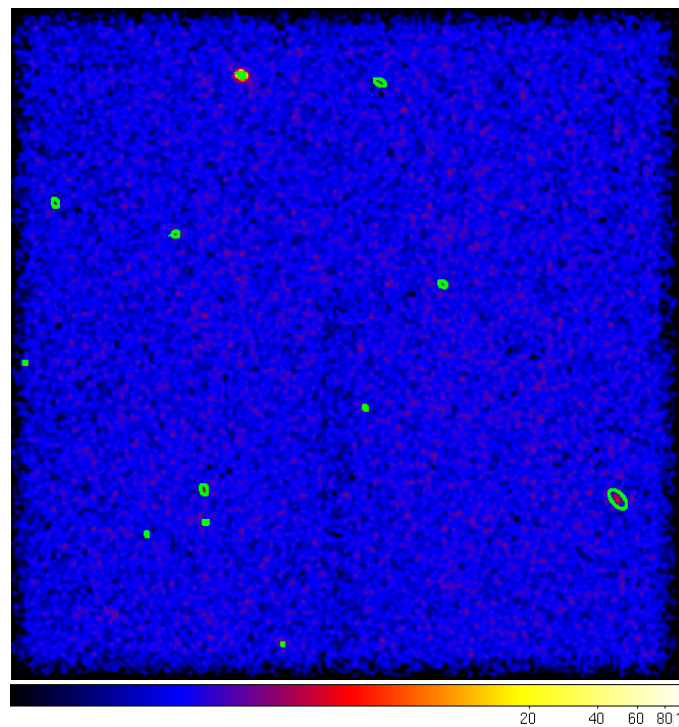


Figure 2.5: An example of the point source detected with *wav_detect* (green circles) for observation 9586 of the Draco dwarf galaxy.

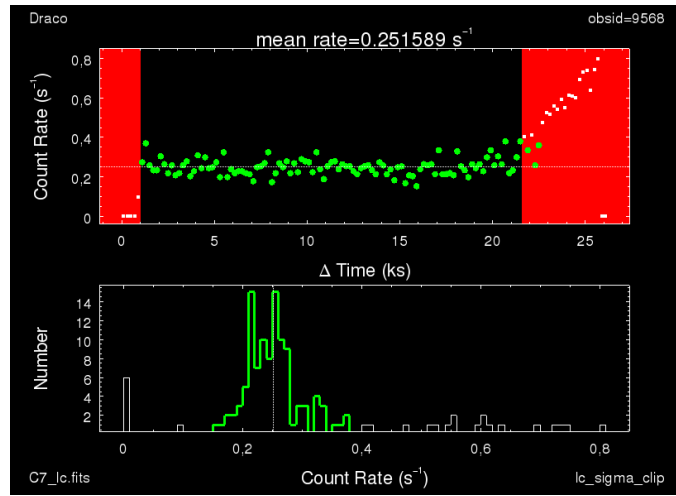


Figure 2.6: An example of light curve cleaning with *lc_sigma_clipping* for observation 9586 of the Draco dwarf galaxy. In the top plot, green points are those that passed the sigma-clipping and the horizontal dotted line shows the mean value of these points. The bottom plot is a histogram of the count rate values; the green curve again shows the data that passes the sigma-clipping algorithm.

2.3.4 INSTRUMENTAL RESPONSE

Due to imperfect detection methods, the energy and spatial distributions of the photons collected by the CCDs are not identical to the corresponding distributions of the incoming photons. The main effects are vignetting and the probability of an incoming photon to be detected by a given pixel in the CCD (sensitivity), under one called detector response.

Vignetting is the variation in the effective photon collecting area of the telescopes as a function of photon energy and position relative to the optical axis of the telescope. The spatial part can be understood in terms of classical optics (in the case of no diffraction) by looking at Fig. 2.7: An incident wave will only be totally reflected from the mirror if the incident angle is less than the critical angle. If the incident angle is larger than the critical angle, the reflectivity decreases monotonically as a function of increasing angle and hence the effective photon collecting area decreases as a function of off-axis distance. For X-rays one way to increase the effective area is to arrange several nearly cylindrical mirrors inside each other in a co-axial configuration as seen in Fig. 2.2. Vignetting is also energy dependent since the reflectivity of the high-density materials used for mirror coating in general decrease with energy at X-ray frequencies.

In theory, the detector response can be split into a spatial part which is relevant for image

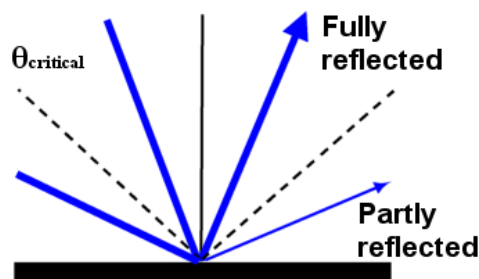


Figure 2.7: An incident wave will only be totally reflected from the mirror if the incident angle is less than a critical angle. If the incident angle is larger the reflectivity decreases monotonically as a function of increasing angle.

analysis and an energy dependent part which is relevant for spectral analysis. Unfortunately the real world is more complicated and the two are entangled.

For imaging analysis the response is accounted for by using an exposure map, i. e. an image containing the effective exposure time at a given energy and detector position. However, in order to create an exposure map, one needs to know the source spectrum. Often this is avoided by assuming the exposure map at the median energy of the spectrum to be representative for the full spectrum.

For spectral analysis there are two response files containing observation specific information: A "redistribution matrix file" (rmf) which maps from instrument energy channel to incident photon energy i. e. converts between channel space and energy space involving the spreading of photons due to instrumental resolution; and an "auxiliary response file" (arf) which accounts for the net effective area as shown in Fig. 2.8 as well as quantum efficiency. The combination of the two files can be thought of as the transformation of a flat spectrum through the detector (for a given area of the detector).

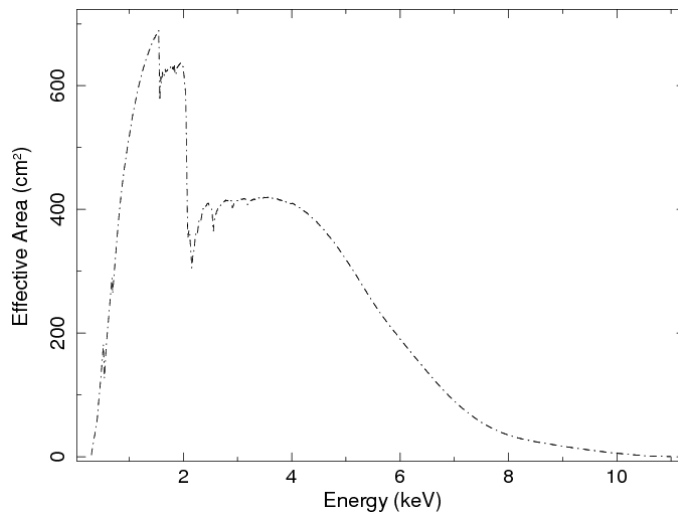


Figure 2.8: The effective area of ACIS S3 for observation 9586 of the Draco dwarf galaxy.

2.3.5 EXTRACTING SPECTRA AND INSTRUMENTAL RESPONSE FILES

First the region of which one is interested in the spectrum must be defined in the detector plane (e. g. using ds9). The CIAO tool for extracting spectra is called *specextract*. Apart from the spectrum of the given region, the arf and rmf files described in Sec. 2.3.4 are generated. For background subtraction also the background region must be defined. If nothing is subtracted as background, the spectrum includes various contributions apart from the source such as cosmic X-ray background, unresolved sources within the field of view, emission from the Milky Way halo, and instrumental effects as illustrated in Fig. 2.9.

2.3.6 BACKGROUND SUBTRACTION

Background subtraction is a rather non-trivial task because the background consist of several components with a different dependence on energy and position, both of the detector and the sky. There are three possibilities for subtracting the background: using another part of the same observation, using blank sky data, or using a model for the background (*Chandra* X-ray Centre, 2009f).

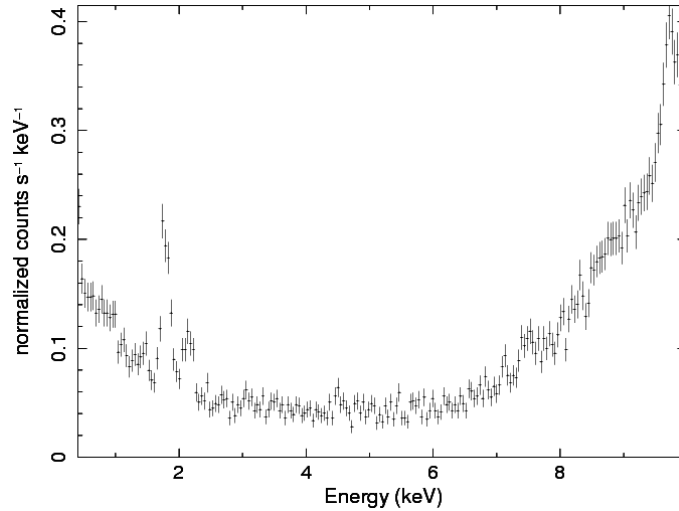


Figure 2.9: An example of a spectrum before background subtraction from the Draco dwarf galaxy observation 9586 .

If the spectrum is extracted from a region that does not cover all of the field of view, another part of the same observation can be used as background. The advantage is that the background will be from the same part of the sky at the right time i. e. eliminating any time variation of the background. The disadvantage is that the instrumental background does also depend on the position on the detector, and the same region cannot be used both as background and source. To avoid this problem it is possible to use blank sky data which is a stack of observations of X-ray sourceless regions in the sky. In this way the background can be taken from the right position on the detector, but there is no guarantee that the background of the blank sky data is similar to the background in the direction of the observed source at the given time (*Chandra* X-ray Centre, 2009f). Quite often the blank sky spectrum must be normalised to the source spectrum in order to reflect the background at the given sky position. The normalisation interval must be without significant source emission. For clusters of galaxies it is customary to use the 10 – 12 keV interval in the outer part of the observation (Markevitch, 2002).

Modelling the background is very challenging, so usually one of the above described methods for background subtraction is preferable.

2.3.7 SPECTRAL MODEL COMPARISON

For X-ray observations, the instrumental response contained in the *arf* and *rmf* files is not an analytical model. Consequently it is not possible to remove the instrumental effect in a robust and unique way in order compare an unfolded spectrum with a model spectrum. Instead a given model is convolved with the instrumental effects before it is fitted to the spectrum in units of "normalised counts per instrument energy channel". The free model parameters are determined using χ^2 or cash-statistics (Cash, 1979). Depending on the fitted model, physical parameters of the source can be derived and the flux determined from the model. Xspec contains a lot of pre-defined models, which can also be accessed from Sherpa.

3

STERILE NEUTRINOS

The sterile neutrino is an excellent dark matter candidate which only requires a minimal extension of the Standard Model. The model referred to as ν MSM (neutrino Minimal Standard Model) can, with the right choice of parameters, explain the observed flavour mixing and mass splitting of the active neutrinos, the baryon asymmetry of the Universe and provide a well motivated dark matter candidate. This chapter gives an overview of the motivation for the model and the theory needed to understand the various types of observational constraints.

3.1 COLD, HOT, AND WARM DARK MATTER

The Universe was matter-dominated at the time when structures formed and hence the dark matter must have left its signature in the structures we observe today. One of the original motivations for the sterile neutrino as a dark matter candidate was the discrepancies between the observed structures and the ones predicted by numerical simulations (Dodelson & Widrow, 1994). The argument is briefly outlined in the following.

Dark matter is often split into cold, warm or hot depending on the typical length scale of the smallest formed structures (which for thermal relic dark matter is related to the temperature at the time of freeze-out). Often the structure distribution is quantised in terms of the matter power spectrum, $P(k)$, which is defined as the average of the relative density fluctuation squared for a given Fourier mode, k :

$$P(k) = \left\langle \left| \frac{\delta\rho}{\bar{\rho}} \right|_k^2 \right\rangle. \quad (3.1)$$

The classical Λ CDM cosmology contains a single species of cold dark matter particles (CDM) which clusters at small scales (stars and galaxies) and later form larger structures (galaxies and clusters) through merging. In the pure CDM scenario, there is no significant cut-off in the predicted matter power spectrum today (even though most candidates e. g. from SUSY predicts a cut-off, Hofmann et al., 2001; Boehm et al., 2002; Diemand et al., 2008). In the 1990's this led to "the missing satellite problem" because the number of satellites predicted by numerical CDM simulations did not correspond to the number of observed dwarf galaxies in the vicinity of the Milky Way (e. g. Moore et al., 1999). Also the density profiles of dark matter halos provided a challenge: The CDM simulations predicted monotonically increasing density towards the centre of the halos thereby leading to a cuspy density profile, which seemed to be in contradiction with observations (Navarro et al., 1996).

These problems can be solved by a warmer dark matter candidate, which wipes out structures up to a certain scale, so at the time when the particles become non-relativistic, there are no structures left at small scales providing a non-negligible cut-off in the matter power spectrum (see Fig. 3.1). In the ultimate hot dark matter (HDM) scenario there will be very little structure on

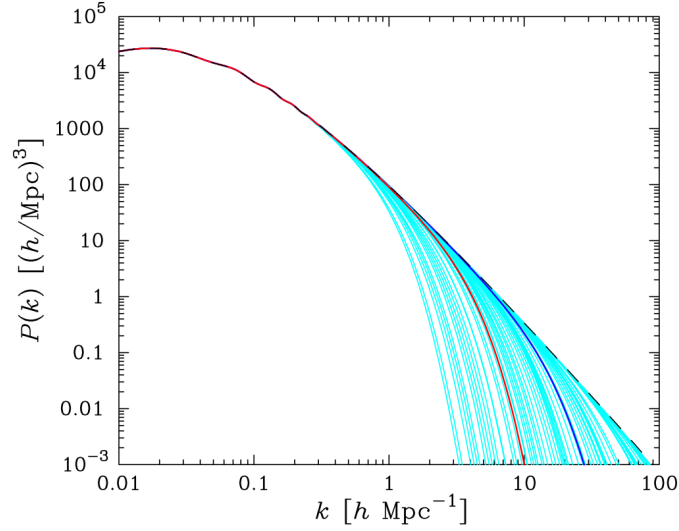


Figure 3.1: Illustration of the linear matter power spectrum and the cut-offs introduced by warm dark matter in the form of non-thermal sterile neutrinos in the mass range $m_s = 0.3 - 140$ keV (Abazajian, 2006).

galactic scales, which does not correspond with the observations as seen in the e. g. the Hubble Space Telescope (HST) image in Fig. 3.2. So far, a cut-off in the matter power spectrum has not been established observationally.

Between the bottom-up scenario of CDM and the HDM top-down scenario lies the intermediate region of a warm dark matter particle (WDM) with a typical rest mass in the keV-range, which allows for both small and large scale structures. (Bode et al., 2001). The keV-mass sterile neutrino proposed by Dodelson & Widrow (1994) was a warm dark matter candidate able to solve the apparent discrepancies between the CDM simulations and reality.

Today the missing satellite problem has been solved otherwise. Partly due to the detection of many more Milky Way dwarf satellites (Gilmore et al., 2007; Donato et al., 2009) and partly from more detailed numerical simulations predicting very little star formation in the dwarfs hiding them from observation and making them subject to selection effects (Koposov et al., 2009). Also the predicted cusps have been shown to be very challenging to detect and in agreement with current observations (Spekkens et al., 2005).

Even though the problems with CDM may have gone away, the keV-mass sterile neutrino is still an attractive dark matter candidate, because through different production mechanism scenarios they can be produced with very different free streaming length properties (see Sec. 3.4, Boyarsky et al., 2009d; Kusenko, 2009). The ν MSM is a rather simple model in comparison to

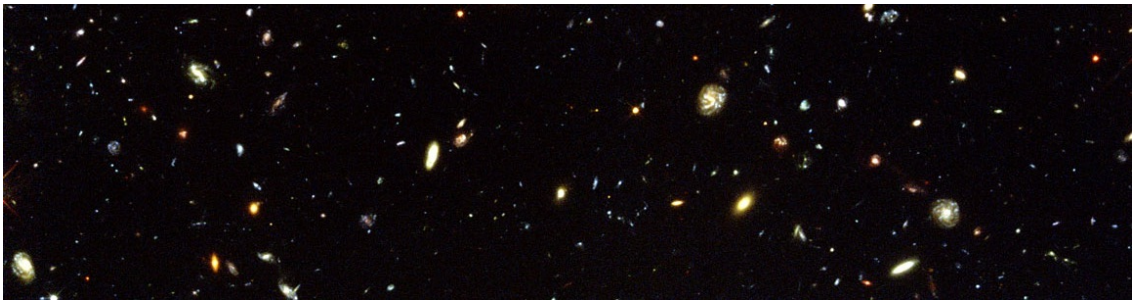


Figure 3.2: The Hubble Deep Field images show a lot of structures in the Universe (Hubble Space Telescope, 2009).

other theories such as SUSY or KK particles, and it is viable independent of the findings of the Large Hadron Collider (LHC) being constructed at CERN. Apart from providing a dark matter candidate, the model supply an explanation for the active neutrino masses as required by the observed neutrino oscillations, the baryon asymmetry of the Universe (Asaka & Shaposhnikov, 2005), as well as alternative uses e. g. an explanation for the peculiar velocities of pulsars by allowing for asymmetric neutrino emission (Kusenko & Segrè, 1997; Fuller et al., 2003), and synthesising early star formation (Biermann & Kusenko, 2006).

3.2 THEORY OF STERILE NEUTRINOS

The sterile neutrinos can be highly motivated by particle physics. This section gives a very compact introduction to the Standard Model of particle physics with the focus on the neutrino sector and the sterile neutrino extension. An extensive description can be found in The Particle Data Group's Review by Amsler et al. (2008).

3.2.1 THE STANDARD MODEL OF PARTICLE PHYSICS

Developed primarily in the 1960's the Standard Model is a group-theoretical extension of quantum mechanics derived from fundamental symmetries found in nature. Basically the Standard Model describes the elementary particles and the forces between these particles. It is defined as a renormalisable field theory based on the $SU(3) \times SU(2) \times U(1)$ gauge group. It contains three families with left-handed particles being the $SU(2)$ doublets, right handed particles being the $SU(2)$ singlets and one Higgs doublet. The resulting elementary particles (summarised in Tab. 3.1) are split into two sectors: quarks and leptons. Both sectors are again split into three generations as found experimentally at the now closed Large Electron Positron (LEP) Collider at CERN (Amsler et al., 2008). For the leptons, the three generations are composed of an electron-like particle and its corresponding neutrino: (e, ν_e) , (μ, ν_μ) , and (τ, ν_τ) .

The Standard Model particles interacts through the four fundamental forces via their proper force carriers: The photon for the electromagnetic interaction, the Z^0 and W^\pm bosons for the weak interaction, the eight gluons for the strong interaction and perhaps a graviton for the gravity. The electromagnetic and the weak interactions have been unified into the so called Quantum Electro Dynamics (QED) and the strong interaction is described in a theory called Quantum Chromo Dynamics (QCD). So far, gravity has not yet been mathematically incorporated into the Standard Model. All the particles in the Standard Model have antiparticles associated with them, except for the photon, which is its own anti-particle. These antiparticles have the same mass and spin as their counterparts, but all other quantum numbers are reversed.

Matter, in the form that we know it, consists of protons and neutrons which again are made of a combination of three up and down quarks together with a number of gluons. All particles composed of three quarks are called baryons and the fact that we observe more matter than anti-

Quarks (spin 1/2)			Leptons (spin 1/2)			Force carriers (spin 1)		
Particle	Mass	Charge	Particle	Mass	Charge	Particle	Mass	Charge
up (u)	≈ 2.4 MeV	2/3	electron (e)	0.5 MeV	-1	photon (γ)	0	0
down (d)	≈ 4.3 MeV	-1/3	e-neutrino (ν_e)	< 2 eV	0	Z-boson (Z^0)	91 GeV	0
charm (c)	0.1 GeV	2/3	muon (μ)	0.1 GeV	-1	W-boson (W^-)	80 GeV	-1
strange (s)	0.1 GeV	-1/3	μ -neutrino (ν_μ)	< 2 eV	0	W-boson (W^+)	80 GeV	+1
top(t)	171 GeV	2/3	tau (τ)	1.8 GeV	-1	gluon (g)	0	0
bottom (b)	4.2 GeV	-1/3	τ -neutrino (ν_τ)	< 2 eV	0	graviton?	?	?

Table 3.1: The particles of the standard model. The force carrying particle for gravity, the graviton, has not yet been detected experimentally (Amsler et al., 2008).

matter in the Universe is called baryon asymmetry.

On top of all this comes the Higgs boson which provide the link between the quantum field description of the particles and their masses (Halzen & Martin, 1984). Its existence has not yet been experimentally verified, but one of the purposes of the upcoming LHC is to look for the Higgs boson.

In the Standard Model the neutrinos are exactly massless. However, neutrino experiments provide compelling evidence for flavour neutrino oscillations (explained in Sec. 3.2.2), which requires the neutrinos to have non-zero masses (Amsler et al., 2008). This is an indication for new physics beyond the Standard Model.

Another problem with the Standard Model is that it does not provide any good candidates for the dark matter and the cosmological constant (dark energy). The cosmological constant has been proposed to be a kind of vacuum energy, but so far it has not been possible to come up with a theory that reproduce the correct order of magnitude from a Standard Model vacuum energy.

3.2.2 STANDARD MODEL NEUTRINO PHYSICS

From analyses of the decay width of the Z-boson at LEP, we know there exist $N_\nu = 2.994 \pm 0.012$ neutrino species that are sensitive only to weak interactions (Amsler et al., 2008). They are called flavour eigenstates or active neutrinos, ν_e, ν_μ, ν_τ , and are linear combinations of states with definitive mass, ν_i . In the Standard Model the number of mass eigenstates is taken to be equal to the number of flavour eigenstates i. e. $i = 1, 2, 3$. The difference between flavour and mass eigenstates is a non-Standard Model phenomenon called neutrino mixing.

In a three-neutrino scenario, flavour and mass eigenstates are related by a 3×3 mixing matrix called U , which can be parametrised by three mixing angles and a phase describing the experimentally verified non-conservation of charge and parity in weak interactions (CP violation). In total there are seven mixing parameters (including the three neutrino masses) to be determined experimentally. One way is through the neutrino oscillation experiments, where the (dis)appearance of a given type of neutrinos in a pure one-type neutrino beam is measured. Unfortunately the oscillation experiments are not sensitive to the absolute mass scale but only to the differences of the squared neutrino masses $\Delta m_{21}^2 = m_2^2 - m_1^2$ (solar neutrinos), $|\Delta m_{31}^2| = m_3^2 - m_1^2$ (atmospheric neutrinos). The phenomenon of flavour mixing is also seen in the quark sector, but with much smaller mixing angles (Cabibbo, 1963; Kobayashi & Maskawa, 1973; Amsler et al., 2008).

Currently, the strongest firm upper limit on the sum of the neutrino masses comes from the WMAP 5-year observations of the CMB leading to an upper limit on the sum of the neutrino masses of $\Sigma m_\nu < 0.67 \text{ eV}$ assuming Λ CDM cosmology (Komatsu et al., 2009). The same analysis also finds that three active neutrino species are favoured by cosmology, confirming the results from LEP.

3.2.3 STERILE NEUTRINOS

Of all the particles in the Standard Model, the neutrinos are the least understood and the least theoretically incorporated. In the Standard Model, the leptons are Dirac particles and have, except for the neutrinos, two polarisation states: left-handed and right-handed (i. e. they transform as doublets under the $SU(2)_L \times U(1)_Y$ gauge group). For the neutrinos only the left-handed neutrinos and right-handed anti-neutrinos have been observed experimentally (parity violation) and therefore incorporated in the model (Amsler et al., 2008)

If the neutrinos are pure Dirac particles, also right-handed neutrinos (and their left-handed anti-neutrinos) should exist. They are often referred to as sterile neutrinos, since they do not par-

ticipate in any Standard Model electro-weak interactions (i. e. they are singlets of the $SU(2)_L \times U(1)_\gamma$ gauge group, Maggiore, 2003).

The neutrinos can also be Majorana particles, which by definition are their own anti-particles. If the neutrinos are pure Majorana particles they can be described as entirely left-handed, but then the lepton number conservation in electro-weak interactions involving neutrinos is violated. It is very difficult to distinguish experimentally between the two types of particles. Currently the best limits on the Majorana mass term of the active neutrinos is $m_{\nu M} \lesssim 19.5 \text{ eV}$ (90% confidence level) provided by the neutrino-less double β -decay experiment called NEMO-3 (Argyriades et al., 2009)

To make it even more complicated there is also the possibility that the neutrinos are a mixture between Dirac and Majorana particles achieving characteristics and mass terms from both types.

3.2.4 ν MSM AND NEUTRINO MASSES

In the Standard Model, the active neutrinos are exactly massless, which is in contradiction to their experimentally observed non-zero mass splittings. A simple way to generate those masses is via the seesaw mechanism where a number of electro-weak singlets are added to the Standard Model by hand in terms of right-handed sterile neutrinos which are a mixture of Dirac and Majorana particles (Amsler et al., 2008). As long as the added neutrinos are singlets under $SU(3) \times SU(2)_L \times U(1)_\gamma$, which means they do not participate in any Standard Model interaction, any number can be added. Two heavy eigenstates are needed to explain the solar and atmospheric mass differences of the active neutrinos. The resulting mixing angles are however too large to fulfil the criteria for a dark matter candidate, and in this case a third sterile neutrino is needed. There are already three families of leptons, so there is a certain kind of symmetry in having three sterile neutrinos as well. The successful "three sterile neutrino extension" of the Standard Model is called the ν MSM and is a renormalisable theory in agreement with particle physics experiments (Asaka & Shaposhnikov, 2005). It is described in a number of papers (e. g. Asaka & Shaposhnikov, 2005; Asaka et al., 2005, 2006a,b, 2007; Shaposhnikov & Tkachev, 2006; Gorbunov & Shaposhnikov, 2007; Shaposhnikov, 2007, 2008; Laine & Shaposhnikov, 2008) and in two excellent recent reviews (Boyarsky et al., 2009d; Kusenko, 2009). In ν MSM the lightest sterile neutrino plays the role as keV-mass dark matter and hence it will be the focus in the following sections.

The Lagrangian for ν MSM is (Boyarsky et al., 2009d):

$$\mathcal{L} = \mathcal{L}_{SM} + \bar{\nu}_{s,a}(i\partial_\mu\gamma^\mu)\nu_{s,a} - y_{\alpha a}H\bar{L}_\alpha\nu_{s,a} - \frac{M_{aa}}{2}\bar{\nu}_{s,a}^c\nu_{s,a} + \text{h.c.}, \quad (3.2)$$

where \mathcal{L}_{SM} is the Standard Model Lagrangian with massless left-handed neutrinos (e.g. from Amsler et al., 2008). α denotes the lepton doublets ($\alpha = e, \mu, \tau$), a denotes the additional singlets ($a = 1, 2, \dots, N$), H is the Higgs field, y are the Yukawa couplings, and M_{aa} is the mass matrix for the singlets as discussed below.

Similar to the Standard Model fermions and quarks, the neutrinos in ν MSM acquire Dirac masses via Yukawa couplings plus a possible Majorana mass term specifically for the sterile neutrinos. The smallness of the active neutrino masses is obtained via the seesaw mechanism (as explained in e. g. Amsler et al., 2008; Kusenko, 2009). The mass elements are given by:

$$M_{aa} = \begin{pmatrix} 0 & D_{3 \times N} \\ D_{3 \times N}^T & M_{N \times N} \end{pmatrix}, \quad (3.3)$$

where $D_{\alpha a} = y_{\alpha a}\langle H \rangle$ are the Dirac masses from a spontaneous symmetry breaking given by the Yukawa couplings, and M are the right handed Majorana masses.

The Majorana masses are undetermined from neutrino experiments (too many unknown parameters) and also the origin of the Yukawa coupling values is unknown. If the Yukawa couplings are of the order of one, the Majorana mass terms have to be much larger than the electro-weak scale (GeV) in order to obtain the experimentally inferred active neutrino masses (active neutrino masses are suppressed by $\langle H \rangle / M$). If one instead chooses very small Yukawa couplings ($y < 10^{-6}$), the sterile neutrino mass eigenstates becomes of the order of keV – GeV. These are much heavier than the eV sterile neutrino proposed to explain the findings of the LSND experiments (de Gouvea, 2005).

The smallness of the Yukawa couplings gives all three sterile eigenstates masses below the electro-weak scale (few hundred GeV). If the two heaviest states are closely degenerate at the 0.1 – 10 GeV scale, the CP-violating effects in the sterile neutrino oscillations are enhanced which allows to generate a significant lepton asymmetry in the early Universe from out-of-equilibrium decays of the two heavy states (Laine & Shaposhnikov, 2008). The lepton asymmetry can be transferred to the baryons explaining the baryon asymmetry of the Universe (Asaka & Shaposhnikov, 2005; Asaka et al., 2006a). Decays of the two heavy mass eigenstates distorts the spectra of the active neutrinos. If this happens close to the time of the BBN, the nuclei formation can be changed significantly. This is prevented for lifetimes shorter than $\tau_{2,3} < 0.1$ sec, by giving the decay products enough time to thermalise before BBN (Dolgov et al., 2000).

3.2.5 TWO-TYPE NEUTRINO MIXING

In ν MSM, the active-sterile neutrino mixing is dominated by mixing with only one type of active neutrinos due to the non-degeneracy of the masses (Lesgourgues & Pastor, 2006). Consequently the two-type neutrino mixing described in the following is a good approximation and it can of course be generalised to three or more types (Kayser, 2008).

With two types of neutrinos, here chosen as an active and a sterile neutrino (without loss of generality), the neutrino mixing can be described with only one mixing angle in vacuum, θ (Kayser, 2008):

$$\begin{pmatrix} \nu_\alpha \\ \nu_s \end{pmatrix} = \begin{pmatrix} \cos(\theta) & \sin(\theta) \\ -\sin(\theta) & \cos(\theta) \end{pmatrix} \begin{pmatrix} \nu_1 \\ \nu_2 \end{pmatrix}, \quad (3.4)$$

where ν_α and ν_s are flavour eigenstates, and ν_1 and ν_2 are a light and a heavy mass eigenstate. For $\theta = 0$ there is no mixing and the flavour eigenstates are identical to the mass eigenstates. If $\theta \neq 0$ and you try to measure the mass of ν_α many times by a weak interaction experiment, most of the outcome will be the mass of ν_1 , but a few times you will get ν_2 as shown in Fig. 3.3. The effective mass is thus a weighted average. Among the active neutrinos, the mixing angle is significant as opposed to the quark sector, where the mixing angles are very small (Amsler et al., 2008).

Sometimes neutrino mixing is referred to as neutrino oscillations, because the probability of measuring a given flavour oscillates with distance (time) and energy (Kayser, 2008):

$$P(\nu_s \rightarrow \nu_\alpha) = \frac{1}{2} \sin^2(2\theta) \left(1 - \cos\left(\frac{\Delta m^2 L}{2E_\nu}\right) \right), \quad (3.5)$$

where L is the propagated length, E_ν is the neutrino energy and Δm^2 is the difference of the masses squared. The probability of detecting an $\bar{\nu}_e$ in an originally pure $\bar{\nu}_\mu$ beam as a function of distance is shown in Fig. 3.3. Often the expression "mixing angle" denotes $\sin^2(2\theta)$ instead of θ . In matter, the mixing is suppressed or enhanced by quantum mechanical effects (Kayser, 2008).

By regarding all decay branches possible through oscillations, the mean lifetime of a sterile pure Dirac neutrino of mass, m_s , has been determined to be (Barger et al., 1995; Dolgov et al.,

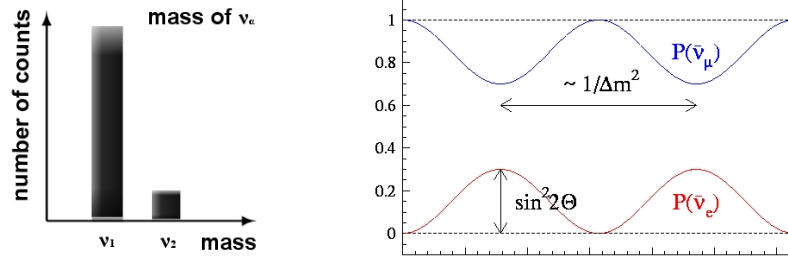


Figure 3.3: (Left) An interaction dependent measurement of the mass of ν_α in a two-type mixing scenario, with mass eigenstates ν_1 and ν_2 . A corresponding interaction independent measurement would give a weighted average. (Right) The probability of detecting an $\bar{\nu}_e$ in an originally pure $\bar{\nu}_\mu$ beam as a function of distance.

2000):

$$\tau = \frac{1}{\Gamma_{tot}} = \frac{f(m_s) \times 10^{20}}{(m_s/\text{keV})^5 \sin^2(2\theta)} \text{ sec}, \quad (3.6)$$

where Γ_{tot} is the total decay rate. $f(m_s)$ takes into account the open decay channels so that for $m_s < 1 \text{ MeV}$, where only decay channels to neutrinos are open, $f(m_s) = 0.86$, but for $m_s > 2m_e \approx 1 \text{ MeV}$ also the e^+e^- -channel is open and $f(m_s) = 1$. In this thesis, only the case where $m_s < 1 \text{ MeV}$ has been considered. If the sterile neutrinos are pure Majorana particles, and hence their own anti-particles, the number of available decay modes is doubled, and their lifetime is shorter by a factor of two.

3.3 OBSERVATIONAL SIGNATURES

Via the neutrino mixing, the sterile neutrinos acquire several testable signatures as outlined in the forthcoming sections. The most direct is an emission line in X-ray, but also the structure formation is affected, which potentially can be detected through observations of the Lyman α forest.

3.3.1 RADIATIVE DECAY

The dominating decay of the sterile neutrinos is into three low energetic active neutrinos (Barger et al., 1995). Unfortunately it is a very challenging signature to detect experimentally. If $m_s > m_\alpha$ the radiative decay $\nu_s \rightarrow \nu_\alpha + \gamma$ becomes allowed. The decay is achieved by ν_s virtually transforming itself into two charged particles shown in Fig. 3.4. This is possible if the mass eigenstate of the sterile neutrino couples to a W boson and transforms it into a charged lepton (Kayser, 2008; Pal & Wolfenstein, 1982). One of the charged particles emit a photon and the two charged particles recombine to form an active neutrino.

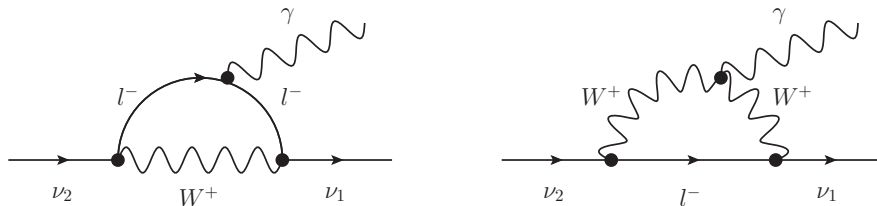


Figure 3.4: The Feynman diagrams for a ν_s virtually transforming itself into two charged particles by the coupling of the mass eigenstate to a W boson and thereby decaying radiatively (Pal & Wolfenstein, 1982; Kusenko, 2004).

Due to the kinematics of the reaction, the photon is mono-energetic and the energy in the ν_s rest frame can be determined from energy and momentum conservation (two-body decay, Amsler et al., 2008):

$$E_\gamma = \frac{1}{2}m_s \left(1 - \frac{m_\alpha^2}{m_s^2}\right). \quad (3.7)$$

If $m_s \gg m_\alpha$, which is likely since $\sum_\alpha m_\alpha \lesssim 0.6$ eV (Komatsu et al., 2009) and m_s is of the order of keV, then $E_\gamma \approx m_s/2$.

The branching ratio for the radiative decay has been derived to be (Barger et al., 1995):

$$\frac{\Gamma_\gamma}{\Gamma_{tot}} = \frac{27\alpha}{8\pi} \approx \frac{1}{128}. \quad (3.8)$$

3.3.2 STERILE NEUTRINO DARK MATTER MASS

The radiative decay is a testable signature of the sterile neutrinos as dark matter. Since no cut-off has been detected in the observed matter power spectrum at small scales, there is no a priori favoured mass for the dark matter. Assuming all of the dark matter to be sterile neutrinos, a lower limit on the mass can be derived from phase space considerations. The sterile neutrinos are fermions and consequently they obey the Fermi statistics providing a limit for how close they can be squeezed together in dark matter halos of a given size (Tremaine & Gunn, 1979; Lin & Faber, 1983; Dalcanton & Hogan, 2001; Petraki, 2008; Boyanovsky, 2008; Gorbunov et al., 2008; Boyarsky et al., 2009c; Angus, 2009). Applied to dwarf galaxies the very conservative result is $m_s \gtrsim 0.49$ keV, which for specific assumptions on the primordial phase space distribution, can be strengthened to $m_s \gtrsim 1.0 - 1.8$ keV (Boyarsky et al., 2009c). For this reason, the mono-energetic emission line is expected to lie in the X-ray energy range. Current X-ray observatories have a sensitivity interval of $E_\gamma = 0.3 - 10$ keV corresponding to masses of $m_s = 0.6 - 20$ keV.

The optical components of a galactic or cluster halo have velocity dispersions of the order of $v/c \approx 10^{-5}$ to 10^{-4} (Smith et al., 2001). The dark matter is assumed to have the same velocity dispersion and consequently any broadening due to motion can be neglected since it is of the order of $E_{obs}/E_{em} = 1.0001$, which is much smaller than the instrumental resolution.

3.3.3 CONSTRAINING THE DECAY RATE FROM EMITTED PHOTONS

If no emission line is detected, the flux emitted from a given clump of matter can be converted into a constraint on the decay rate of dark matter particles radiatively decaying with $E_\gamma = m/2$.

The number of dark matter particles of mass m in a clump of matter is $N = M_{tot}/m$, where M_{tot} is the mass of dark matter (usually taken to be the total mass within the field of view). The luminosity can be expressed as $\mathcal{L} = E_\gamma N \Gamma_\gamma$, where E_γ is the photon energy and Γ_γ is the decay rate of the radiative decay. Then the flux at a luminosity distance, D_L , is:

$$F = \frac{\mathcal{L}}{4\pi D_L^2} = \frac{E_\gamma N \Gamma_\gamma}{4\pi D_L^2} = \frac{M_{tot} \Gamma_\gamma}{8\pi D_L^2}, \quad (3.9)$$

where the last equality specifically assumes $E_\gamma = m/2$. The observed flux, F_{det} , gives an upper limit for the flux from decaying dark matter so Eqn. 3.9 can be rewritten as:

$$\Gamma_\gamma^{max} \leq \frac{8\pi F_{det} D_L^2}{M_{tot}} = 1.34 \times 10^{-4} \text{ sec}^{-1} \left(\frac{F_{det}}{\text{erg/cm}^2/\text{sec}} \right) \left(\frac{D_L}{\text{Mpc}} \right)^2 \left(\frac{M_{tot}}{M_\odot} \right)^{-1}, \quad (3.10)$$

which is useful in the common case of no observed emission line (see Ch. 4).

3.3.4 LYMAN α CONSTRAINTS

Dark matter is governing the structure formation and consequently its properties can be constrained from the matter distribution in the Universe. The Lyman α forest provides a powerful method of mapping the matter distribution. Here I briefly introduce the general idea before its implications for the sterile neutrinos are discussed in the next section.

The Lyman α forest is a series of absorption lines seen in the spectra of distant quasars due to absorption in neutral hydrogen clouds at different redshifts along the line of sight (see Fig. 3.5). The amount of absorption is proportional to the local hydrogen density. Assuming the dark matter density distribution to follow that of the gas down to the scale where the gas becomes pressure supported, the Lyman α forest becomes a very powerful method to map the density fluctuations on scales $k \approx 0.1 - 5h \text{ Mpc}^{-1}$ for redshifts $z \approx 2 - 4$.

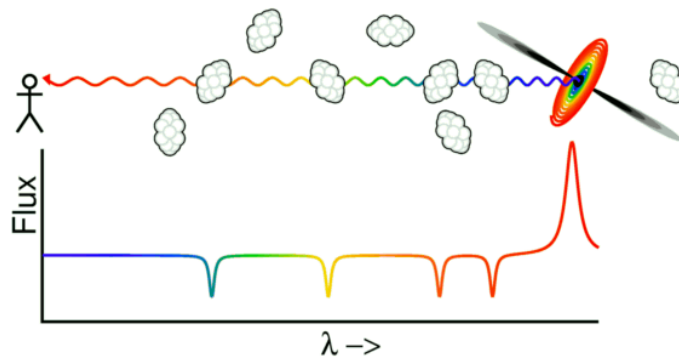


Figure 3.5: The emission of a distant quasar is absorbed in natural hydrogen clouds at different redshifts along the line of sight leading to a Lyman α forest in the spectrum (Wright, 2004).

Large observational surveys such as the Sloan Digital Sky Survey (SDSS, The SDSS Collaboration, 2009) determine the flux power spectrum (defined similar to the matter power spectrum in Eqn. 3.1), so in principle all you have to do is to use the cosmological model with your favourite dark matter candidate to predict a flux power spectrum and compare it to the data. Unfortunately, the prediction of the flux power spectrum relies on a large number of assumptions and the many free parameters requires a simultaneous fit to the Lyman α data combined with other cosmological probes such as CMB.

At $z \approx 2 - 4$ the gravitational collapse of the dark matter fluctuations is already mildly non-linear introducing a non-linear bias between the flux and matter power spectra. Consequently it is necessary to perform hydrodynamical simulations both to simulate the non-linearity and to relate the flux and matter power spectra. State of the art hydrodynamical cosmological simulations are very computer intensive and with the large set of cosmological parameters it is not possible to perform a simulation for each parameter variation. Instead, one has to do with a grid of 10-20 simulations for a variation of few key parameters (e. g. the dark matter particle mass or average velocity), for which the flux power spectra are predicted. For parameter values between the simulations, the flux power spectra can be obtained by interpolation. For each set of key parameter values to be investigated, the probability for the the given model to be "true" can be achieved comparing the flux power spectrum from the simulation to the observed ones combined with the WMAP 5-years observations (using e. g. CosmoMC, Lewis & Bridle, 2002).

The relation between the flux and matter power spectra depends on the initial velocity distribution of the dark matter. The mixing angles of the sterile neutrinos are sufficiently small that they are never in thermal equilibrium and consequently they have a non-thermal primordial velocity distribution with the details depending on the production scenario. Consequently, using the Lyman α forest to constrain the sterile neutrinos depends heavily on the assumed production

mechanism (Boyarsky et al., 2009a).

3.4 DIFFERENT SCENARIOS AND THEIR CONSTRAINTS

There are several ways the sterile neutrinos can be produced in the early Universe each leading to different kinematics and clustering properties for the same mass. The X-ray flux constraints described in Sec. 3.3.3 are not very sensitive to the details production scenario. However, the Lyman α constraints are very sensitive to the production mechanism via the initial velocity distribution of the dark matter. In this section, the most important scenarios and their observational constraints are discussed.

3.4.1 LINE EMISSION CONSTRAINTS

Fig. 3.6 illustrates a combination of all current observational and cosmological constraints in the $m_s - \sin^2(2\theta)$ parameter space of the sterile neutrinos. The upper right corner (blue) has been excluded from X-ray and soft γ -ray line searches as described in Sec. 3.3.3 and Ch. 4. They are not sensitive to the production mechanism of the sterile neutrinos as long as the sterile neutrinos are assumed to account for all of the dark matter. If more than one type of dark matter exist, the line search constraints weakens according to the sterile neutrino dark matter percentage.

The Dodelson-Widrow scenario (described in Sec. 3.4.2) is the only scenario, where the production of the sterile neutrinos is directly related to the mixing angle. However, the oscillations exist in all cases and hence the sterile neutrinos can decay to photons (X-rays) no matter how they are produced, which thus provides the most model independent constraints.

3.4.2 OSCILLATIONS - THE DODELSON-WIDROW SCENARIO

The simplest production mechanism for the sterile neutrinos is via the neutrino oscillations in lepton-lepton collisions. Dodelson & Widrow (1994) originally proposed this scenario assuming a negligible lepton asymmetry, a small mixing angle, the initial number density to be zero, and oscillations to be the only production mechanism. The sterile neutrinos are never in thermal equilibrium and consequently they are not the product of a freeze out. Instead, they are produced at relatively low temperatures ($\lesssim 1$ GeV) from interactions with the active neutrinos, so their momentum distribution is proportional to that of the active neutrinos. Numerical calculations of the resulting energy density gives (Dodelson & Widrow, 1994; Abazajian et al., 2001a,b; Dolgov & Hansen, 2002; Abazajian, 2006; Asaka et al., 2007):

$$\Omega_s \approx 0.2 \left(\frac{\sin^2(2\theta)}{4 \times 10^{-8}} \right) \left(\frac{m_s}{\text{keV}} \right)^{1.8}. \quad (3.11)$$

In Fig. 3.6 the dark blue band represents Eqn. 3.11 assuming the sterile neutrinos to provide the total observed dark matter energy density. Above this line, sufficiently sterile neutrinos are produced to over-close the Universe, which is in contradiction with the findings from CMB which points towards a flat Universe (Hinshaw et al., 2009).

The velocity distribution of sterile neutrinos produced through oscillations is a modified Fermi-Dirac function (similar in shape to thermal relics). A large number of Lyman α analyses have been carried out for oscillatory produced sterile neutrinos (for references see caption of Fig. 3.5) leading to mass constraints as high as $m_s > 14$ keV (Seljak et al., 2006). A conservative approach with focus on the statistics for the parameter selection and systematic errors resulted in $m_s > 8$ keV (frequentist 99.7% confidence limit, Boyarsky et al., 2009a).

From Fig. 3.6 it is seen, that if the sterile neutrinos are assumed to account for all dark matter, the Dodelson-Widrow scenario is in conflict with the combined constraints from X-rays and Ly-

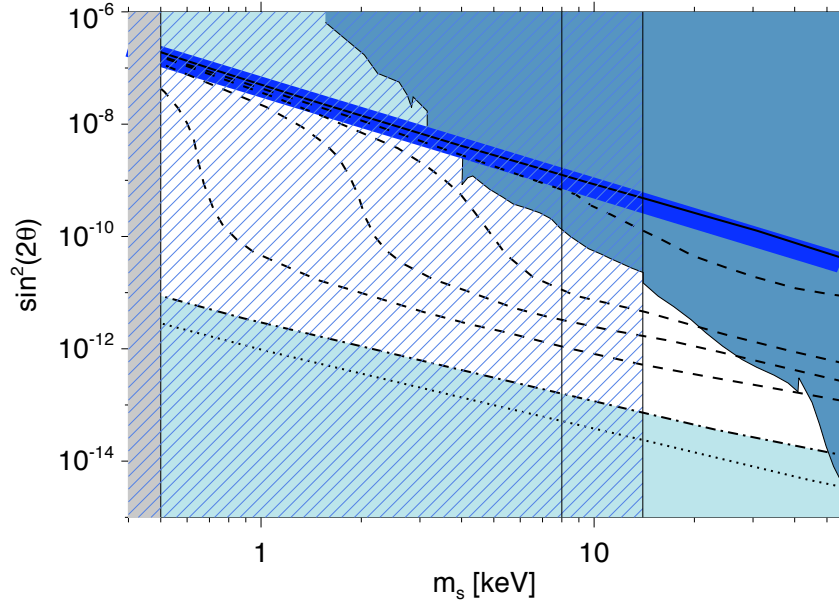


Figure 3.6: Sketch of all current observational and cosmological constraints. **Phase space:** grey, from Tremaine & Gunn (1979); Dalcanton & Hogan (2001); Petraki (2008); Boyanovsky (2008); Gorbunov et al. (2008); Boyarsky et al. (2009c); Angus (2009), **X-ray:** blue, from Riemer-Sørensen et al. (2006, 2007a); Abazajian et al. (2007); Boyarsky et al. (2008c); Riemer-Sørensen & Hansen (2009) using Chandra data, from Boyarsky et al. (2006a,b,c); Watson et al. (2006); Boyarsky et al. (2007a,b, 2008a) using XMM data, from Boyarsky et al. (2008b) using INTEGRAL SPI data, from Loewenstein et al. (2009) using Suzaku data. **Lyman α :** hatched blue, the vertical lines are $m_s < 8$ keV and $m_s < 14$ keV, from Narayanan et al. (2000); Viel et al. (2005, 2008); Seljak et al. (2006); Boyarsky et al. (2009a,b). **Dodelson-Widrow production:** clear blue band, from Dodelson & Widrow (1994); Abazajian et al. (2001a,b); Dolgov & Hansen (2002); Abazajian (2006); Asaka et al. (2007). **Resonant production:** solid line for $L_6 = 0$, dashed lines for $L_6 = 4, 12, 25, 70$ from above, dot-dashed line for $L_{max} = 700$, and dotted line for $L_{BBN} = 2500$, from Laine & Shaposhnikov (2008).

man α . Boyarsky et al. (2009a) showed that if the oscillatory produced sterile neutrinos contribute with more than 60% of the dark matter, the scenario can be ruled out.

Sterile neutrinos with a keV-mass are produced near the QCD phase transition in the early Universe, which might change the production rate by a few percent and thereby weakening the Lyman α constraints slightly, but not enough to avoid the conflict (Dolgov & Hansen, 2002; Abazajian, 2006; Asaka et al., 2007).

Asaka et al. (2006b) proposed that additional entropy produced after the sterile neutrinos would dilute their momentum distribution. In Riemer-Sørensen et al. (2006) we considered the observational consequences and concluded that such an entropy increase would strengthen the observational X-ray constraints and weaken the Lyman α constraints (see Sec. 4.2).

3.4.3 RESONANT PRODUCTION

If the lepton asymmetry is non-zero, the sterile neutrinos can be produced in greater abundance through oscillations at the Mikheev-Smirnov-Wolfenstein resonance (MSW, Wolfenstein, 1978; Mikheev & Smirnov, 1985; Shi & Fuller, 1999). The average momentum of the MSW produced sterile neutrinos is lower than for the ordinary oscillatory produced ones rendering it an overall colder dark matter candidate (see Fig. 3.7, Kishimoto & Fuller, 2008). The needed lepton asym-

metry can be produced by decays of the heavier sterile neutrinos. It is characterised in terms of $L_6 = 10^6(n_{\nu_e} - n_{\bar{\nu}_e})/s$, where the n_{ν_e} are the neutrino number densities, and s the entropy. The maximal value which can be generated through the decays corresponds to $L_6 \approx 700$ (Laine & Shaposhnikov, 2008). Lepton asymmetries of this order of magnitude is safely below the maximal value of $L_6 \lesssim 2500$ leading to a successful BBN (Dolgov et al., 2002).

The dashed/dotted lines in Fig. 3.6 shows $\sin^2(2\theta)$ as a function of mass for values of $L_6 = 0 - 2500$ leading to the observed dark matter energy density. It is seen that for obtainable lepton asymmetries only $m \lesssim 50$ keV is allowed due to the line emission constraints (Fig. 3.6, Laine & Shaposhnikov, 2008). The light blue area below the $L_6 = 700$ line (dot-dashed) is excluded because in this region it is not possible to generate enough sterile neutrinos to account for all of the dark matter neither through oscillations nor through resonant production.

Currently there has not been performed any Lyman α analyses specifically for resonantly produced sterile neutrinos, but an analysis combining CDM and WDM can be used to infer some results because the resonant production will modify the initial velocity distribution by adding a narrow peak at low velocities as shown in Fig. 3.7 (Boyarsky et al., 2009a,b). The resulting matter power spectra have a step and a plateau rather than the classical WDM cut-off. They are very similar to those of a thermal relic made up of mixed WDM and CDM down to scales smaller than those resolved by current Lyman α data. Boyarsky et al. (2009b) concluded that for each mass of $m_s \gtrsim 2$ keV there is at least one value of the lepton asymmetry, for which the resonantly produced sterile neutrinos are compatible with the Lyman α data, the X-ray constraints, and all other cosmological requirements (e. g. the lepton asymmetry does not change BBN), and with the lepton asymmetry naturally produced within the model.

3.4.4 PRODUCTION AT THE ELECTRO-WEAK SCALE

The sterile neutrinos can also be produced at the electro-weak scale by decays of a gauge singlet Higgs boson with mass above 100 GeV. This is possible if the Majorana mass terms of the sterile neutrinos arises from the Higgs mechanism with the Higgs singlet coupling to the neutrinos thus acquiring a vacuum expectation value (Kusenko, 2009). The so produced dark matter sterile neutrinos will have a velocity distribution similar to the resonantly produced ones, which on average is colder than those produced by oscillations because they remain out of equilibrium while their

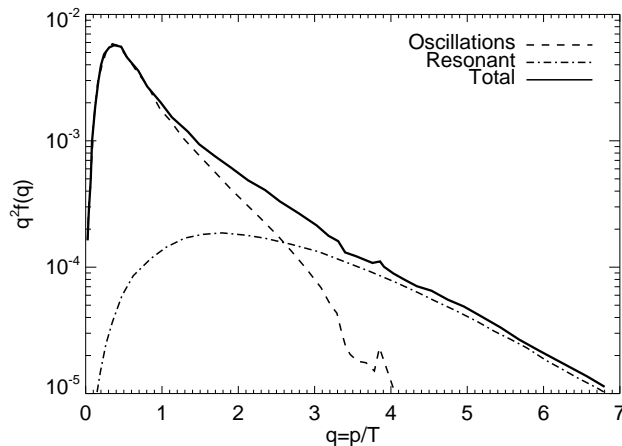


Figure 3.7: The velocity distribution for a 3 keV sterile neutrino produced through oscillations and resonantly with a lepton asymmetry of $L_6 = 16$ (Boyarsky et al., 2009b).

momenta are redshifted due to entropy production as the number of degrees of freedom in the early Universe decreases. The resulting energy density is independent of the neutrino oscillations (Petraki & Kusenko, 2008; Shaposhnikov & Tkachev, 2006):

$$\Omega_s \approx 0.2 \left(\frac{y}{10^{-8}} \right)^3 \left(\frac{\langle S \rangle}{m_s} \right) \left(\frac{33}{\xi} \right), \quad (3.12)$$

where y is the Yukawa coupling of the sterile neutrinos, $\langle S \rangle$ is the mean of the gauge singlet mass, and ξ is the dilution factor since the production.

The Majorana masses of the sterile neutrinos can be a fundamental parameter of the theory, or it can arise from the Higgs mechanism (Chikashige et al., 1980), which can make the sterile neutrinos a colder dark matter candidate than for creation through oscillations because the abundance becomes mainly dependent on the Higgs singlet mass scale.

3.4.5 ALTERNATIVE SCENARIOS

The sterile neutrinos can also be produced from their couplings to e. g. the inflaton (Shaposhnikov & Tkachev, 2006). The resulting thermal velocity distribution then depends on the mass of the inflaton and the time of production, and can easily be tuned to be either warm or cold from a theoretical point of view.

In case the sterile neutrinos are not the main component of the dark matter, they are in all scenarios produced in the early Universe, and thus every dark matter halo should contain some fraction if they exist.

Introducing alternative production scenario affects some of the constraints plotted in Fig. 3.6. The Lyman α constraints (dashed) only applies to sterile neutrinos with a Fermi-Dirac like velocity distribution. The lower bound on the mixing angle (light blue) might change depending on the co-produced lepton asymmetry. However, the co-produced lepton asymmetry must never violate the BBN ($L_6 \lesssim 2500$). The upper limits on the mixing angle are more solid. The sterile neutrinos can always be produced through oscillations, so mixing angles above the dark blue Dodelson-Widrow band are excluded as long as the sterile neutrinos are assumed to account for all of the dark matter, because larger mixing angles would lead to an overproduction of dark matter. Similarly the sterile neutrinos can always decay via the oscillations, so the only way to change the X-ray constraints is if the sterile neutrinos does not account for all of the dark matter. The Tremaine-Gunn limit (grey) relies on the sterile neutrinos being fermions and accounting for all of the dark matter.

4

OBSERVATIONAL CONSTRAINTS ON STERILE NEUTRINOS

This chapter treats my work on emission line constraints (Riemer-Sørensen et al., 2006, 2007a; Riemer-Sørensen & Hansen, 2009) with a comparison to other published constraints. Apart from Sec. 4.1 on line emission in general, the sections follow the chronological order of my work. A possible signal from decaying sterile neutrinos should ideally be looked for in nearby objects with the largest possible amount of dark matter within the field of view, and low X-ray noise from baryons. The Milky Way halo is the nearest dark matter dominated object we know and is treated in Sec. 4.2. Colliding clusters of galaxies provides very dark matter dense regions with very low noise from X-ray emitting gas. In Sec. 4.3 the colliding cluster Abell 520 is explored. Another option is to improve the instrumental resolution. The difficulties with this are explained in Sec. 4.4. Finally Sec. 4.5 treats the first X-ray observation of a Milky Way dwarf galaxy, which are the objects with the best ratio between distance, mass, and noise level.

4.1 LINE EMISSION

The decay rate of any dark matter candidate with a radiative two-body decay can in the case of non-detection be constrained from astronomical observations of dark matter concentrations (Abazajian & Koushiappas, 2006; Boyarsky et al., 2009d, and references therein). The strongest constraints are obtained from studying dark matter dominated regions, using instruments with high spectral resolution. The decay line is expected only to suffer negligible broadening due to the motion of the dark matter. From X-ray observations of galaxy clusters the dark matter velocity dispersion can be found by solving the hydrostatic and Jeans equations. The resulting velocity dispersion has a peak at approximately 500 km sec^{-1} , leading to a line broadening which is negligible compared to the instrumental spectral resolution (Navarro et al., 1996; CXO Proposers' Observatory Guide, 2008).

4.1.1 DISTINGUISHING BETWEEN EMISSION LINES ORIGINS

Due to background emission and instrumental response, the observed spectra always contain emission lines. The question is how they can be distinguished from a possible dark matter signal. Fig. 4.1 shows a spectrum of a *Chandra* observation where the telescope was stowed behind a lid, so all features are either internal or due to particles penetrating the lid. The internal line features originate from fluorescence of materials in the telescope and focal plane.

In a given spectrum with low baryonic noise, like the example in Fig. 4.2, most line features can be identified to have an instrumental origin. However a decay line from dark matter could "hide"

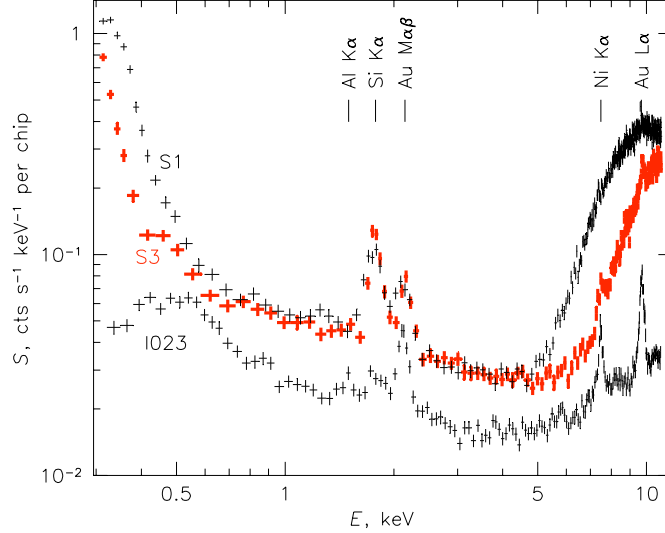


Figure 4.1: Spectra of Chandra observations with ACIS in the stowed position (the different spectra are from the different CCD types onboard Chandra). Line features are due to fluorescence of material in the telescope and focal plane (CXO Proposers' Observatory Guide, 2008) or due to particles penetrating the lid.

under one of these prominent features. In this case, the energy of the decay line is redshifted by a factor of $(1+z)$ in the spectrum of a dark matter region at a given redshift, z . In Riemer-Sørensen et al. (2006) I tested for hidden lines by comparing the blank sky spectrum ($z = 0$) in Fig. 4.2 to those of the outskirts of the clusters Abell 478 and Abell 383 shown in Fig. 4.3. In the blank sky spectrum the line features at $E_\gamma = 1.74$ keV, $2.1 - 2.2$ keV, and 7.47 keV are identified as the Si $K\alpha$, the Au $M\alpha\beta$ complex, and Ni $K\alpha$ respectively.

I optimised the ratio between expected dark matter signal and baryonic emission from hot intracluster gas by extracting spectra from the cluster outskirts. The X-ray emission from hot intracluster gas is proportional to the gas density squared, whereas the emission of photons from dark matter is directly proportional to the dark matter density. Specifically, I extracted spectra from an outer radial bin, defined by optimising the ratio of matter in the field of view to the X-ray emission from the intracluster gas ("noise") parametrised by fitting the surface brightness profile, $S(R)$, with a β -model:

$$S(R) = S_0 \left(1 + (R/r_c)^2\right)^{-3\beta+1/2}. \quad (4.1)$$

The outer radius was chosen as the radius with the optimal ratio (which is very close to the edge of the ACIS-S3 chip) and the inner radius was chosen so the signal to noise ratio had a value of half the optimal value. The spectra and corresponding redshifted energies are shown in Fig. 4.3¹.

For Abell 487 with a redshift of $z = 0.0881$ (Vikhlinin et al., 2006), the lines should be redshifted to $E_\gamma = 1.5$ keV, 1.8 keV, and 6.9 keV if they have a cluster origin. As seen in the left part of Fig. 4.3 there are no obvious line features at these energies (marked by arrows). For Abell 383 with $z = 0.1883$ (Vikhlinin et al., 2006), the lines should be redshifted to $E_\gamma = 1.2$ keV, 1.7 keV, and 6.3 keV. There is a visible line at $E_\gamma \approx 1.7$, but this line is the original instrumental Si $K\alpha$

¹After finishing this analysis a related paper appeared (Boyersky et al., 2006b) where an analysis using exactly this method of looking at the outer cluster region was made.

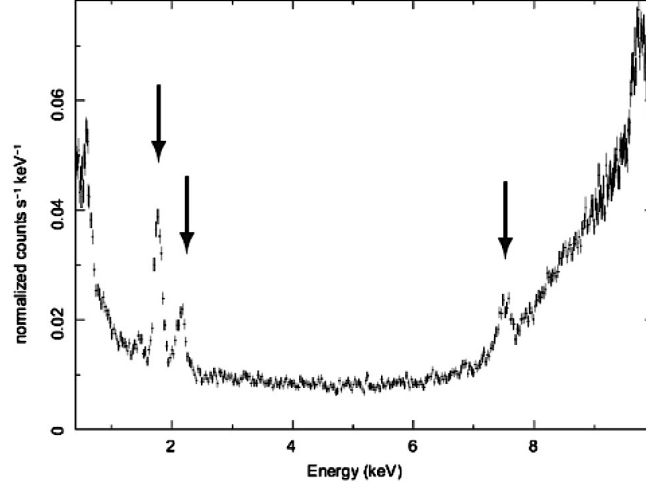


Figure 4.2: The blank spectrum with the the line features at $E_\gamma = 1.74$ keV, $2.1 - 2.2$ keV, and 7.47 keV identified as the Si $K\alpha$, the Au $M\alpha\beta$ complex, and Ni $K\alpha$, respectively.

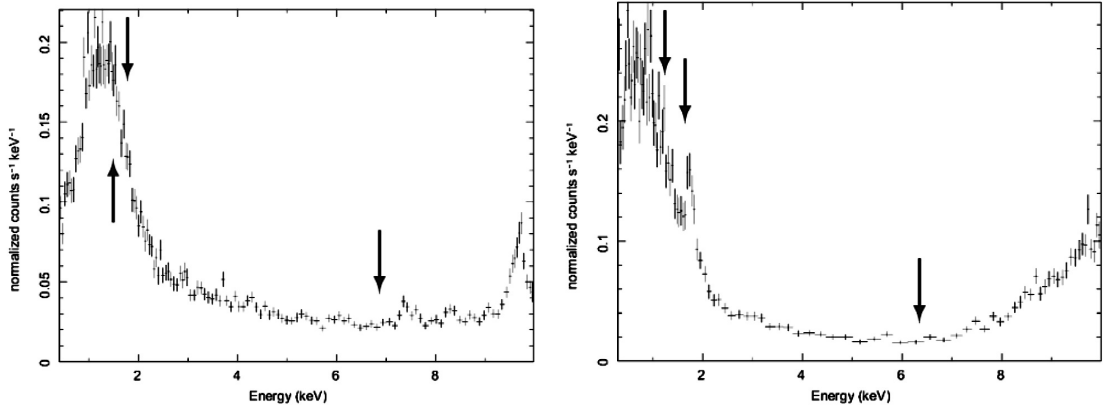


Figure 4.3: The spectra of the outer parts of Abell 478 (Left) and Abell 383 (Right) with the line feature energies from Fig. 4.2 marked by arrows at the corresponding redshifted energies.

line, so Abell 383 is not suitable for checking whether there is an emission line hiding under the Au $M\alpha\beta$ complex.

In the case where a "moving" line had been found in the spectra, it would probably origin in standard physical processes of the observed object as the redshifting of course applies to all types of emission lines.

4.2 THE MILKY WAY DARK MATTER HALO

This section is a brief reminder of the results presented in Riemer-Sørensen et al. (2006). The work was done as part of my Master degree, but is included here for completeness².

4.2.1 BLANK SKY DATA

The Milky Way is generally believed to be embedded in a dark matter halo, which is both massive, X-ray quiet, and definitely very nearby, making it an obvious target for studying decaying

² Λ CDM parameter values: $H_0 = 70$ km sec⁻¹ Mpc⁻¹, $\Omega_M = 0.30$

sterile neutrinos. In normal astronomical observations the local emission from the halo and unresolved sources is treated as background and consequently it is well observed. Approximately 400 ksec of *Chandra* observations of different regions of the sky without known X-ray sources, have been combined into a set of blank sky data which is provided with CIAO.

I analysed the ACIS-S3 part of the blank sky data set D2000-12-01, created during 2001 (*Chandra* X-ray Centre, 2009f). The intrinsic background level of the ACIS-I chips is slightly lower than the background level of ACIS-S3 (CXO Proposers' Observatory Guide, 2008), but as we wanted to compare the blank sky spectrum with source spectra usually extracted from ACIS-S3, we chose this chip.

The data preparation process described in Sec. 2.3.3 is somewhat simplified for blank sky data. Sources identifiable by eye are already marked out in the creation of the blank sky data files, so no extra point source removal is needed. Also only good "non-flaring" time intervals have been used and all time stamps have been set to zero, so it is not possible to clean the light curve further (*Chandra* X-ray Centre, 2009f).

The spectrum was extracted for a region of $8.4 \text{ arcmin} \times 8.4 \text{ arcmin}$. The extracted spectrum is shown in Fig. 4.4 for $E = (0.8 - 9.0) \text{ keV}$. The line features were examined as explained in Sec. 4.1.1.

4.2.2 MODEL FITTING AND LINE FLUX DETERMINATION

The blank sky spectrum was well fitted (reduced $\chi^2 = 1.1$ for 540 d. o. f.) by a composite model consisting of an exponential plus a power law plus four Gaussians at the locations of the most prominent instrumental lines. Since the model was only used to determine the flux and not to derive any physical parameters, its composition was chosen to provide the best possible fit.

A hypothetical mono-energetic emission line in the spectrum was represented by a Gaussian, centered at the line energy, and with a width, σ , given by the instrumental spectral resolution: $\sigma \approx 0.1 \text{ keV}$ for $0.3 \text{ keV} \leq E < 6.0 \text{ keV}$ and $\sigma \approx 0.15 \text{ keV}$ for $6.0 \text{ keV} \leq E < 8.0 \text{ keV}$ (CXO Proposers' Observatory Guide, 2008).

For each energy in steps of 0.05 keV , the hypothetical line was defined with maximum at the model value of the fit to the broadband spectrum. An example is shown in Fig. 4.4. The flux of this Gaussian was calculated thus providing an upper limit of emission from decaying dark

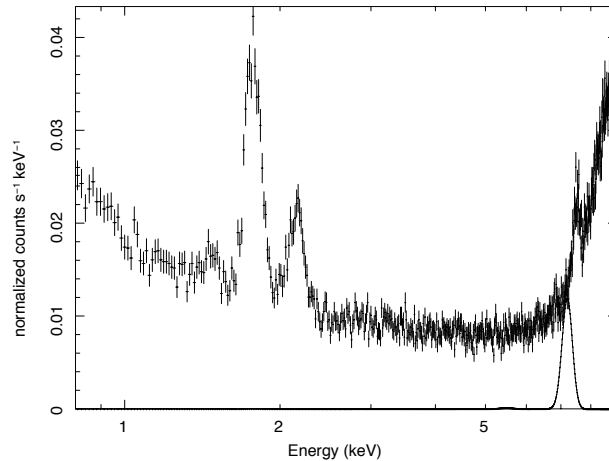


Figure 4.4: The blank sky ACIS-S3 spectrum – i.e. a view through the Milky Way halo. Also shown is the maximal single Gaussian emission line from decaying dark matter at a specific energy.

matter at the given energy. This is a model independent and very conservative analysis, since any X-ray emitters within the field of view, and background, contributes to the extracted spectrum. If we instead only allowed the decay signal from potential decaying dark matter to produce a bump above the "base line" spectrum, we could improve the bounds by a large factor (Boyarsky et al., 2006a). However, this approach would depend sensitively on the robustness of modelling the background and emissions from sources contributing to the base line spectrum.

4.2.3 OBSERVED HALO MASS AND MEAN DISTANCE

The amount of dark matter within the observed field of view is only a minute fraction of the total mass of the galactic halo. The density distribution of the Milky Way was assumed to follow a standard NFW-profile (Eqn. 1.4) with the total mass of the Milky Way halo taken to be $M_{tot}^{halo} = 10^{12} M_{\odot}$ for scale and virial radii of $r_s = 21$ kpc and $r_{vir} = 256$ kpc respectively, and the solar distance $R_{\odot} = 8$ kpc (Klypin et al., 2002). The average distance to the halo mass was determined to be $D_L^{halo} = 35$ kpc by integration of the density profile.

Changing the details of the NFW-profile does not significantly affect our results (e. g. changing the inner density slope between -1 and zero, or changing the outer slope between -3 and -4 , changes the predicted signal by less than a factor of 2). There is also an uncertainty, possibly as large as a factor of 2, arising from using the value of $M_{vir} = 10^{12} M_{\odot}$.

4.2.4 DECAY RATE OF STERILE NEUTRINOS IN THE MILKY WAY HALO

From the blank sky flux, an upper limit on the decay rate was derived as a function of line energy using Eqn. 3.10. The result is plotted in Fig. 4.5. This constraint is very general and applies to all dark matter candidates with a mono-energetic line emission in the keV-range.

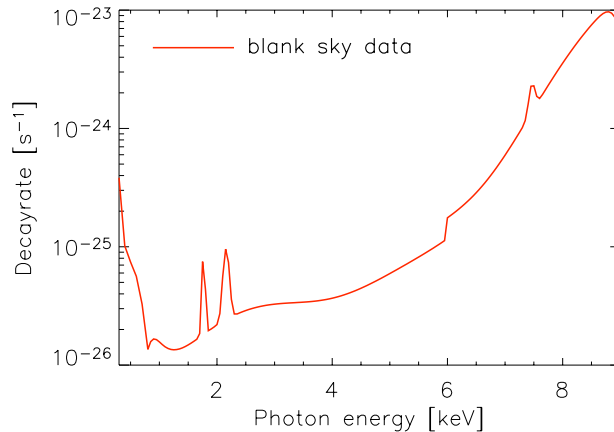


Figure 4.5: The upper limit on the decay rate as function of photon energy from the Chandra blank sky observations looking out through the Milky Way halo (the area above the line is excluded).

4.2.5 COMPARING DATA AND MODEL

In the Dodelson-Widrow production scenario, the mixing angle is given by (Eqn. 209 and Eqn. 210 in Dolgov, 2002):

$$\sin^2(2\theta) \approx 1.14 \times 10^{-7} \left(\frac{A}{6.7 \times 10^{-8}} \right) \left(\frac{g_*(T_{produced})}{15} \right)^{3/2} \left(\frac{S}{1} \right) \left(\frac{\Omega_{DM}}{0.26} \right) \left(\frac{h}{0.71} \right)^2 \left(\frac{m_s}{\text{keV}} \right)^{-2}, \quad (4.2)$$

where $g_*(T_{produced})$ is the number of relativistic degrees of freedom at the temperature at which the sterile neutrinos are produced. For neutrino masses of the order of keV, the neutrinos are produced near the QCD phase transition (Dodelson & Widrow, 1994), making the distribution somewhat non-thermal (Dolgov & Hansen, 2002). The value of g_* for such neutrinos is very conservatively considered to be between 10.75 and 20, depending on the details of the QCD phase transition. I used $g_*(T_{produced}) = 15$ as a reference value. A numerical calculation including the details of the QCD phase-transition (Abazajian, 2006) has confirmed that the choice $g_* = 15$ is in good agreement with the analytical results presented by Dolgov (2002). It should however be kept in mind that the exact details of the QCD phase transition may change the production factor by a few (Asaka et al., 2007).

In Eqn. 4.2, S is a free parameter taking into account a possible additional entropy production after the sterile neutrinos have been created. This entropy production could arise from decays of the heavier sterile neutrino mass eigenstates, leading to a dilution of the momentum distribution of the dark matter sterile neutrinos. The characteristic size of structure formation must remain the same even with the additional entropy production and we have (Asaka et al., 2006b):

$$m_s S^{1/3} \propto \text{constant}. \quad (4.3)$$

Also the temperature of the sterile neutrinos will be diluted by a factor of $S^{1/3}$. S was originally suggested to be in the range between 1 and 100 and later proposed to be between 1 and 2 (Asaka et al., 2006b; Shaposhnikov & Tkachev, 2006).

A is a numeric constant depending on which active neutrino the sterile neutrinos are assumed to mix with. It takes the values $A_{se} = 6.7 \times 10^{-8}$ for ν_s mixing with ν_e and $A_{s\mu} = 4.8 \times 10^{-8}$ for $\nu_{\mu,\tau}$. We only considered mixing with ν_e and the sterile neutrinos were assumed to account for all dark matter. h is the Hubble parameter at the present time.

The observational constraint on the decay rate can be converted to a constraint on the lifetime by combining Eqn. 4.2 with Eqn. 3.6 for the decay rate, and Eqn. 3.8 for the branching ratio:

$$\tau = \left(\frac{E}{\text{keV}} \right)^{-3} \left(\frac{g_*}{15} \right)^{-3/2} \left(\frac{\Omega_{DM}}{0.3} \right)^{-1} \left(\frac{h}{0.7} \right)^{-2} \frac{f(m_s) 6.5 \times 10^{18} \text{sec}}{AS}. \quad (4.4)$$

The resulting lower limit on the lifetime from the data and the model predictions are plotted in Fig. 4.6 for various values of S and g_* . It is seen that the blank sky data (solid red line) is at least one order of magnitude less restrictive than the simplest sterile model predictions (hatched region). Models with significant entropy production, $S \approx 30$, are excluded in the mass range $4.2 \text{ keV} < m < 7 \text{ keV}$ and $S > 100$ excludes $2 \text{ keV} < m < 16 \text{ keV}$. Similar constraints were obtained from the observations of the outskirts of the galaxy cluster Abell 383.

4.2.6 OTHER CONSTRAINTS

The sterile neutrino mass is bounded from below by the Tremaine-Gunn bound applied to dwarf spheroidals requiring $m_s > 0.5 \text{ keV}$ (Tremaine & Gunn, 1979; Lin & Faber, 1983). In the simplest Dodelson-Widrow scenario with thermally produced sterile neutrinos and $S = 1$ the lower bound can be strengthened by using Lyman α observations as described in Sec. 3.3.4. At the time

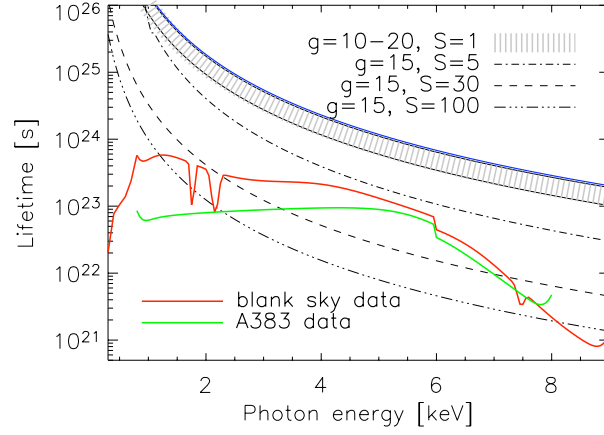


Figure 4.6: The lifetime constraints (the area below the curve is excluded) from the flux of the Chandra blank sky data (red) and the galaxy cluster Abell 383 (green). The ν MSM prediction for $S = 1$ and $g_* = 10 - 20$ (hatched) and several variations of S and g_* (black) have been overplotted.

of publishing, the constraints varied from $m_s \lesssim 2$ keV to $m_s \lesssim 14$ keV (Viel et al., 2005; Seljak et al., 2006). These constraints are weakened when allowing for $S > 1$ (Asaka et al., 2006b), since additional entropy dilutes the momentum of the sterile neutrinos.

Upper limits on the sterile neutrino mass are derived from the flux of the diffuse photon background (Dolgov & Hansen, 2002), and are of the order $m_s < 15$ keV for $S = 1$ (Mapelli & Ferrara, 2005; Boyarsky et al., 2006a). These bounds are strengthened for $S > 1$, since the sterile neutrinos decay faster. The strong claim of an upper mass limit presented in Abazajian et al. (2001b) under-estimated the flux from the Virgo galaxy cluster by 2 orders of magnitude, and is unreliable (Boyarsky et al., 2006b).

Comparing these existing bounds with our findings, we conclude that a broad band in the $m_s - S$ parameter space is still open as shown in Fig. 4.7. Depending on the analysis, the parameter space excluded by Lyman α varies between the hatched blue ($m_s < 2$ keV) and hatched green

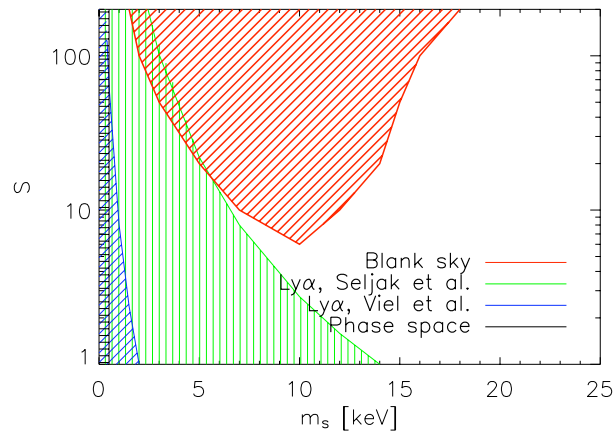


Figure 4.7: The $m_s - S$ parameter space with constraints from the Chandra blank sky data (this work, red), conservative Lyman α observations (blue, Viel et al., 2005), more ambitious Lyman α analysis (green, Seljak et al., 2006), Tremaine-Gunn bound $m_s > 0.5$ keV (black).

($m_s < 14$ keV) regions basically excluding masses smaller than $m_s \lesssim 5$ keV regardless of entropy production, but allowing for higher masses ($m_s \gtrsim 10$ keV) and low entropy production ($S \lesssim 10$).

4.2.7 CONCLUSIONS ON MILKY WAY HALO CONSTRAINTS

We used *Chandra* blank sky observations, i. e. looking out through the Milky Way halo, to search for a possible decay line from dark matter particles. No obvious decay line was identified.

The blank sky 0.3 – 9 keV X-ray flux was used to constrain the parameter space of sterile neutrinos. Our analysis is conservative and assumes that the entire blank sky signal at a given energy is arising from a decaying neutrino. The results obtained here may be improved significantly by looking for decay lines above the expected blank sky emission.

We found that the entropy production must be limited to $S < 100$ for the mass range 2 keV $< m_s < 16$ keV, and even $S < 10$ for masses near $m_s = 10$ keV in the Dodelson-Widrow production scenario. Combining with the Lyman α constraints excludes masses below $m_s \lesssim 5$ keV regardless of entropy production leaving only larger masses. The Lyman α constraints are weakened by the entropy production opening a small window with $m_s \approx 5 - 15$ keV with the requirement of an entropy production of $S \approx 1 - 10$.

It has later been shown by Boyarsky et al. (2009a) that the Dodelson-Widrow scenario can be ruled out when combining all existing X-ray and soft γ -ray constraints.

4.3 THE DARK MATTER BLOB OF ABELL 520

This section is based on the results published in Riemer-Sørensen et al. (2007a) where the "dark matter blob" in the galaxy cluster Abell 520 was investigated. Abell 520 (Fig. 4.8) is a merging cluster (Markevitch et al., 2005) similar to the Bullet Cluster (Clowe et al., 2006) with regions of high dark matter density and low X-ray noise from baryonic emission. The very low X-ray noise environment provide decay rate limits up to an order of magnitude better than the Milky Way despite the much larger distance. For the chosen cosmology³, the luminosity distance to Abell 520 is $D_L = 980$ Mpc ($z = 0.203$, Ebeling et al., 1998).

4.3.1 THE SPECTRUM OF ABELL 520

An ACIS-S3 0.3 – 9.0 keV spectrum was extracted from the 67 ksec *Chandra* observation with id 4215 for a region centered at the dark matter blob and with a radius of $r = 0.85$ arcmin = 190 kpc (the red circle in Fig. 4.8). Before extracting the spectrum, I performed a standard processing of the data with CIAO 3.3 (Fruscione et al., 2006) and manually removed the two point sources within the region.

As seen by the red circles in Fig. 4.9 the dark matter blob is corresponding to a small group of very X-ray faint galaxies (the analysed region is slightly shifted from the region with highest density because it was defined from Fig. 4.8 and not from Fig. 4.9).

The spectrum was fitted by a non-physical model consisting of a power law and six Gaussians designed to fit the spectrum with a reduced χ^2 of 1.2 (for 80 d. o. f.). The extracted spectrum and the fitted model are shown in Fig. 4.10.

4.3.2 FLUX DETERMINATION

For the flux determination I used a simple and conservative approach called the "slice method". The energy range of the spectrum is divided into bins of width equal to the instrumental energy

³ Λ CDM parameter values: $H_0 = 71$ km sec⁻¹ Mpc⁻¹, $\Omega_M = 0.26$, and $\Omega_\Lambda = 0.74$

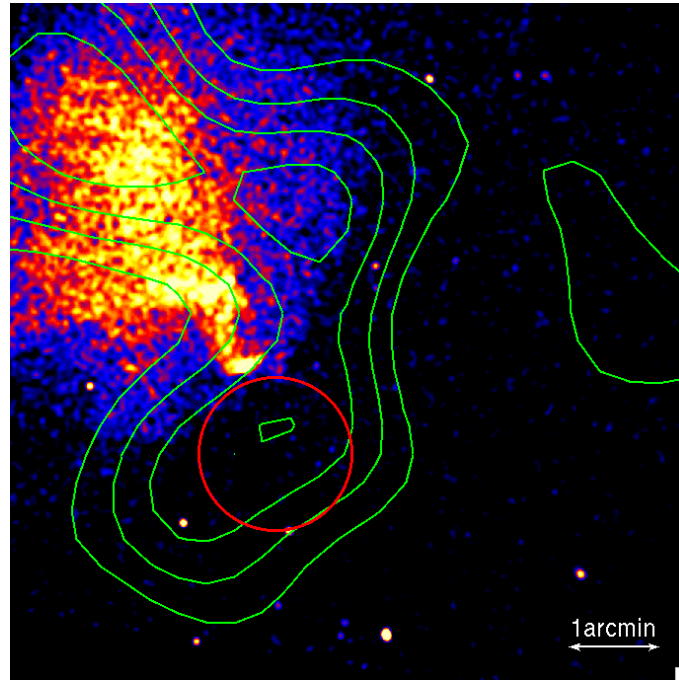


Figure 4.8: Abell 520 observed with Chandra (0.3 – 10.0 keV, orange and blue colours) with the gravitational potential from weak lensing overlaid (green contours). The dark matter blob in the red circle has very low X-ray emission from baryons.

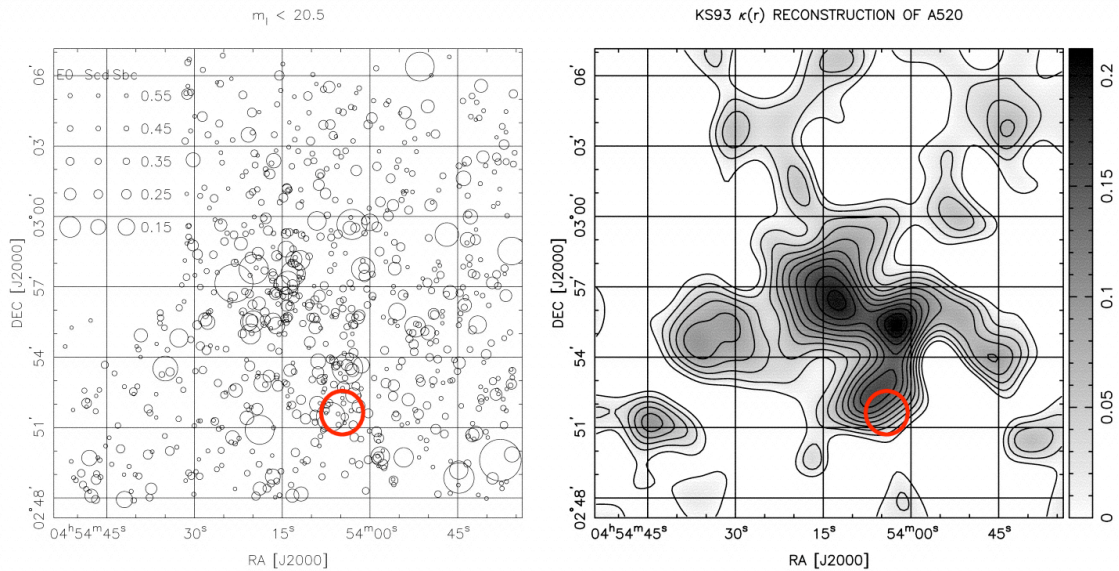


Figure 4.9: (Left) The galaxies of Abell 520. The size of the circle reflects the luminosity of the galaxy. The red circle is the region of the dark matter blob. (Right) The surface mass density of Abell 520 (Dahle et al., 2002).

resolution (FWHM), and all of the X-ray flux in a particular bin is determined from a model fitted to the spectrum. The slice method is very robust, as the physics behind the fitted model is irrelevant. Furthermore, the method does not require any assumptions about the X-ray background, but regards all received flux as an upper limit for the flux from decaying dark matter, despite the fact that unresolved sources, the intra cluster medium, the Milky Way halo, etc. all contributes

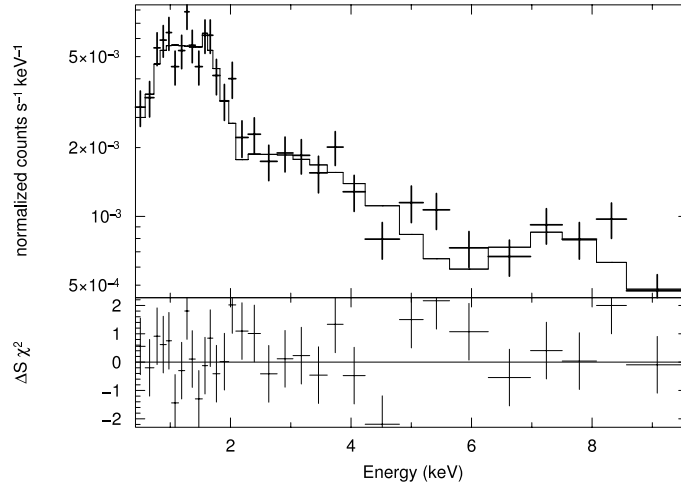


Figure 4.10: The observed spectrum of Abell 520 with the fitted model (upper panel) and the fit residuals (lower panels).

to the total emission. The slice method takes into account that an emission line from decaying dark matter could "hide" under a line feature in the spectrum (see Sec. 4.1.1). The flux obtained with the slice method is almost identical to the flux obtained with the "Gaussian method" used in Riemer-Sørensen et al. (2006, Sec. 4.1.1). Other methods for constraining the flux can give stronger, but less conservative or robust, results (e. g Watson et al., 2006; Boyarsky et al., 2006b).

The slice width is given by the energy resolution of ACIS-S3 (CXO Proposers' Observatory Guide, 2008, $E_{FWHM} = 2.35\sigma$ for a Gaussian):

$$\sigma_{S3} = 0.005E_{\gamma} + 0.05 \text{ keV}. \quad (4.5)$$

4.3.3 BACKGROUND SUBTRACTION

For Abell 520 I attempted to subtract the background as spectra from nearby regions with identical area but away from the dark matter blob. The resulting spectrum is shown in Fig. 4.11. The

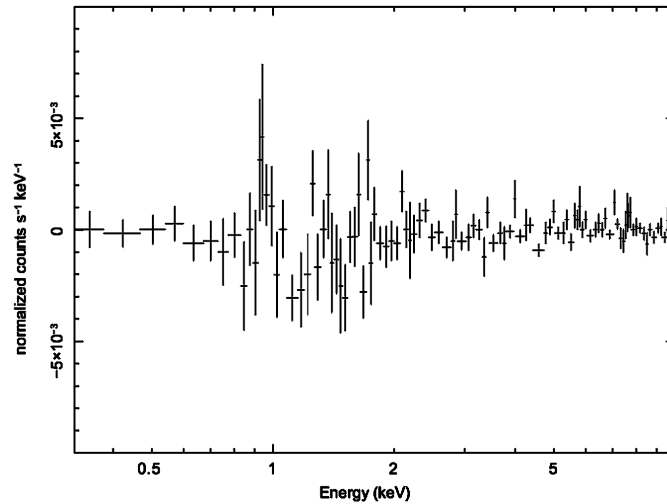


Figure 4.11: The Chandra spectrum of the Abell 520 dark matter blob subtracted the spectrum of a region with similar gas density as the dark matter blob but much lower dark matter mass.

line feature just below 1 keV appears in the blob spectrum, but not in the background from any of the nearby and less dark matter dense regions. The signal is not very significant and a comparison to the corresponding *XMM* spectrum revealed no signal at all. If the line was due to dark matter, it would be expected around 1.1 keV in the blank sky spectrum shown in Fig. 4.2, which is not the case. Furthermore, most of the cluster gas emission takes place below 2 keV with the amount of line emission strongly depending on the gas temperature (Arnaud et al., 2005), which might vary from region to region in the colliding cluster.

4.3.4 MASS OF THE BLOB

Håkon Dahle derived the mass of the dark matter blob in Abell 520 from weak gravitational lensing to be $M_{fov}^{blob} = 4.78 \pm 1.5 \times 10^{13} h^{-1} M_{\odot}$. This value is based on measuring the overdensity in the region in the red circle (Fig. 4.8) with respect to the mean density in a surrounding annulus with inner and outer radius of 0.85 arcmin (168 kpc) and 4 arcmin (792 kpc), respectively. Hence, the mass value can be regarded as a conservative lower limit on the mass contained within the blob region. A mass map generated using the method of (Kaiser et al., 1995) shows a 4σ detection of mass in this region, compared to noise maps based on randomised shear values. A detailed description of the data and methodology of the weak lensing analysis is given in Dahle et al. (2002). Two independent weak lensing analyses of Abell 520 (Mahdavi et al., 2007a; Okabe & Umetsu, 2008) confirms the existence of the blob, centered at slightly different positions. The blob region used here, contains a significant amount of dark matter according to all lensing analyses and was chosen to minimise the baryonic emission from the cluster gas.

The dominating baryonic component in clusters of galaxies is the hot X-ray emitting intra cluster gas. However the generally observed gas mass fraction is only $f_{gas} \approx 0.11$ (Allen et al., 2002). In merging galaxy cluster systems, the gas has been displaced from the blob regions, so the gas mass is negligible and the mass of the dark matter was taken to be the total mass of the blob as determined from gravitational lensing.

4.3.5 DECAY RATE

Fig. 4.12 shows the very general upper limit on the decay rate (Eqn. 3.10) of any dark matter candidate with a two-body radiative decay as obtained from the total received flux from the Abell 520

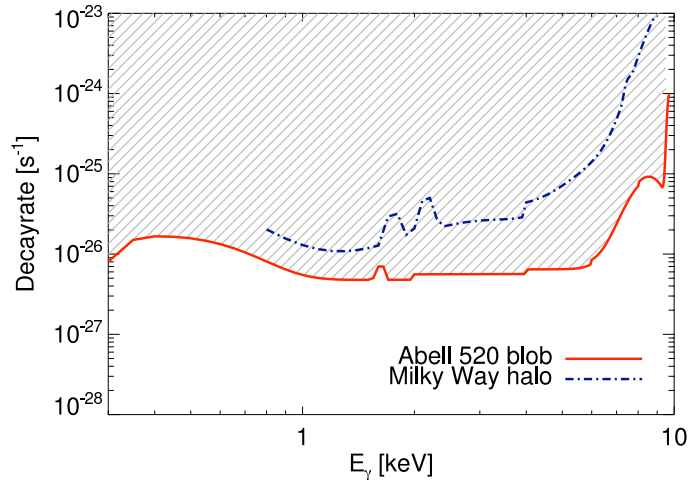


Figure 4.12: The upper limit on the radiative two-body decay rate obtained from the dark matter blob of Abell 520 (solid) together with the Milky Way halo constraint (dot-dashed Riemer-Sørensen et al., 2006).

dark matter blob. It is seen that the obtained constraints are an order of magnitude stronger than the ones obtained from observations of the Milky Way halo alone (Riemer-Sørensen et al., 2006; Boyarsky et al., 2007b). The apparent energy dependence arise because the determined flux is dominated by the background, which varies as a function of energy.

The Milky Way dark matter halo will always be included in the observation, but its M_{fov}/D_L^2 is negligible compared to the same ratio for the dark matter blob.

4.3.6 CONSTRAINING MASS AND MIXING ANGLE

The observational constraints in the $\sin^2(2\theta) - m_s$ parameter space are shown in Fig. 4.13 for the dark matter blob of Abell 520 (red) together with the Tremaine-Gunn limit (hatched), and earlier X-ray constraints (grey). The constraints derived here are very robust as they have been derived from the total amount of received X-ray flux without subtraction of any background contributions. The observed region was chosen for its favourable low baryonic background.

In the simplest Dodelson-Widrow production scenario of the sterile neutrinos (Dodelson & Widrow, 1994), lower bounds on the mass can be obtained from studies of the Lyman α forest (Seljak et al., 2006; Viel et al., 2005, 2006), which combined with the X-ray constraints rule out the full parameter space. However there are other production scenarios, for example via resonance or inflation (Shaposhnikov & Tkachev, 2006), for which the Lyman α results cannot be applied.

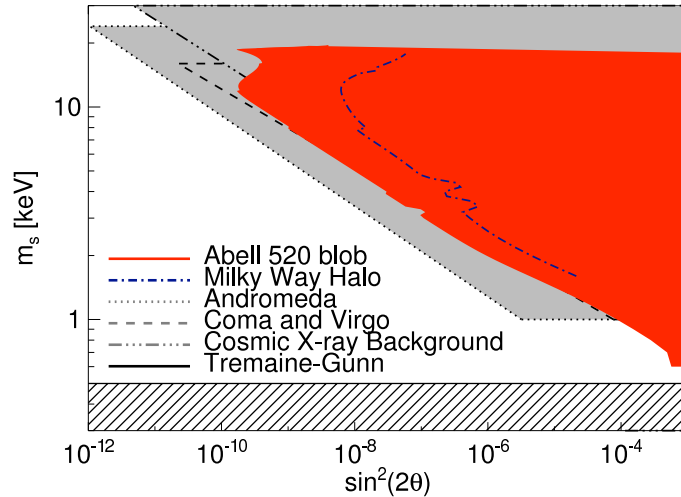


Figure 4.13: The observational constraints from the dark matter blob of Abell 520 (red) together with the Tremaine-Gunn limit (hatched, Tremaine & Gunn, 1979), and earlier X-ray constraints (grey, Boyarsky et al., 2006c,b,a, 2007b, 2008c; Riemer-Sørensen et al., 2006; Watson et al., 2006).

4.3.7 CONCLUSIONS FROM ABELL 520

A very general constraint on the decay rate for all dark matter particle candidates with a two-body radiative decay in the X-ray range was derived. Analysing a spectrum obtained through direct imaging of the almost pure dark matter blob in the galaxy cluster Abell 520, an upper limit of $10^{-26} \text{ sec}^{-1}$ was derived for the decay rate into mono-energetic photons. The mass and mixing angle can be constrained in the specific case of sterile neutrinos, leaving a low mass ($m_s \lesssim 10 \text{ keV}$) and low mixing angle ($\sin^2(2\theta) \lesssim 10^{-6}$) window open. Such constraints can be improved significantly by improving the signal to noise ratio (optimisation of field of view).

Based on the constraints obtained from X-ray observations alone, the low mass ($m_s \lesssim 10 \text{ keV}$) and low mixing angle ($\sin^2(2\theta) \lesssim 10^{-6}$) sterile neutrino is still a viable dark matter candidate.

4.4 WHY IT IS DIFFICULT TO USE GRATINGS

The better the spectral resolution becomes, the better the chances of finding a specific emission line in the spectrum. The spectral resolution of *Chandra* can be significantly improved by employing a grating as described in Sec. 4.4. Unfortunately this method is only optimal when applied to bright point sources (or nearly point sources) as the spatial resolution of the arriving photons is lost, when they are deflected by the grating. For extended sources, there is a degeneration between the deflection angle and photon energy, leading to a "smearing" which decreases the instrumental resolution. This sections presents the results of Riemer-Sørensen et al. (2007a) where we calculated the obtainable resolution for galaxy clusters using Abell 1835 as a generic example.

4.4.1 THE GENERIC EXAMPLE CLUSTER ABELL 1835

There are four important criteria to consider when selecting a cluster for a dark matter line search: i) It has to be observed and the data has to be accessible. ii) The distance to the cluster has preferably to be so that all of the cluster is contained within one *Chandra* pointing, but not so far away that we receive too few photons to do statistical model fitting. For a cluster with virial radius around $R \approx 1000$ kpc, the optimal distance is $z \approx 0.15 - 0.25$. iii) The cluster should be heavy in order to increase the mass within the field of view. iv) The cluster gas should be relatively hot since the number of gas emission lines decreases with temperature, and consequently choosing a relatively hot (10 keV) cluster reduces the number of spectral lines originating in standard physics processes (Sarazin, 1988). From these criteria I chose Abell 1835 as a generic example of a cluster to illustrate the properties of a grating observation. It has been observed for 124 ksec with *Chandra* HETG in the observation with id 511. The luminosity distance is $D_L = 1225$ Mpc ($z = 0.252$) for the adopted cosmology⁴ (Schmidt et al., 2001). Its mass distribution is well described by a standard NFW-profile (Eqn. 1.4) with the best-fit parameters $r_s = 0.8^{+1.59}_{-0.38}$ Mpc ≈ 4.2 arcmin and $\rho_0 = 5.2 \pm 2.5 \times 10^{14} M_\odot \text{Mpc}^{-3}$, leading to a total mass within the scale radius of $M_s = 6.5 \times 10^{14} M_\odot$ (Voigt & Fabian, 2006).

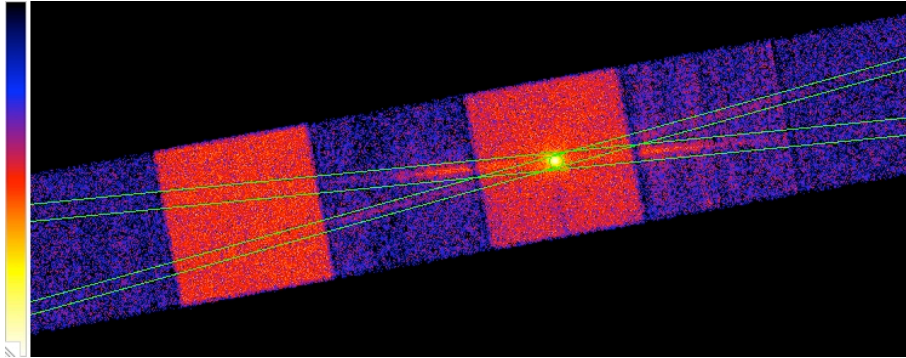


Figure 4.14: Abell 1835 as observed with the *Chandra* HETG instrument. The green lines marks the deflected spectrum and the circle is the zero order region.

4.4.2 GRATING OBSERVATIONS

When the incoming photons are deflected in a grating, the information of their spatial origin is lost. This makes it impossible to optimise the ratio of expected dark matter signal to noise (from X-ray emitting baryons) in the observational field of view as otherwise implemented (Boyarsky et al., 2006b,c; Riemer-Sørensen et al., 2006; Watson et al., 2006). The resolution of a grating

⁴ Λ CDM parameter values: $H_0 = 71 \text{ km sec}^{-1} \text{ Mpc}^{-1}$, $\Omega_M = 0.26$, and $\Omega_\Lambda = 0.74$

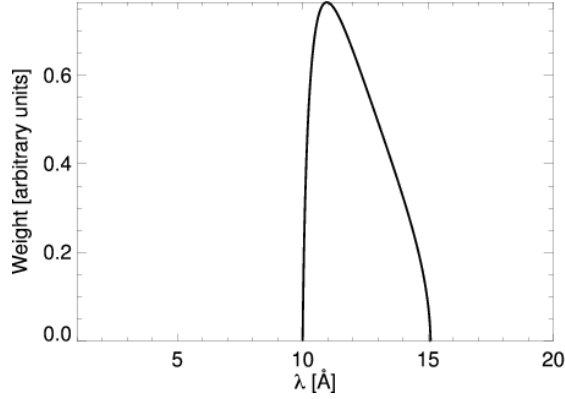


Figure 4.15: Example of the weighting given by Eqn. 4.7 for a NFW-profile for Abell 1835.

spectrometer decreases proportionally to the angular extension of the source.

Any spatially extended source can be thought of as a collection of point sources. The deflection angle, χ , of photons from a mono-energetic point source with incoming angle θ , is given by "The Grating Equation" (Eqn. 6.10 in Hecht, 2001):

$$n\lambda = d(\sin(\theta) - \sin(\chi)), \quad (4.6)$$

where n is the deflection order, and d the grating distance. A range of combinations of values for λ and θ leads to the same deflection angle. Let χ_0 be a given (fixed) deflection angle. If χ_0 corresponds to an on-axis source, only one set of values for $(\lambda, \theta) = (\lambda_0, 0)$ is valid and χ_0 is given as $n\lambda_0 = -d \sin \chi_0$. The possible values of (λ, θ) corresponding to this deflection angle is given by:

$$\lambda = \frac{d}{n} \sin \theta + \lambda_0 n = \frac{R}{D_L} (1+z)^2 \frac{d}{n} + \lambda_0 n, \quad (4.7)$$

where the last equality is for a mono-energetic point source with an off-axis projected distance, R . For a mono-energetic source with a given mass distribution, the flux originating at each θ should be weighted according to the mass at the given projected radius. An example of the weighting is shown in Fig. 4.15 for Abell 1835. The resolution is given by the full width half maximum of the resulting distribution.

4.4.3 CONCLUSIONS ON GRATINGS

It turns out that the obtained energy dependent resolution of $\sigma_{HEG} \approx 0.15$ keV for a photon energy of 1 keV is of the same order of magnitude as the imaging spectral resolution (Eqn. 4.5) for realistic dark matter structures ($\sigma_{S3} \approx 0.05$ keV at 1 keV). Consequently X-ray gratings are not particularly suited for observations of extended dark matter structures such as galaxy clusters as the resolution decreases with the source extension.

4.5 FIRST CONSTRAINTS FROM THE DRACO DWARF GALAXY

It has been demonstrated that the optimal place to search for the decay line of sterile neutrinos is from the dwarf galaxies of our Milky Way such as Ursa Minor, Draco etc. (Boyersky et al., 2006c, 2007b). These dwarfs are nearby, they are X-ray quiet, have a high central dark matter density, and at the same time, we have fairly accurate mass models from optical observations (Wilkinson et al., 2004; Gilmore et al., 2007; Strigari et al., 2007, 2008). Being very X-ray quiet, the only problem is lack of data, because who wants to observe something quiet?

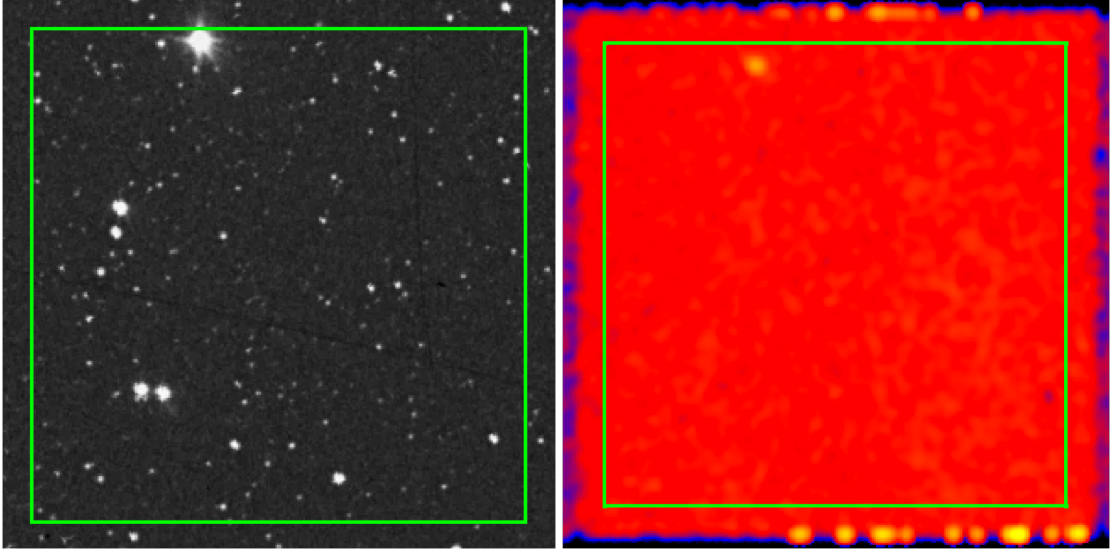


Figure 4.16: (Left) Optical image of the Draco dwarf galaxy with the observed region of $(7.6 \text{ arcmin})^2 \approx (0.18 \text{ kpc})^2$ marked by the green box (SkyView, 2009). (Right) Same but in X-rays observed with Chandra .

In Riemer-Sørensen & Hansen (2009) I analysed recent public available *Chandra* X-ray data of the dwarf galaxy Draco. The Draco and blank sky spectra are almost identical which confirms that i) Dwarf spheroidals are ideal for studying dark matter X-ray emission since the baryonic noise is impressively low, ii) there is very little room for line emission. The absence of any line signal was used to derive constraints in the mass-mixing angle parameter space of the sterile neutrinos. I compared the standard flux derivation method to a very conservative rebinning approach. The resulting constraints are strongly dependent on the chosen method⁵.

4.5.1 X-RAY ANALYSIS

There exist two public *Chandra* observations of Draco with observation ids 9568 (24.8 ksec) and 9776 (12.2 ksec) in the NASA HEASARC archive (Fig. 4.16 NASA, 2008). Before extracting spectra, I reprocessed the data with the newest versions of CIAO (4.1) and CALDB (4.1) following standard procedures (Fruscione et al., 2006). A total of 12 uniformly distributed point sources were removed and the light curve cleaned, reducing the total exposures to 20.3 ksec (9568) and 12.0 ksec (9776). The central part of Draco is situated on the S3 chip. The spectra were extracted from a square region of $(7.6 \text{ arcmin})^2 \approx (0.18 \text{ kpc})^2$, avoiding the edges of the chip. The response matrices were generated and the spectra and response matrices of the two observations were combined using *ftools* (Irby, B., 2008b) which was justified by the very similar count rates in the two otherwise identical observations. For background subtraction I extracted the spectrum of the identical region of S3 from the blank sky data provided with CIAO.

The Draco and blank sky spectra are shown in Fig. 4.17, where it is clearly seen that they are almost identical, with very little room for a dark matter signal.

The normalisation of the blank sky spectrum was determined from the average count rate in the 4 – 6 keV interval for both blank sky and observation. This interval was chosen because the two spectra are very flat and well calibrated here. Additionally, no thermal gas emission is expected at these energies, as Draco is a small and cold structure. The uncertainty of the average count rate is less than 0.5%. Normalising at higher energies gives slightly different background

⁵ Λ CDM parameter values: $H_0 = 71 \text{ km sec}^{-1} \text{ Mpc}^{-1}$, $\Omega_M = 0.26$, and $\Omega_\Lambda = 0.74$

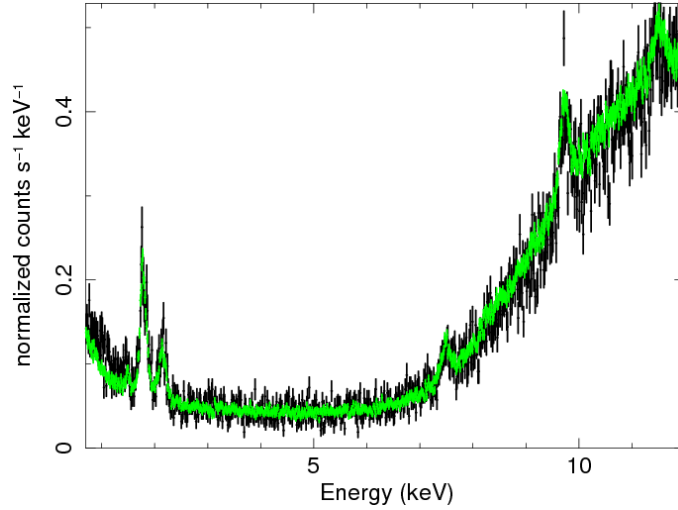


Figure 4.17: Spectrum of the central $(7.6 \text{ arcmin})^2$ of Draco (black) and the corresponding normalised blank sky spectrum (green).

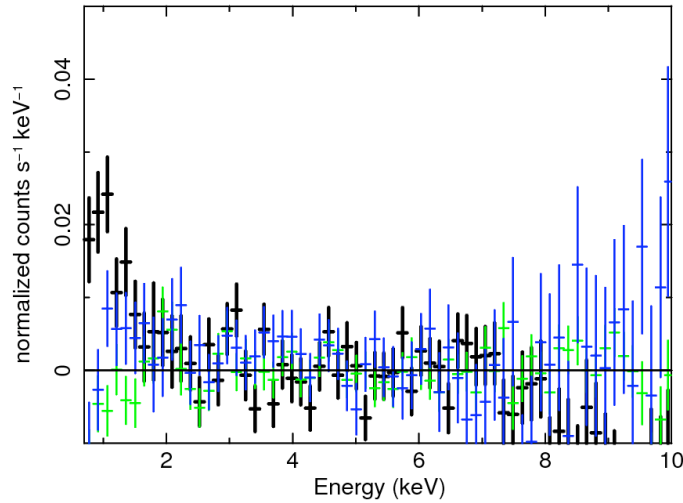


Figure 4.18: The background subtracted spectra of the S3 (center of Draco, fat black), S2 (8.6 arcmin from center, green), and S3 (17.3 arcmin from center blue) chips rebinned for visualisation. In the case of any observable signal from dark matter, there will be a radial dependence, like the one around 1 keV, where the signal disappears far from the center.

levels e.g. 10 – 12 keV gives a 3.5% lower level, and 12 – 14 keV (which is usually used for galaxy cluster observations) gives a 0.5% higher level. However, both intervals have higher uncertainties on the normalisation due to the large scatter.

The background-subtracted Draco spectrum is shown in Fig. 4.18 (black). Apart from a small excess around 1 keV, the spectrum is effectively zero and hence the baryonic noise level is very low and there is virtually no room for a dark matter decay line.

After the background subtraction, the only possible signal is at low energies ($\approx 0.7 - 1.5 \text{ keV}$). The best fitting Gaussian has a width of $\geq 0.5 \text{ keV}$, which is an order of magnitude larger than the width of the instrumental resolution at 1 keV. To check for any radial dependence in the signal, I extracted spectra from similar regions of the S2 and S1 chips centered $\approx 8.6 \text{ arcmin}$ and $\approx 17.3 \text{ arcmin}$ from the center of Draco. The three spectra are compared in Fig. 4.18. The low energy "bump" around 1 keV is not clearly present in the outer radial bins. It is tempting

to believe that this is a signal proportional to the mass within the field of view. Nonetheless, the excess is not very significant ($\lesssim 1\sigma$) and is too wide to be a monochromatic emission line. Most astrophysical backgrounds such as stellar and thermal radiation will also follow the mass distribution of Draco.

After publishing the paper I revisited the data and found the low energy excess emission to originate from the source in the upper part of the field of view (Fig. 4.16), which from the optical observation seems to be a foreground star.

The upper limit on the flux was derived in the 0.7 – 10 keV interval using the spectral fitting package Xspec (version 12.4, Arnaud et al., 2009) following different approaches. The flux derivations are based on the dark matter in Draco being practically at rest ($v/c \approx 10^{-4}$, Gilmore et al., 2007) so the line broadening due to internal motion is negligible compared to the instrumental resolution. The instrumental resolution is given by (CXO Proposers' Observatory Guide, 2008, $E_{FWHM} = 2.35\sigma$ for a Gaussian):

$$E_{FWHM} = 0.012E_\gamma + 0.12 \text{ keV} . \quad (4.8)$$

One employed approach was to rebin the data with a binwidth corresponding to the instrumental resolution. At a given energy, E_γ , all bins within the interval $[E_\gamma - E_{FWHM}/2 : E_\gamma + E_{FWHM}/2]$ were rebinned to give a single bin value and uncertainty (fat data point in Fig. 4.19). The possible line emission was defined as a Gaussian with the width given by the resolution and maximum at the 3σ upper limit of the rebinned data. The upper limit on the flux was determined from the Gaussian over the same interval as the data were rebinned.

Another approach was to model the background instead of subtracting it (same method as discussed in Boyarsky et al., 2006c). The background was fitted with a continuum consisting of an exponential and 10 Gaussians. The fit gave a reduced χ^2 of 1.3 (for 637 d. o. f.). The line emission was added to the model as a Gaussian with the width given by the instrumental resolution as illustrated in Fig. 4.20. The total model was fitted to the data with the normalisation of the Gaussian as the only free parameter. The flux was determined exclusively from the Gaussian with the normalisation set to the 3σ upper limit from the fit.

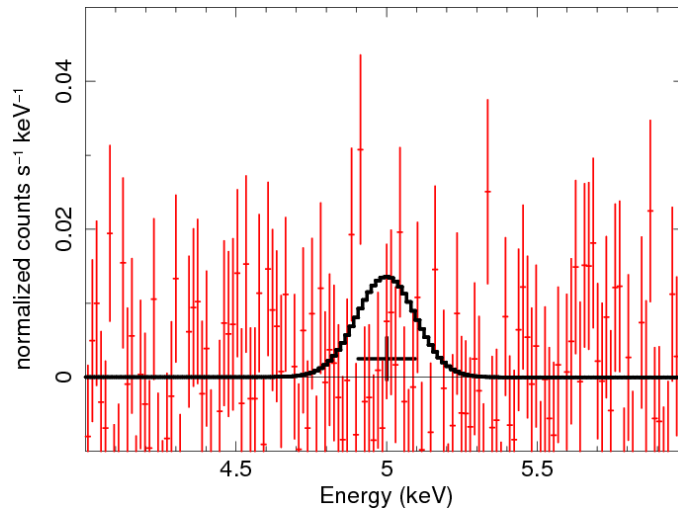


Figure 4.19: The rebinning approach illustrated for $E_\gamma = 5$ keV. All data within the interval $[E_\gamma - E_{FWHM}/2 : E_\gamma + E_{FWHM}/2]$ was rebinned to one bin (central data point). The width of the Gaussian is given by the resolution and the maximum by the 3σ upper limit of the rebinned data.

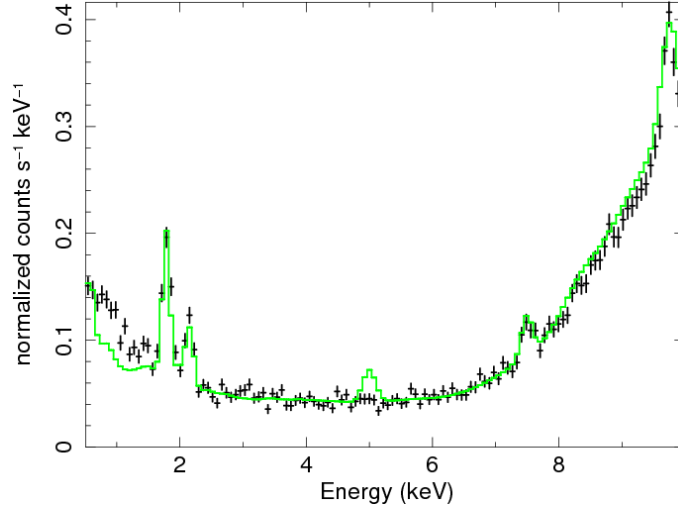


Figure 4.20: The Draco spectrum (black) and the background model (green line) including the potential line at $E_\gamma = 5$ keV. For visualisation, the line normalisation has been increased by a factor of 10.

4.5.2 OBSERVED MASS

The dark matter mass within the field of view was determined from the density profile derived from photometric and kinematic data by Gilmore et al. (2007). The density profile in the 0.1 – 0.5 kpc range is well described by $\rho(r) = \rho_0(1 + (r/r_0)^{1.5})^{-2.25}$ where $\rho_0 = 0.65 \times 10^9 M_\odot \text{ kpc}^{-3}$ and $r_0 = 0.28$ kpc. I extrapolated this profile to the observed range of 0 – 0.18 kpc and integrated along the line of sight to determine the mass within the field of view. The total dark matter mass of Draco within 0.5 kpc is larger than $6 \times 10^7 M_\odot$ (Gilmore et al., 2007; Strigari et al., 2008) of which approximately $6.7 \times 10^6 M_\odot$ lies within the observed square. The statistical uncertainty on the mass is very small, but the systematics are very hard to determine (Gilmore et al., 2007; Boyarsky et al., 2007b).

4.5.3 RESULTS

Fig. 4.21 shows the obtained upper limits on line emission flux as a function of photon energy (coloured areas are excluded). These constraints are very general and apply to all dark matter candidates with a monochromatic line emission. The vertical lines in the rebinned approach constraints are single energies, where the upper limit on the flux becomes exactly zero for a 3σ upper limit on the flux (using this approach with the chosen background normalisation). If we require e. g. 5σ , they disappear.

The fluxes are converted to constraints in the $m_s - \sin^2(2\theta)$ parameter space for sterile neutrinos of the Majorana type, assuming the sterile neutrinos to account for all of the dark matter in Draco (Riemer-Sørensen et al., 2006; Boyarsky et al., 2006c):

$$\sin^2(2\theta) \leq 1 \times 10^{18} \left(\frac{F_{det}}{\text{ergcm}^{-2}\text{s}^{-1}} \right) \left(\frac{m_s}{\text{keV}} \right)^{-5} \left[\frac{(M_{fov}/M_\odot)}{(D_L/\text{Mpc})^2} \right]^{-1}. \quad (4.9)$$

The distance to Draco is 80 kpc (Gilmore et al., 2007). The resulting conservative constraints are shown in Fig. 4.22 (red and black hatched) compared to earlier constraints from galaxy clusters, galaxies, and the Milky Way halo (blue, Boyarsky et al., 2009d, and references therein, see Sec. 3.4 for explanations). The overlap with earlier constraints is an excellent confirmation of the excluded parameter space, since the Draco constraints are complementary and independent of earlier constraints. Even with the relatively short exposure, the constraints are good due to the

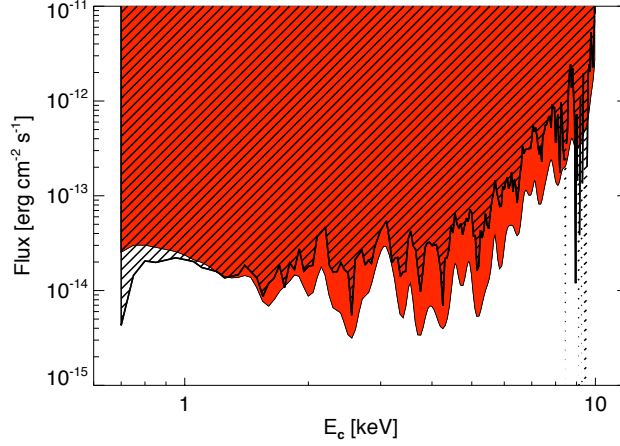


Figure 4.21: The obtained upper limits on the line emission flux. The modelling Gaussian approach (solid red) gives stronger constraints than the conservative rebinning approach (black hatches).

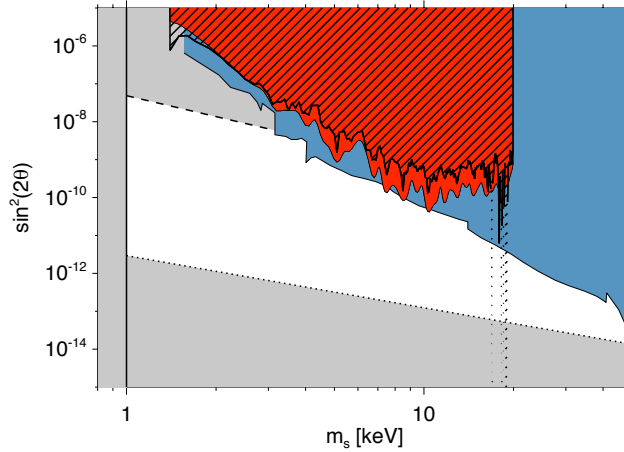


Figure 4.22: The obtained constraints in the $m_s - \sin^2(2\theta)$ parameter space for sterile neutrinos of the Majorana type. The modelling Gaussian approach (solid red) gives stronger constraints than the conservative rebinning approach (black hatched). Earlier constraints (taken from Boyarsky et al., 2009d, and references therein): Phase space considerations (grey below 1 keV), nucleosynthesis (grey region below dotted line), oscillatory production giving $\Omega_s > \Omega_{DM}$ (grey region above dashed line), earlier observational constraints (blue).

almost perfect similarity of the spectra of Draco and the background. The difference between the Gaussian modelling (red) and the rebinning (black hatched) approaches is clearly visible, with the Gaussian modelling method providing stronger constraints at most energies than the more conservative rebinning method.

4.5.4 FUTURE OBSERVATIONS?

The limiting factor of the constraints is the uncertainties in the observations and blank sky, which can be improved by increasing the exposure time. The statistics improve with the squareroot of the exposure time so a 100 ksec observation improves the constraints by a factor of two. In order to exclude the entire currently allowed region, the needed exposure time for *Chandra* or similar instruments becomes unreasonably high and a different instrumental approach is needed

(Boyarsky et al., 2007a).

X-ray observations of dwarf galaxies have also been shown to provide very good constraints on annihilating thermal relic dark matter with GeV – TeV-masses (Regis & Ullio, 2008; Jeltema & Profumo, 2008). The annihilations produce electron-positron pairs with energies as high as GeV, which during their propagation produce secondary emission due to various mechanisms (synchrotron radiation in magnetic fields, inverse Compton scattering of the CMB, and bremsstrahlung). The very low baryonic emission from the dark matter dominated dwarf galaxies also makes them ideal for constraining the secondary emission from annihilating dark matter.

4.5.5 SUMMARY

I analysed 32 ksec *Chandra* X-ray observation of the Milky Way dwarf galaxy Draco and searched for line emission from decaying dark matter particles. The Draco and blank sky background spectra have a nearly identical shape. This confirms dwarfs as ideal for studying dark matter emission since the baryonic contamination is close to zero. No obvious line signal was found, which lead to conservative constraints in the $m_s - \sin^2(2\theta)$ parameter space for sterile neutrinos. Longer exposures are needed to reduce the statistical uncertainty and improve the constraints.

4.6 POSSIBLE IMPROVEMENTS ON LINE CONSTRAINTS

Even though the constraints presented in Sec. 4.2 to Sec. 4.5 represent state of the art, they can be further improved. Previously, the focus has mainly been on selecting the object carefully and increase the statistics by prolonging the exposures. Also a range of different methods to determine what is the maximum line flux allowed by the data has been considered. Even though longer exposure times do increase the statistics, the limits for conventional constraints with the current telescopes have been reached.

One option for improving the statistical uncertainties significantly is to stack the residuals of all available background subtracted spectra of dark matter dominated objects (with appropriate redshifting). This will correspond to increasing observation time, but the sum of useful observations is much larger than any observation that will ever be granted to a single object. The challenge is how to unfold the instrumental response so the spectra can be properly redshifted before the stacking.

I would also like to investigate a completely different statistical approach using time-series analysis. It is a statistical tool well known from other branches of science, but not often applied to astronomical spectra. In principle it should allow to distinguish between pure noise and "emission line-like" noise, and determine the statistical evidence for a non-detection of line emission versus pure noise. Most of the already developed time-series analysis tools are geared to work with linear or oscillating trends, however the underlying trend in e. g. hot plasma emission from galaxy clusters is much more complicated, which provides a challenge. A similar approach is to use wavelet analysis to create a power spectrum of the "background subtracted non-signal X-ray spectra", where systematic line tendencies would show up at a statistical level.

A combination of stacked spectra and a redesigned statistical analysis has the potential to exclude all of the currently allowed parameter space without having to wait for new instruments.

5

SOLAR AXIONS AS DARK MATTER

This chapter is based on Riemer-Sørensen et al. (2007b), where I analysed X-ray observations of merging galaxy clusters (Bullet Cluster and Abell 520) to constrain radiatively decaying dark matter inspired by a specific type of Kaluza-Klein (KK) axions, invoked as a possible explanation for the solar coronal X-ray emission. These particles can be produced inside stars and remain confined by the gravitational potential of clusters. In contrast to the sterile neutrinos, which have a predicted mono-energetic line emission, the considered KK axions have towers of eigenstates decaying to a (quasi-)continuous spectrum. From the X-ray observations I derived the first cosmological¹ constraint on the lifetime for this kind of particles to be $\tau \gtrsim 10^{23}$ sec.

5.1 AXIONS

5.1.1 PECCEI-QUINN AXIONS

Axions were originally proposed by Peccei & Quinn (1977) to resolve the strong CP-problem in QCD. The non-trivial vacuum structure of QCD allows for a violation of the combination of charge conjugation and parity in strong interactions manifesting itself in e. g. a dipole moment of the neutron. Experimentally such dipole moment has not been observed, implying that the CP-violation is either extremely small or completely absent. The question of why the CP-violating term is so close to zero is a question of naturalness within QCD known as the "CP-problem". The solution proposed by Peccei & Quinn (1977) is to promote the effective CP violating term to a field by adding an additional symmetry to the Standard Model, and break this symmetry spontaneously. This results in a Nambu-Goldstone boson (Nambu, 1960; Goldstone et al., 1962) which due to non-trivial vacuum effects of QCD acquires a small mass (turning it to a pseudo-Nambu-Goldstone boson). This hypothesised particle is the axion. Presumably the axion was named after a brand of detergent since it cleaned up the problem of QCD.

By requiring a very high mass scale for the symmetry breaking, the general axion models predict very low masses ($10^{-6} - 1$ eV) and very small cross-sections for strong and weak interactions. In the presence of very strong magnetic fields, the axions can be converted into photons (and vice versa) via the Primakoff effect or photon coalescence as illustrated in Fig. 5.1 (Kim & Carosi, 2008).

The axions are looked for in a range of experiments. One class of experiments is the "light shining through a wall" experiments (e. g. ALPS, BFRS, GammeV, LIPSS, OSQAR) in which photons are sent through a strong magnetic field, where some photons are (theoretically) converted to axions. The remaining photons are blocked by an aluminium wall, letting the axions through. Behind the wall is another strong magnetic field in a completely dark cavity where the axions

¹ Λ CDM parameter values: $H_0 = 71 \text{ km sec}^{-1} \text{ Mpc}^{-1}$, $\Omega_M = 0.3$, and $\Omega_\Lambda = 0.7$

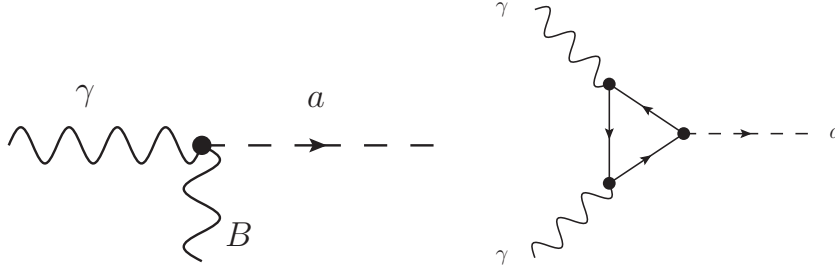


Figure 5.1: Feynman diagrams for creation of axions via the Primakoff effect and photon coalescence via a triangular loop.

are reconverted to photons. A similar class of experiments uses very strong magnetic fields to look for axions created in the strong magnetic fields in the centre of the Sun (e. g. CAST, Tokyo Axion Helioscope). A third class looks for polarisation changes of light passing through strong magnetic fields or microwave cavities indicating an interaction between photons and axions (e. g. BMV, PVLAS). So far only PVLAS have claimed a possible axion signal (Zavattini et al., 2006) but after hardware upgrade and further data taking, the claim was withdrawn (Zavattini et al., 2008).

Even though originally proposed to solve the strong CP-problem, with a bit of fine-tuning, the axion is an excellent dark matter candidate (Bergstrom, 2009; Duffy & van Bibber, 2009; Kim & Carosi, 2008). Despite dedicated experiments (e. g. ADMX) there is still an acceptable range of masses between 10^{-5} and 10^{-2} eV where the axion does not contradict any observational constraints (Bergstrom, 2009).



Figure 5.2: CAST (Cern Axion Solar Telescope) at CERN (CERN, 2009).

5.1.2 KALUZA-KLEIN AXIONS

KK particles arise in extra dimensional extensions of the Standard Model (Arkani-Hamed et al., 1998; Horvat et al., 2004). It is assumed that only gravity propagates in the higher dimension space, while the Standard Model fields are confined to our (3+1)-dimensional subspace. The higher dimensions are compactified on orbifolds of radius R . Since the axions are singlets under the Standard Model gauge group, they could also propagate in the higher-dimensional space. As a result of the compactification, the higher-dimensional axion field is decomposed into an infinite KK tower of states with the mass spacing of order $1/R$ (Dienes et al., 2000; Horvat et al., 2004). The axion mass, m_{a_i} corresponding to the lowest KK state, may decouple from the Peccei-Quinn scale and be determined by the compactification radius, $m_a = 1/(2R)$. All the KK states have the same coupling strength to matter and a source of axions will therefore emit all KK states up to the kinematic limit. The axions can decay into two photons, each with an energy of half the mass. Since all mass eigenstates are present, the photons will be emitted with energies spaced by $m_a/2 = 1/(4R)$, providing a spectrum which for reasonable values of $R \approx 1$ fm is continuous for all observational purposes.

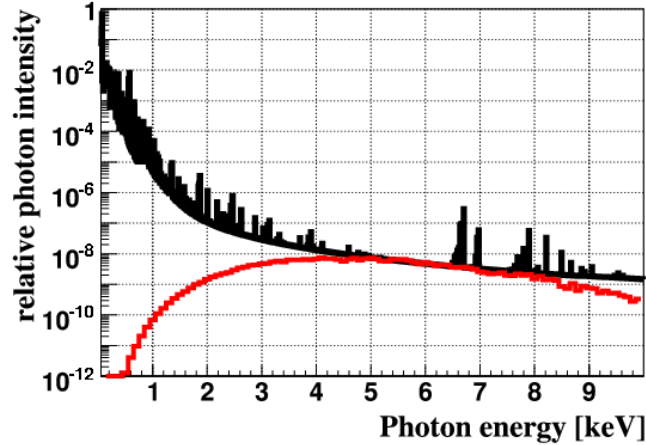


Figure 5.3: The reconstructed quiet solar X-ray spectrum from YOHKOH (black, upper curve Reale et al., 2001) and the expected flux from decaying massive axions of the KK type (red, lower curve, DiLella & Zioutas, 2003).

Recently KK particles in general have received a lot of attention as a viable explanation for the PAMELA positron excess and ATIC/PPB-BETS electron excesses (Chang et al., 2008).

5.1.3 SOLAR AXIONS

Fig. 5.3 shows an X-ray spectrum of the Sun observed with the YOHKOH satellite (McKenzie, 2002) during a period of low sun-spot activity (Reale et al., 2001). This emission is known as the "solar corona problem" because it is not explained by conventional solar models (blackbody plus corona plus sun spots) without invoking new physics. One option is to introduce massive axions of the KK type (DiLella & Zioutas, 2003; Asztalos et al., 2006). The standard axions with the remaining rest mass window in the sub-eV range live far too long to solve this problem (Hannestad et al., 2005).

The axions are produced in the core of the Sun by photon coalescence and Primakoff effect (see Fig. 5.1). Up to 16% of the solar emission can be converted to axions without changing the solar luminosity or lifetime (DiLella & Zioutas, 2003). Any source of axions will emit all KK states up to the kinematic limit, so some of the axions have enough energy to exit the Sun, but not enough to escape its gravitational potential and hence they will be trapped in orbits around the Sun. Eventually they decay spontaneously into two photons. The resulting spectrum has been calculated from the assumed production mechanism by DiLella & Zioutas (2003, red line in Fig. 5.3)². The peak energy is $E_{peak} \approx 4.5$ keV, and for $E_\gamma \geq 2.0$ keV the derived spectrum is well represented by:

$$F_{der}(E_\gamma > 2.0 \text{ keV}) = 2.2 \times 10^8 E_\gamma^{-8.1} e^{-(32.0/E_\gamma)}. \quad (5.1)$$

The shape of the predicted KK axion spectrum is tightly bound by solar physics processes. The normalisation depends on the coupling strength of the KK axions to photons and can for this purpose be treated as a free parameter.

In Riemer-Sørensen et al. (2007b) we considered the possibility that part of the dark matter in galaxy clusters is like KK axions which can be produced in normal stars and accumulated over the lifetimes of these stars (DiLella & Zioutas, 2003; Hannestad & Raffelt, 2002, 2004). Part of the

²The model considered by DiLella & Zioutas (2003) originally treated by Arkani-Hamed et al. (1998) with $m_{EW} = 100$ TeV and two extra universal dimensions ($n = 2$) has been ruled out by studies of neutron stars. However, models with $n > 3$ are not ruled out, and the final spectrum does not change much (private communication with Steen Hannestad).

so produced axions are confined by the gravitational potential of the host galaxy clusters, where they stay until they eventually decay spontaneously. Assuming the Sun to be a "typical" star in cosmos, which is a reasonable assumption, Eqn. 5.1 can be applied to KK axions produced in stars and confined by the dark matter gravitational well in galaxy clusters.

The solar axions proposed by DiLella & Zioutas (2003) as a solution to the solar corona problem, cannot alone account for all of the X-ray emission below 4 keV (difference between the red and black lines in Fig. 5.3). The remaining observed emission requires an alternative explanation, which might simply include Standard Model physics.

5.2 DATA ANALYSIS

I analysed *Chandra* X-ray observations of the two galaxy clusters Abell 520 and the Bullet Cluster (1E0657-558). Basic data on the clusters and the observations are specified in Tab. 5.2. The data were retrieved from the publicly available HEASARC database (NASA, 2008) and processed using standard data reduction methods with CIAO version 3.3 (Fruscione et al., 2006).

As seen from the X-ray images in Fig. 5.4 the clusters are merging systems (Markevitch et al., 2005; Clowe et al., 2006) where the cluster gas is displaced from the stars and the dark matter. This provides mass concentrations practically devoid of baryons ideal for dark matter studies (Clowe et al., 2006; Boyarsky et al., 2008c; Riemer-Sørensen et al., 2007a). In Fig. 5.4 the dark matter blob regions selected for the analysis are shown in white. For easy comparison to the results of Boyarsky et al. (2008c) the region in Bullet Cluster was chosen identical to their SUB region i.e. as the large circle centered on the mass peak with the smaller circle centered on the bullet boundary subtracted.

The dark matter in the Milky Way halo also contributes to the possible signal (Riemer-Sørensen et al., 2006), and such contamination must be removed. Before extracting the spectra, a background region with small mass and no significant X-ray emission, was chosen from the same observation and subtracted. This simplifies the expected signal from decaying dark matter as only one source redshift has to be considered.

The blob region spectrum shown in Fig. 5.5 is clearly different from the expected axion spectrum shown in Fig. 5.3, so there must be an additional (baryonic) contribution to the emission e. g. from gas. However, the most conservative constraint on the decaying dark matter luminosity was obtained by assuming all of the received photons to originate from decaying dark matter. The total luminosity was obtained by fitting a model consisting of a "basis" thermal emission model plus the expected axion flux to the spectrum. The basis model was a sum of a thermal

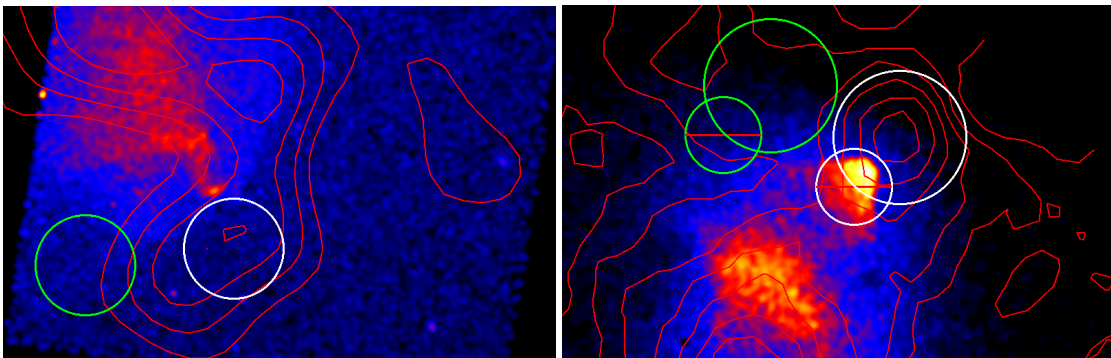


Figure 5.4: The X-ray image of Abell 520 (Left) and the Bullet Cluster (Right) overlaid the gravitational potential from weak gravitational lensing (red, in units of κ , Bullet Cluster contours from (Clowe et al., 2006)). The dark matter blob regions are white circles and the reference regions green circles.

plasma model and several Gaussians (line emission). No physical quantities were derived from the model. It was designed to fit the data with a reduced $\chi^2 \approx 1$ for the numerical analysis of the spectrum (black line in Fig. 5.5). However, the resulting physical parameters of the basis model are typical for clusters. The expected continuous emission of decaying axions was represented by redshifting the fitted expression in Eqn. 5.1 according to the distance of the cluster of galaxies. As seen in Fig. 5.3, the expected spectrum of decaying solar KK axions was only significantly contributing for $E_\gamma = 2.0 - 9.5$ keV, even with the redshifts of the considered clusters taken into account. The complete model (basis + axion) was fitted to the blob region spectrum in this interval with all parameters except the redshift free in the fitting. The resulting values of the reduced $\chi^2/d. o. f.$ are given in Tab. 5.2. The 3σ upper limit (with respect to the fitting residuals) on the luminosity was determined from the fit with the total model normalisations given by the fitted values plus 3σ . I also made an attempt to model the baryonic emission from the reference region spectrum, and subtract it from the blob region spectrum, but the low statistics resulted in huge errors on the luminosity.

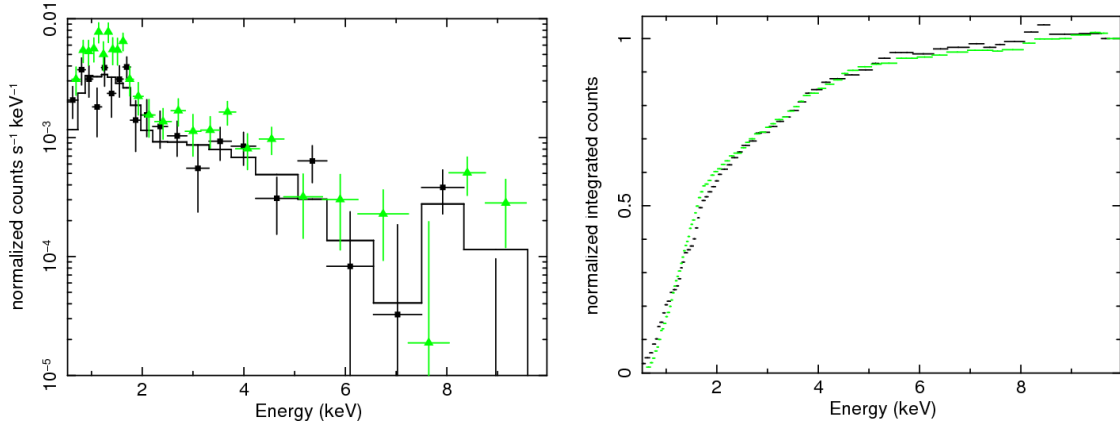


Figure 5.5: (Left) The observed background subtracted spectrum of the blob region (black) of Abell 520 with the fitted "basis model" (black, solid, reduced $\chi^2 \approx 1$) and the spectrum of the reference region (green). (Right) The integrated spectra of the same regions as for the left panel. The deviations between the two spectra is of the order few percent.

	Abell 520	Bullet Cluster
Redshift	0.2 (Ebeling et al., 1998)	0.29 (NASA, 2008)
D_A [Mpc]	662	872
Region radius, $\delta\theta$ [arcmin]	0.85	0.66
Chandra observation id	4215	5356+5361
Exposure time [ksec]	67	179
M_{blob} [$10^{13} M_\odot$]	6.7 ± 2.1	5.8 ± 0.9 (Boyarisky et al., 2008c)
Red $\chi^2/d. o. f.$, basis model	0.78/33	1.04/512
Red $\chi^2/d. o. f.$, basis+expected ^a	0.77/32	1.05/511
3σ total luminosity upper limit [10^{44} erg/sec]	0.2	0.9

Table 5.1: The obtained values as described in Sec. 5.2. ^aThe difference in d. o. f. is due to the different number of free parameters in the models.

5.3 MASSES OF THE REGIONS

For Abell 520, Håkon Dahle derived the masses of the regions from weak gravitational lensing as described in Sec. 4.3.4. The mass of the Bullet Cluster dark matter blob region (SUB) was taken from (Boyersky et al., 2008c). In the merging galaxy cluster systems, the gas has been displaced from the blob regions, so the gas mass can be neglected and the dark matter mass is taken to be the total mass of the blobs.

For Abell 520 the blob region spectrum is shown in Fig. 5.5 (black). The blob region spectra were compared to the spectra of a reference region in the same cluster (green in Fig. 5.5) of same size and shape, and of similar X-ray flux as the blob regions, but with much smaller masses (green in Fig. 5.4). For both clusters, there is a mass contrast of an order of magnitude between the dark matter dominated blob region and the reference region in which the baryons are the dominating source of X-ray emission. As seen in Fig. 5.5, there are no outstanding differences between the emission from the two regions. The difference between the integrated spectra in the right panel is of the order of a few percent at all energies.

5.4 LIFETIMES

A simple estimate of the lifetime of the dark matter particles can be derived from the observed total luminosities: $L = \Gamma E_\gamma N$, where Γ is the decay rate, E_γ is the photon energy, and N is the total number of particles. In the general case of non-relativistic radiative dark matter two-body decays, $E_\gamma = m/2$ for a dark matter candidate of mass m , $N = XM_{DM}/m$, where X is the mass fraction of the dark matter made up of the considered candidate. The lifetime then becomes:

$$\tau = \frac{1}{\Gamma} = \frac{XM_{DM}}{2L}. \quad (5.2)$$

It is worth mentioning that I considered the case where the many individual two-body decay modes produce a wide KK axion bump, which has the shape of the red (lower) curve in Fig. 5.3, but Eqn. 5.2 applies to all dark matter candidates with a continuous emission in the $E_\gamma \approx 2.0 - 9.5$ keV interval.

For the two clusters the observational 3σ upper limits on the luminosities lead to a lower limit on the mean lifetime of the order of $\tau \gtrsim 10^{23}$ sec. The strongest constraint is $\tau \gtrsim 6 \times 10^{24}$ sec from Abell 520 assuming one single dark matter particle constituent with a radiative two-body decay. The luminosity limit is a 3σ upper limit so the main uncertainty in the lifetime constraint comes from the 1σ uncertainty in the mass determination which is approximately 30% for Abell 520 and approximately 20% for the Bullet Cluster. Therefore the uncertainty on the lifetime limit is of the order of 30% at 1σ . This is not a precision measurement, but a determination of the order of magnitude.

5.5 COMPARING TO THE MODEL

For solar KK axions the lifetime has been derived to be $\tau \approx 1.25 \times 10^{20}$ sec for a mean axion rest mass of 5 keV (DiLella & Zioutas, 2003). This is four orders of magnitudes smaller than the lower limit derived from clusters of galaxies assuming the axions to account for all of the dark matter. However the assumed axions produced in the stars (as predicted for the Sun) does not have to be (all of) the dark matter. If the axions only contributes with a small fraction of the total amount of dark matter, the lower limit relaxes and the two lifetimes can become consistent if the fraction is smaller than 0.01%, in which case the star produced axion-like contribution to the dark matter is clearly very small.

5.6 SUMMARY

Dark matter blobs in merging clusters of galaxies are excellent laboratories for constraining fundamental properties of dark matter candidates, like their lifetime. One promising dark matter constituent might have properties similar to the generic KK axion, presumably produced inside stars and proposed to explain the origin of the quiet solar X-ray spectrum which has remained elusive for decades (DiLella & Zioutas, 2003). Trapped by the deep gravitational potential of clusters of galaxies some of the KK axions, or the like, eventually decay isotropically into two X-ray photons and thereby contribute to the diffuse intracluster X-ray emission. Hence, the X-ray emission from dark matter blobs can be taken as a conservative upper limit on the assumed total KK axion luminosity, leading to a lower limit on the KK axion lifetime of $\tau \gtrsim 6 \times 10^{24}$ sec.

Note

Riemer-Sørensen et al. (2007b) made it to the cover of *Physical Review Letters* (Fig. 5.6) and consequently received significant media attention with interviews in several major Danish newspapers (e.g. Politiken, BT) and the story was translated to a number of languages e.g. English, Greek, Dutch, German, Korean. Conclusion: "Always include nice colour figures in your paper..."

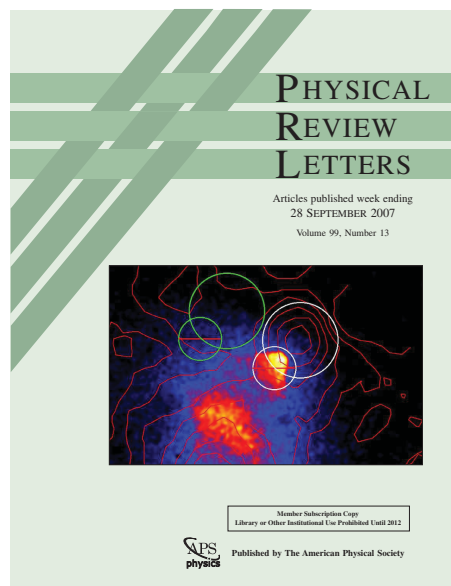


Figure 5.6: The frontpage of *Physical Review Letters* 99.

6

CLUSTERS OF GALAXIES

This chapter provides a short introduction to a few general subjects on galaxy clusters meant as a supplement to the subjects treated in the next chapters about my work on the two clusters Abell 1689 and Abell 1703. If one is already familiar with galaxy clusters, this chapter can be skipped.

6.1 CLUSTERS OF GALAXIES AND THEIR PROPERTIES

Most galaxies in the Universe are found in collections of more than 30 galaxies called clusters. Clusters are the largest systems in the Universe that have had sufficiently time to reach virial equilibrium. Their virial masses ranges from $10^{13} M_{\odot}$ for small groups up to a few $10^{15} M_{\odot}$ for very rich clusters. The mass is dominated by dark matter ($\approx 80\%$) and hot X-ray emitting gas ($\approx 20\%$) with only a few percent from the baryonic matter in the galaxies. With X-ray luminosities of $L_{0.1-2.4\text{keV}} \approx 10^{44} \text{ erg sec}^{-1}$ they are the brightest X-ray sources in the sky. The average temperature of the gas is typically observed to be $T \approx 0.3 - 15 \text{ keV}$ ($\approx 10^7 \text{ K}$, Arnaud, 2005) meaning that the light elements in the gas are completely ionised. Consequently the gas emits X-rays due to thermal bremsstrahlung from the electrons moving in the electromagnetic fields of the nuclei (see Fig. 6.1 Sarazin, 1988).

6.2 CLUSTER MASS

The dominant baryonic matter component of a cluster is the hot intergalactic/intra-cluster gas (Fukugita et al., 1998) which is usually assumed to be optically thin and fully ionised. The cluster mass can be extracted from X-ray observation using a few simple considerations.

A hot intra-cluster gas that is only supported against gravitational infall by its own pressure is described by the equation of hydrostatic equilibrium which for spherical symmetry is (Sarazin, 1988):

$$\frac{dP}{dr} = -\frac{GM_{tot}(< r)\rho_g(r)}{r^2}, \quad (6.1)$$

where P is the pressure of the gas, G is the gravitational constant, $\rho_g(r)$ is the gas density, and $M_{tot}(r)$ is the total mass inside a sphere of radius r including gas, stars, dark matter, spaceships, etc.

At high temperatures and low densities, the gas follows the ideal gas law (Sarazin, 1988):

$$P = \frac{\rho_g(r)T(r)}{\mu m_p}, \quad (6.2)$$

where $T(r)$ is the gas temperature, and μ is the mean molecular weight of the gas in units of



Figure 6.1: The galaxy cluster Abell 1689 observed at optical wavelengths and with the X-ray emission from the hot gas shown in purple (NASA, 2007).

the proton mass, m_p , which is conventionally taken to be 0.6 for known cluster compositions. Combining Eqn. 6.1 and Eqn. 6.2 gives the total mass inside a given radius:

$$M(< r) = -\frac{T(r)}{G\mu m_p} r \left[\frac{d \ln(\rho_g(r))}{d \ln(r)} + \frac{d \ln(T(r))}{d \ln(r)} \right]. \quad (6.3)$$

Assuming the cluster to be isothermal, Eqn. 6.3 reduces to:

$$M_{tot}(< r) = -\frac{\langle T \rangle r}{G\mu m_p} \frac{d(\ln(\rho_g(r)))}{d(\ln(r))}, \quad (6.4)$$

where $\langle T \rangle$ is the characteristic temperature of the gas. Most clusters are not exactly spherical symmetric and consists of several components with different temperatures. Nonetheless, comparisons between X-ray observations and simulations show that Eqn. 6.4 gives a good first order description of the average mass distribution despite the crude approximations (Evrard et al., 1996).

6.3 DETERMINATION OF GAS PROPERTIES

The gas density and temperature can be determined by fitting a model to the X-ray spectrum. The *mekal* model implemented in Xspec, is a model for the emission spectrum from a hot diffuse gas including emission lines from several elements, based on the model calculations of Mewe et al. (1985) with Fe L calculations by Liedahl et al. (1995). Its parameters are temperature, metal abundance relative to solar values, redshift, and normalisation. The intensity of X-ray emission of a hot, tenuous, optically thin gas (which is a good description of the intra cluster medium) scales as the square of the number density as all emission processes are due to collisions between two charged particles (electrons and ions) as for example bremsstrahlung. In the *mekal* model the

relation between the normalisation and the gas density is given by (Arnaud et al., 2009):

$$K = \frac{\text{EI}}{4 \times 10^{14} \pi d_A^2 (1+z)^2}, \quad (6.5)$$

where d_A is the angular diameter distance and $\text{EI} = \int n_e n_H dV$ is called the Emission Integral over volume V of the emission under consideration. The electron number density in the volume is estimated as $\langle n_e \rangle = \sqrt{1.2 \text{EI}/V}$ for $n_e \approx 1.2 n_H$. K has units of cm^{-5} .

Instead of assuming isothermality, the observation is often split into 2D radial bins (e. g. circles as illustrated in Fig. 7.2), and the temperature determined for each bin individually. This is a good approximation, but not perfect, since each bin contain gas with different radii along the line of sight. The temperature analysis can be improved by subtracting the (fainter) spectra from the outer shells before the temperature determination. Xspec has a procedure for this called *project* (Arnaud et al., 2009).

6.4 FROM OBSERVATION TO MASS

The mass within a given radius r_j can be determined following the method of Voigt & Fabian (2006). First the gas pressure given by the ideal gas law can be expressed as $P = nk_B T$ where $n = 1.2 n_H$ is the total particle number density. The pressure gradient between the i 'th and $i+1$ 'th annuli is determined as:

$$\left(\frac{dP}{dr} \right)_j = \left(\frac{P_{i+1} - P_i}{r_{i+1} - r_i} \right)_j, \quad (6.6)$$

where $r_j = (r_i + r_{i+1})/2$. The gas density at r_j (the centre of the j 'th annulus) is determined using linear interpolation $\rho_{g,j} = (\rho_{g,i+1} + \rho_{g,i})/2$ for $\rho_{g,i} = \mu m_H n_i \approx 1.92 \mu m_H n_{e,i}$ leading to a mass within r_j of:

$$M_{tot}(< r_j) = -\frac{1}{G} \frac{r_j^2}{\rho_{g,j}} \left(\frac{dP}{dr} \right)_j. \quad (6.7)$$

The errors can be determined from standard error propagation assuming the parameters to be independent or by a simple Monte Carlo technique perturbing the parameters a number of times.

The method relies on the gas to be in hydrostatic equilibrium and spherically distributed. A slight elongation does not affect the analysis significantly (Donahue et al., 2003; Gavazzi, 2005), but overall the shape must be spherically.

6.5 OTHER OBSERVATIONAL METHODS

6.5.1 GRAVITATIONAL LENSING

Strong and weak gravitational lensing are two different methods of determining the mass of the lensing object(s) based on distortions of the images of background sources. The gravitational field of a galaxy cluster curves the space-time around it so photons emitted from a source behind the cluster travel along curved rather than straight paths on their way to the observer (Fig. 6.2). If the effect is strong enough, there will be multiple paths from the same object past the cluster resulting in multiple images of the same background object. The effect is called strong gravitational lensing, and it can be used to determine the mass distribution of the lensing object within the Einstein radius (the typical distance between the multiple images). Since the source is often an extended object (e. g. a galaxy), the light from different positions in the source will follow slightly different paths resulting in distorted arc-shaped images. This is denoted weak lensing

and is tracing the mass outside the Einstein radius. Thus the two methods are valid in different ranges, overlapping only around the Einstein radius.

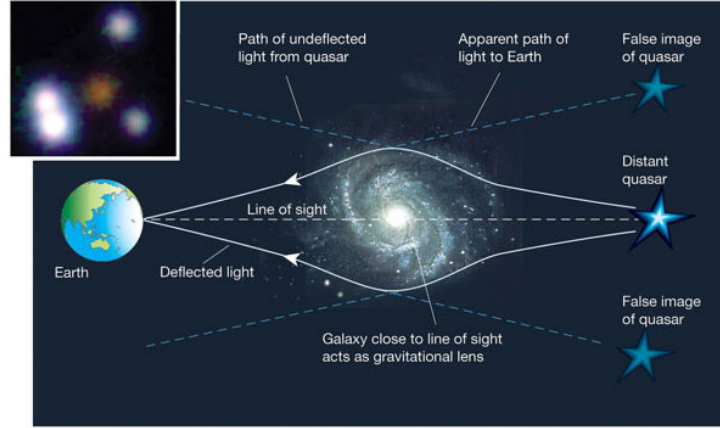


Figure 6.2: Light from a distant quasar (left) is deflected by the gravitational field of a galaxy or galaxy cluster along the line of sight to the Earth (right). As a result, the quasar appears brighter, and multiple images of the quasar may be seen (Turner, 2002).

6.5.2 SUNYAEV-ZEL'DOVICH EFFECT

Another method for mass determination of clusters is the Sunyaev-Zel'dovich (SZ) effect, which is the upscattering of CMB photons on the energetic cluster gas electrons (Sunyaev & Zel'dovich, 1970; Carlstrom et al., 2002). The result is a temperature change of the CMB. The magnitude of the temperature change (actually intensity at a given wavelength) is proportional to the integral of the electron pressure through the cluster, which again depends on the gravitational potential confining the electrons within the cluster. Since the SZ effect is a change in the everywhere-present CMB, it is independent of redshift and hence it is a well suited method for studying distant clusters. Unfortunately the effect is very small, and the method has so far only been applied to a few very well studied clusters, but the field is in rapid development.

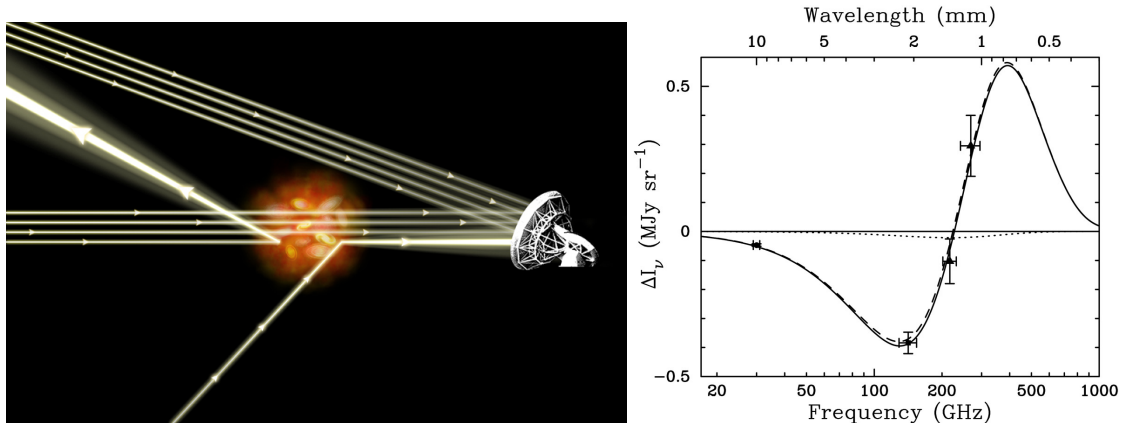


Figure 6.3: (Left) Illustration of the SZ effect (NASA, 2007). (Right) The measured SZ spectrum of Abell 2163. The best-fit thermal (dashed line) and kinetic (dotted line) SZ model spectra are shown together with the combined model (solid line), LaRoque et al., 2002).

7

THE DISCREPANCY BETWEEN LENSING AND X-RAY MASS ESTIMATES OF ABELL 1689

This chapter is heavily based on the article Riemer-Sørensen et al. (2009) where I analysed a new and deep (approximately 180 ksec) *Chandra* X-ray observation of the galaxy cluster Abell 1689.

For many galaxy clusters there is a long-standing discrepancy between their masses determined from X-ray and gravitational lensing. Abell 1689 is a well-studied example (Xue & Wu, 2002; Andersson & Madejski, 2004; Andersson et al., 2007; Lemze et al., 2008; Limousin et al., 2007; Tu et al., 2007; Lemze et al., 2008; Okura et al., 2008; Dahle et al., 2009).

In earlier X-ray analyses the very circular surface brightness of Abell 1689 has been inferred as the cluster being spherically symmetric and in hydrostatic equilibrium. A simple hardness ratio map analysis reveals the cluster is not nice an spherical, but rather consist of a regular part to the South West (SW) in the observation and some structure in the North Eastern (NE) part of the observation. In order to avoid complications and mis-interpretations due to X-ray emission from the substructure, we excluded it from the mass reconstruction. The obtained results were compared to a new weak gravitational study by Dahle et al. (2009) based on a Hubble Space Telescope mosaic covering the central $1.8 \text{ Mpc} \times 1.4 \text{ Mpc}$ and the strong lensing profiles by Limousin et al. (2007). The mass profiles of the regular SW part from two methods are very similar in shape, and the obtained mass profiles are consistent within the uncertainties over the full range where the mass can be reconstructed from X-rays (out to approximately 1 Mpc). The obtained cluster mass within 875 kpc derived from X-rays alone is $6.4 \pm 2.1 \times 10^{14} M_{\odot}$ compared to a weak lensing mass of $8.6 \pm 3.0 \times 10^{14} M_{\odot}$ within the same radius.

7.1 MOTIVATION

The spectrum of the X-ray emission from the gas depends on the temperature of the gas, which for a cluster in hydrostatic equilibrium is related to the total mass. Gravitational lensing uses the distortion of background source images to probe the total mass along the line of sight. It has been widely debated whether cluster mass determinations from the two methods agree, and in some cases large discrepancies have been found (e.g. Loeb & Mao, 1994; Miralda-Escude & Babul, 1995; Voigt & Fabian, 2006; Mahdavi et al., 2007b; Zhang et al., 2008). The main motivation for studying a single cluster, Abell 1689, in large detail with the best available X-ray and lensing data is to get insight into the mass discrepancy by determining the mass distribution using both methods. I also checked that the obtained results were in agreement with those of a third independent mass determination method using the velocity dispersion of the galaxies within the cluster.

Abell 1689 seen in Fig. 7.1 is a massive cluster with a redshift of $z = 0.1832$ (Teague et al., 1990). It is mostly known for its amazing gravitational arcs and large number of multiply im-

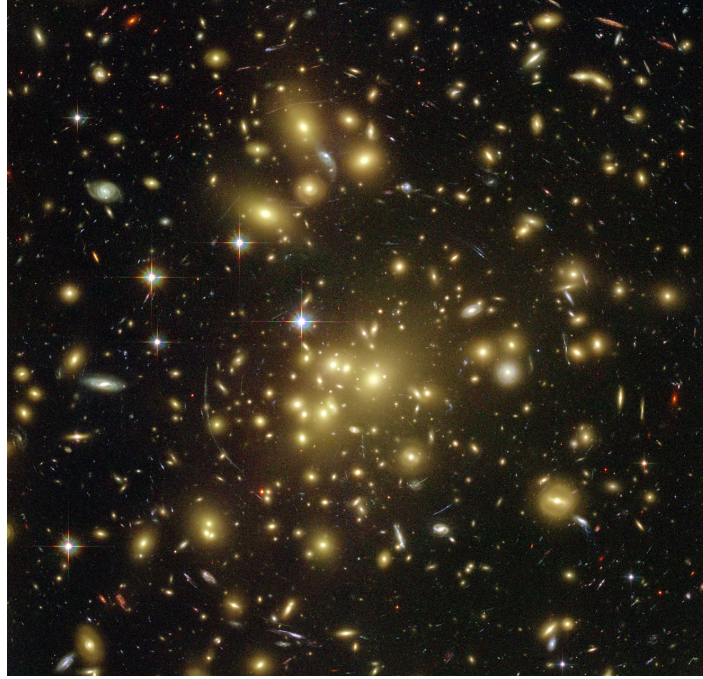


Figure 7.1: (Left) Abell 1689 (image size is approximately $3 \text{ arcmin} \times 3 \text{ arcmin}$). The cluster is most famous for its impressive arcs and a large number of multiply imaged systems (Hubble Space Telescope, 2009).

aged systems. Consequently it has been well studied with strong and weak gravitational lensing (Broadhurst et al., 2005b,a; Halkola et al., 2007; Lemze et al., 2008; Limousin et al., 2007; Dahle et al., 2009). It has been proposed as a standard example of a spherical cluster of galaxies in hydrostatic equilibrium (Xue & Wu, 2002; Lemze et al., 2008). However, earlier studies have found large discrepancies between the mass obtained from X-ray observations and from gravitational lensing (Andersson & Madejski, 2004; Andersson et al., 2007; Lemze et al., 2008; Peng et al., 2009). Strong gravitational lensing analyses have found the central 300 kpc to consist of several subclumps (Limousin et al., 2007; Tu et al., 2007) and weak lensing reveals substructure on a larger scale (500 kpc, Okura et al., 2008; Dahle et al., 2009). Furthermore an indication of substructure in the NE part of Abell 1689 was seen by Andersson & Madejski (2004) in an *XMM* X-ray observation.

7.1.1 DATA

In 2007 new data became available in the form of a very deep X-ray observation with *Chandra* (approximately 150 ks new exposure). In addition, a weak gravitational lensing analysis based on a mosaic using the Wide Field Planetary Camera 2 (WFPC2) instrument aboard the Hubble Space Telescope (HST) had recently been carried out (Dahle et al., 2009). This provides a unique mass map with an unprecedented combination of spatial resolution (50 arcsec) and a large spatial extension. We explored both of these data sets in this work. At the redshift of Abell 1689, 1 arcmin corresponds to 185 kpc for the chosen cosmological model¹.

¹ Λ CDM parameter values: $H_0 = 70.1 \text{ km s}^{-1} \text{ Mpc}^{-1}$, $\Omega_M = 0.23$, $\Omega_b = 0.046$, and $\Omega_\Lambda = 0.72$ (Hinshaw et al., 2009)

Observation id	Date	Exposure time	Data mode
1663	2001 Jan 7	10.73 ks	FAINT
5004	2004 Feb 28	19.86 ks	VFAINT
6930	2006 Mar 06	75.79 ks	VFAINT
7289	2006 Mar 09	74.61 ks	VFAINT

Table 7.1: The analysed *Chandra* observations of Abell 1689. The given exposure times are after light curve cleaning.

7.2 X-RAYS

7.2.1 X-RAY OBSERVATIONS

I analysed four *Chandra* X-ray observations from the NASA HEASARC archive (NASA, 2008) with a total exposure of approximately 180 ks (see Tab. 7.2.1). It has been claimed that the two newest, and by far longest, observations cannot be used due to background issues (Lemze et al., 2008), but these can be overcome as shown in Sec. 7.2.3.

The four observations in Tab. 7.2.1 were reprocessed with the calibration CALDB 3.4.1 and analysed with CIAO 3.4 (Fruscione et al., 2006) following standard procedures as described in Ch. 2 (*Chandra* X-ray Centre, 2009a). I found the X-ray peak of Abell 1689 to have the position (R.A., decl.)=(197.87306°, -1.3413889°). In all observations, the X-ray peak was situated on the ACIS-I3 chip and I performed the analysis with events entirely from this chip.

7.2.2 X-RAY IMAGE AND SURFACE BRIGHTNESS

An exposure corrected X-ray image combined from the four observations is shown in Fig. 7.2. The emission is almost circular tempting one to conclude that Abell 1689 is spherical and in hydrostatic equilibrium. However this is not the case, which is clearly demonstrated by the surface brightness profiles derived from Fig. 7.2 for the NE and SW halves respectively (defined by the dashed white line). Fig. 7.3 shows the ratio between the NE and SW profiles. It is evident that within approximately 300 kpc the SW half is brighter, where outside approximately 500 kpc

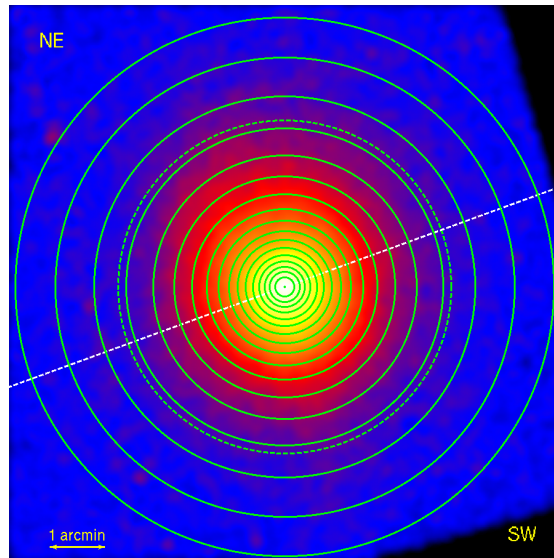


Figure 7.2: Exposure corrected X-ray image composed from the observations in Tab. 7.2.1 (smoothed with a 10 arcsec wide Gaussian). The dashed white line through the X-ray peak (20° angle) divides the cluster in the NE and SW halves. The annuli described in Sec. 7.2.5 are shown in solid green and the 3 arcmin circle in dashed green.

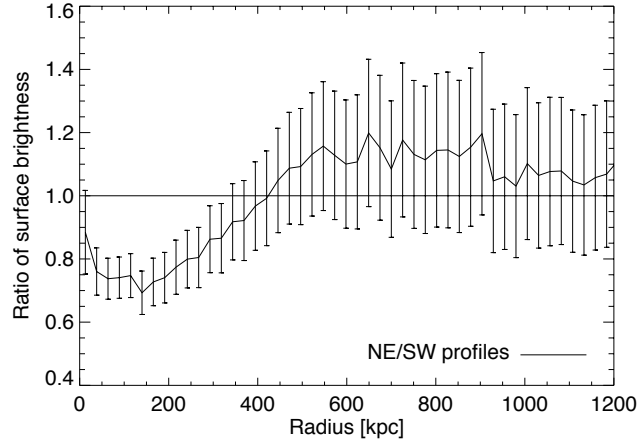


Figure 7.3: The ratio between the surface brightness profiles in the 0.3 – 12.0 keV of the NE and SW halves with Poisson errors.

the two halves are more equally bright with an overall tendency for the NW half to be brighter.

7.2.3 BACKGROUND

Three of the four observations analysed here have been done in the VFAINT telemetry mode (see Sec. 2.2.1).

The standard blank sky observations for background subtraction are produced from observations in the FAINT mode (Markevitch et al., 2003), and hence the shape of the background spectrum from a VFAINT observation deviates from the spectrum of a blank sky observation. However, instead of using the pipeline processed VFAINT data, the data can be reprocessed as FAINT observations. In the latter case, the shape of the background spectra of the two new, long observations 6930 and 7289 are identical to the corresponding blank sky spectra. I extracted the blank sky spectra from the same chip regions as the observed cluster spectra and scaled the blank sky spectrum level to the corresponding observational spectrum in the 9 – 12 keV interval, where very little cluster emission is expected (Markevitch et al., 2003).

Instead of using the blank sky background, it is possible to use the local background from the same observation allowing to take advantage of the improved background reduction in the VFAINT mode. The background differs from chip to chip (in the CCD), so the local background has to be extracted from the same chip as the source region (in this case ACIS-I3). I compared the two methods of background subtraction and the difference between the final results (e.g. the temperature) was negligible. In the following I used the blank sky method whenever extracting spectra, since it allows to use more of the chip for the actual analysis and hence determine the temperature further from the centre of the cluster. For the images I used the VFAINT data since the background event grading is better.

7.2.4 HARDNESS RATIO MAPS

The ratio of low energy photons to high energy photons from the intra cluster medium is a proxy of the temperature structure of the cluster. If the cluster is isothermal and only radiates thermally, the ratio between soft and hard photons (S/H) will be independent of position (within the cluster). However, if there is a variation in temperature, you expect to see a difference in S/H. Even clusters in hydrostatic equilibrium have a radial temperature gradient, which you expect to see

as a circular structure in the soft to hard photon ratio.

From the two longest exposures (observation id 6930 and 7289) I created two hardness ratio maps with different energy splittings between the soft and hard photons. One has a splitting energy of 1.0 keV so $S/H = E[0.3 - 1.0 \text{ keV}]/E[1.0 - 10.0 \text{ keV}]$ and the other of 6.0 keV so $S/H = E[0.3 - 6.0 \text{ keV}]/E[6.0 - 10.0 \text{ keV}]$. I produced a soft and a hard exposure corrected image with a binning of 5 arcsec per pixel. The images were smoothed with a Gaussian of width $\sigma = 5 \text{ arcsec}$, before the soft images were divided by the hard images. For visualisation, the hardness ratio maps were smoothed again with Gaussian of width $\sigma = 15 \text{ arcsec}$, resulting in the two hardness ratio maps shown in Fig. 7.4. Bright colour means excess of low energy photons relative to high. In the case of hydrostatic equilibrium this means colder, but since substructure is rarely in hydrostatic equilibrium, the temperature that can be derived from spectral fitting is not the actual physical temperature.

In the 1.0 keV hardness ratio map (left side of Fig. 7.4) a substructure in the NE part of the cluster is clearly visible, where in the 6.0 keV hardness ratio map (right side of Fig. 7.4) only the (almost) circular symmetric part centered at the X-ray peak is visible.

The splitting of 1 keV is commonly used (e.g. Fabian et al., 2000), but I investigated several splittings between 0.5 keV and 7.0 keV. For splittings between 1.0 keV and 6.0 keV, the hardness ratio map shifts gradually between the two extremes shown in Fig. 7.4, so increasing the splitting energy hides the NE structure and enhances the circular cluster structure.

The contours of the total X-ray emission from Abell 1689 (green in Fig. 7.4) give the impression of being circular with only a slight elongation in the North-South direction. This elongation is more pronounced in the hardness ratio maps with the 1 keV splitting.

In the hardness ratio map with splitting at 6.0 keV there is a relative soft-photon excess centred at the position of the total X-ray peak, which indicates a cooler core in the cluster.

In order to make sure none of the above mentioned features originated in the background, I

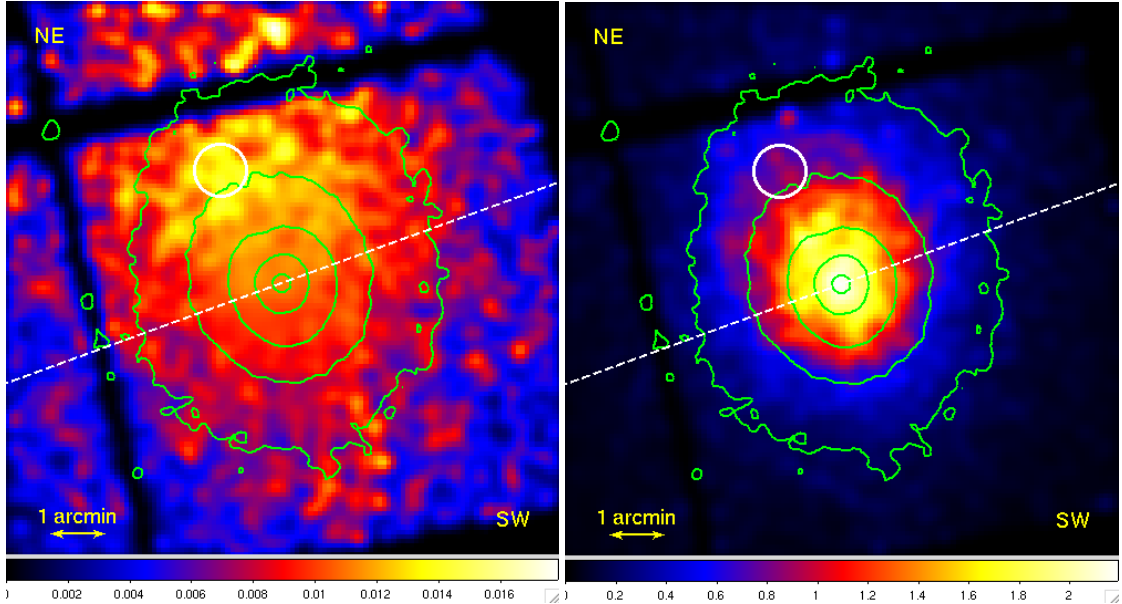


Figure 7.4: Hardness ratio maps (bright is soft photon excess) with the contours of the almost circular total X-ray emission (green). The white line divides the cluster into the NE (upper) and the SW (lower) parts. The white circle is the region analysed in Sec. 7.2.8. (Left) The hardness ratio map for the energy splitting of 1.0 keV ($S/H = E[0.3 - 1.0 \text{ keV}]/E[1.0 - 10.0 \text{ keV}]$). (Right) The hardness ratio map for the energy splitting of 6.0 keV ($S/H = E[0.3 - 6.0 \text{ keV}]/E[1.0 - 10.0 \text{ keV}]$).

created similar hardness ratio maps for the background. As seen in Fig. 7.5 they are completely flat with no structures like those in the observations.

From the hardness ratio maps it is inferred that Abell 1689 consist of a spherically symmetric part, which to the NE is obscured by some substructure. The cooler core indicates that the spherical part of Abell 1689 is relaxed and in hydrostatic equilibrium (Voigt & Fabian, 2006). Therefore I split the cluster into two regions and in the following sections, the temperature and mass profiles have been determined from the symmetrically appearing SW part alone. The division line shown in Fig. 7.2 and Fig. 7.4 (white dashed) goes through the X-ray peak and is tilted by 20° with respect to the East-West direction.

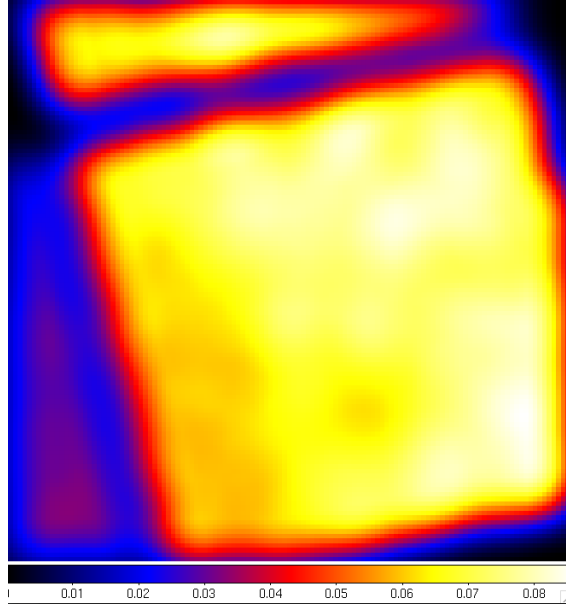


Figure 7.5: Hardness ratio map of the blank sky data for the energy splitting of 1.0 keV.

7.2.5 TEMPERATURE PROFILE

Assuming the intra cluster medium to be an optically thin and completely ionised gas, we determined the global properties of Abell 1689 by analysing a $0.5 - 8.0$ keV spectrum of the central 3 arcmin. This radius was chosen because it includes most of the cluster emission (the dashed green circle in Fig. 7.2) and the same radius is used in earlier analyses (Andersson & Madejski, 2004; Lemze et al., 2008). Using Xspec 12.3 (Arnaud et al., 2009), an isothermal plasma model (*mekal*, Mewe et al., 1985) including Galactic absorption (*wabs*) was fitted to the spectrum. The absorption in neutral hydrogen along the line of sight was fixed to $1.83 \times 10^{20} \text{cm}^{-2}$ (NASA, 2007, n_H tool). Leaving n_H a free parameter while fitting gave a consistent value. The redshift was fixed to $z = 0.183$. The redshift can also be determined from the spectral fitting, but the result had an uncertainty of the order of 20% and as a consequence I used the fixed value. Unfortunately this also excludes the idea of determining the distance along the line of sight to the NE substructure from the spectral fitting.

The resulting global temperature was 10.5 ± 0.1 keV and the abundance 0.37 ± 0.02 solar value for a reduced χ^2 of 1.3 (1725 d. o. f.). This is consistent with earlier reported results (Xue & Wu, 2002; Andersson & Madejski, 2004; Lemze et al., 2008).

Clusters are not isothermal and consequently I made a radial temperature analysis. I re-

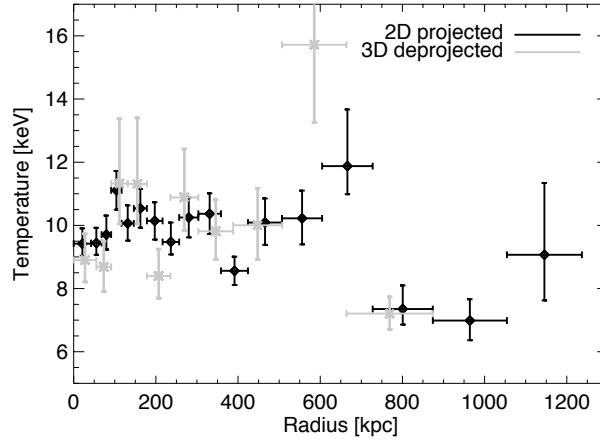


Figure 7.6: The temperature profile reconstructed from the SW symmetric part of Abell 1689. The black diamonds are the 2D projected profile and the grey crosses are the 3D deprojected profile. Apart from one outlier, the profiles are very similar and for the further analysis the 2D projected profiles was used.

stricted the radial temperature analysis to the SW symmetrically appearing half of the cluster.

Using the four data sets and the blank sky background, I extracted the spectra from the SW half of Abell 1689 in 17 half-circular bins centered at the X-ray peak and containing at least 30000 events each (green circles in Fig. 7.2). The same model as for the global properties was fitted to the 0.5 – 8.0 keV spectrum of each radial bin. The obtained (projected, 2D) temperature profile is shown in Fig. 7.6 (black diamonds).

Fitting the complete annuli provides similar temperatures except for the annuli affected by the substructures in the NE part. In general the reduced χ^2 of the fits are closer to one for the half annuli than for the complete annuli.

Since the observed X-ray emission is a superposition of gas shells of different temperatures we proceeded to deproject the temperature profile of Abell 1689 using ten half-circular bins, each containing at least 45000 counts. Using Xspec, the spectra and response matrices for all bins were fitted simultaneously to the same plasma model as for the 2D temperature profile, but now combined with the *project* command, which accounts for the projection effects performing a 3D to 2D projection of prolate shell annuli. Each shell are assumed to have its own temperature and all the temperatures are allowed to vary independently. Spherical symmetry of the SW part was assumed as supported by the hardness ratio maps. The deprojected (3D) temperature profile is shown in Fig. 7.6 as grey crosses.

The two temperature profiles are quite similar and for that reason, I chose to reconstruct the mass profile from the 2D projected temperature profile.

7.2.6 X-RAY MASS PROFILE

Assuming the SW part of Abell 1689 to be one half of a spherical symmetric cluster in hydrostatic equilibrium, the 2D projected temperatures can be used to determine a mass profile following the procedure of Voigt & Fabian (2006) described in Sec. 6.4. The resulting 3D mass profile of the SW part is shown in Fig. 7.7 (black) for the gas density given by the normalisation of the fitted plasma model. The errors bars was determined by standard error propagation.

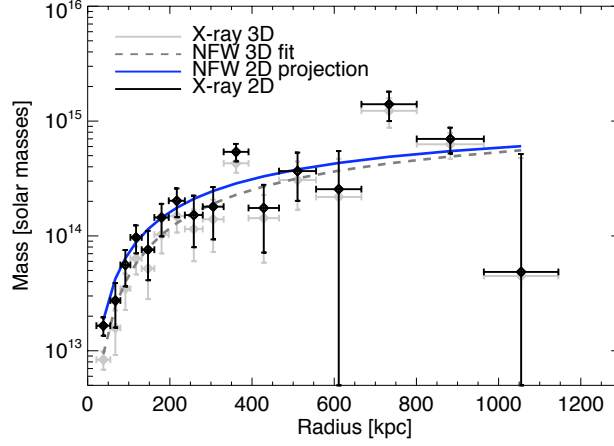


Figure 7.7: The 3D X-ray mass profile (grey diamonds). The fitted NFW-profile is shown as a grey dashed line, and the projected 2D NFW-profile as a blue solid line. The 2D projected X-ray mass profile is shown as black diamonds.

7.2.7 NFW FIT AND PROJECTION

The mass profile determined from X-rays describes the 3D matter distribution (even though derived from the 2D projected spectra). However the mass profiles from gravitational lensing (described in Sec. 7.3.1) are 2D projected profiles, so in order to compare the two profiles, we need to project the X-ray profile. It is most easily done by projecting the density along line of sight, and then integrate along the projected radius, R (Sarazin, 1988):

$$M_{2D}(< R) = \int_0^R 2\pi R' \int_{R'}^{\infty} \frac{\rho_{tot}(r)r}{\sqrt{r^2 - R'^2}} dr dR'. \quad (7.1)$$

If we naively calculate the density profile from the discrete X-ray mass profile, it becomes unphysical with negative densities because of the fluctuations in the mass (even if the uncertainties are taken into account). Instead I investigated how large the projection effect is for different analytical density profiles. The projection mainly affects the inner part of the mass profile by a factor of up to two, and leave the outer parts effectively unchanged. In the very central parts of the cluster, the projection depends on the cuspsiness of the chosen profile. However, the X-ray mass profile does not probe the central part in great detail and the chosen profile is required to reproduce the observed 3D mass profile by fitting, so I used an NFW-profile (Eqn. 1.4). The 3D NFW integrated mass profile was fitted to the 3D X-ray mass profile using reduced χ^2 statistics. The best fit is shown as a dashed grey line in Fig. 7.7 and has the following parameters: $r_s = 174 \pm 10$ kpc, $\rho_0 = (7.79 \pm 0.02) \times 10^6 M_{\odot} \text{ kpc}^{-3}$, for a reduced $\chi^2 = 1.6$ (13 d. o. f.) consistent with earlier published results (Lemze et al., 2008). Solving Eqn. 1.6 gave a concentration parameter of $c_{200} = 10.3$

The NFW-profile was projected using Eqn. 7.1 and the obtained 2D profile was divided by the 3D profile to achieve a radius-dependent projection factor, which ranged from two in the centre to one in the the outer parts. Each point in the 3D X-ray mass profile was converted to a 2D mass profile by multiplying with the projection factor at the corresponding radius. Fig. 7.7 shows the 3D profile as grey diamonds, the fitted NFW-profile as a grey dashed line, the projected 2D NFW-profile as a blue solid line, and the corrected 2D X-ray mass profile as black diamonds. The one σ error bars were correspondingly corrected.

7.2.8 INVESTIGATIONS OF THE NE REGION

The NE region is dominated by soft photons (see Sec. 7.2.4) and for that reason expected to be colder than the SW region (if in thermal equilibrium). Fitting a single temperature component plasma model (same model as above) to the spectrum of the region within the white circle in Fig. 7.4 gave a temperature of 9.3 ± 0.9 keV (reduced $\chi^2 = 0.97$ for 129 d.o.f.). This is slightly colder than the corresponding SW part of the cluster, which has a temperature of 11.1 ± 0.6 keV (reduced $\chi^2 = 1.02$ for 707 d.o.f.) at similar distance to the centre.

The emission from the region is assumed to be a combination of the emission from the SW spherical component plus some softer component. I attempted to determine the temperature of the NE component, by fitting a two temperature model to the spectrum of the NE region. One of the temperatures was fixed to the temperature of the spherical component at the same distance (11.1 keV) while the other temperature was a free parameter of the fit. We obtained a cold component temperature of 1.3 ± 1.0 keV (reduced $\chi^2 = 0.92$ for 128 d.o.f.) with a normalisation of 9% of the normalisation of the warm component. Mazzotta et al. (2004) demonstrates that in general it is very hard to disentangle two temperature components with equal normalisation unless one temperature is around 10 keV and the other one well below a few keV. Comparing to our scenario, the normalisations are not equal. Therefore I tested the stability of the two temperature fit by varying the two temperatures and their fractional normalisation and then fitting for the overall normalisation. This procedure gives similar reduced χ^2 for a range of parameters. For a reduced $\chi^2 < 1.5$ the two temperatures can be varied independently between 4 keV and 14 keV as long as the normalisations stays a free parameter. The conclusion is that the best fit for the NE region is either a two temperature model with a warm and a very cold component or a one temperature model with a temperature slightly lower than the corresponding SW part of the cluster, which is consistent with fitting a one temperature model to a two temperature plasma (Mazzotta et al., 2004).

7.2.9 DISCUSSION OF X-RAY RESULTS

The hardness ratio maps and spectral analysis reveal that Abell 1689 is not spherically symmetric as indicated by the total X-ray image, but rather the observation consists of a spherical main clump centred at the X-ray peak and a softer X-ray emitting substructure to the NE.

The NE substructure is not easily visible in the total X-ray emission. It is because the total cluster X-ray emission is generally dominated by low energy photons almost regardless of gas temperature, which again is dominated by emission from the main cluster. The absolute number of photons leading to the relative difference in the soft to hard photon ratio is simply drowned in the total X-ray emission. However, the substructure is clearly visible in the ratio between the surface brightness profiles of the two halves shown in Fig. 7.3.

The substructure visible to the NE in the hardness ratio is consistent with the *XMM* result of Andersson & Madejski (2004), but it is more distinct in the work presented here.

The hardness ratio map and the temperature profile indicates the core of Abell 1689 to be cooler than the average cluster temperature, which might indicate hydrostatic equilibrium (Voigt & Fabian, 2006).

The temperature profile of the SW part of the cluster is compared to earlier published X-ray temperature profiles in Fig. 7.8. The error bars are smaller than earlier obtained profiles from *Chandra* data (Xue & Wu, 2002; Lemze et al., 2008) due to better statistics, and extends to larger radii due to the use of blank sky background. Only the analysis of *XMM* data by Andersson & Madejski (2004) has comparable statistics and extension. However the temperature profile obtained in this work is generally slightly warmer which leads to an overall larger mass.

The X-ray mass profile as inferred from the SW part of the cluster is well fitted by an NFW-

profile with a concentration parameter of $c_{200} = 10.3$.

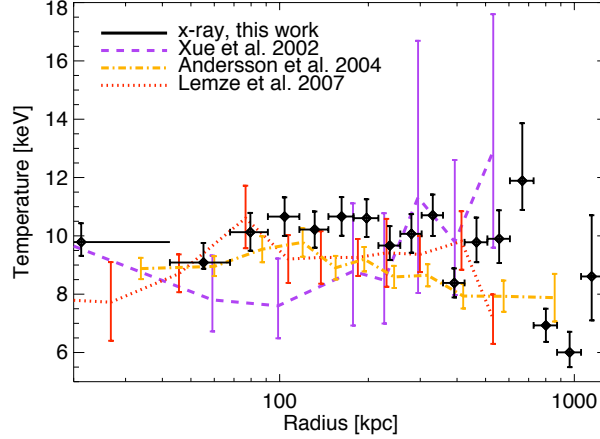


Figure 7.8: Temperature profile compared to earlier results: purple (dashed) from Xue & Wu (2002), orange (dashed dotted) from Andersson & Madejski (2004, 3D deprojected), and red (dotted) from Lemze et al. (2008).

7.3 ADDITIONAL OBSERVATIONS OF ABELL 1689

7.3.1 STRONG AND WEAK LENSING ANALYSES

We compared the X-ray analysis to strong and weak gravitational lensing analyses of Abell 1689. There have been many strong lensing studies of Abell 1689 (Broadhurst et al., 2005b,a; Limousin et al., 2007; Lemze et al., 2008). We used the latest and most detailed by Limousin et al. (2007), which is based on data from the HST Advanced Camera for Surveys (ACS) with the spectroscopic information of the lensed objects from the Keck Telescope and the Very Large Telescope (VLT). The mass reconstruction was done using a Bayesian Monte Carlo Markov Chain method with LENSTOOL (Jullo et al., 2007). The result is an accurate mass mapping of the central parts, which demonstrates a clear bimodality as shown in Fig. 7.9 (black contours). In the very centre there is a main clump associated with the peak of the X-ray emission and then a second significant clump approximately 180 kpc NE of the centre associated with a clump of galaxies (A in Fig. 7.9). Previous studies (Broadhurst et al., 2005a; Halkola et al., 2006) were using fewer spectroscopically confirmed imaged background systems but are in good agreement with the results from Limousin et al. (2007).

For weak gravitational lensing we compared to a recent analysis by Dahle et al. (2009), which is based on a mosaic of 16 HST WFPC2 pointings covering the central $\sim 1.8 \text{ Mpc} \times 1.4 \text{ Mpc}$ of the cluster, complemented at larger radii by ground-based data using the CFH12K mosaic CCD camera at the 3.6 m Canada-France-Hawaii Telescope (CFHT), covering a larger field of $7.7 \text{ Mpc} \times 5.2 \text{ Mpc}$. This provides a unique mass map with an unprecedented combination of spatial resolution (50 arcsec) and a large spatial extension. The surface mass density map from weak gravitational lensing shown in Fig. 7.9 (white contours) was reconstructed by Dahle et al. (2009) using the Kaiser et al. (1995) method. The mass contours clearly shows a non-spherical morphology of Abell 1689 at approximately 500 kpc from the centre (B in Fig. 7.10).

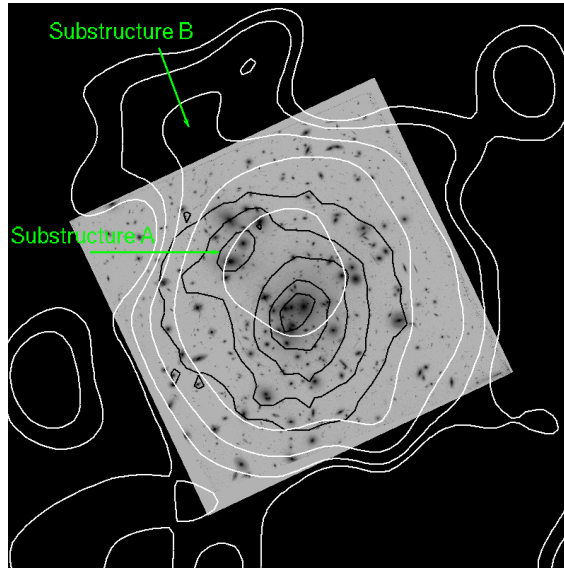


Figure 7.9: Optical images (HST/ACS) with strong (black) and weak (white) gravitational lensing contours. The strong lensing minimum value is $10^9 M_{\odot} \text{ arcsec}^{-2}$ and the distance between contours is $3.5 \times 10^8 M_{\odot} \text{ arcsec}^{-2}$. There is a clear mass peak at the centre of the cluster and a smaller peak 180 kpc to the NE (A). The κ contours from the weak lensing have a resolution of 50 arcsec (FWHM). The minimum value is $\kappa = 0.1$ and the distance between contours is $\delta\kappa = 0.16$. There is clearly a subclump 500 kpc to the NE of centre (B).

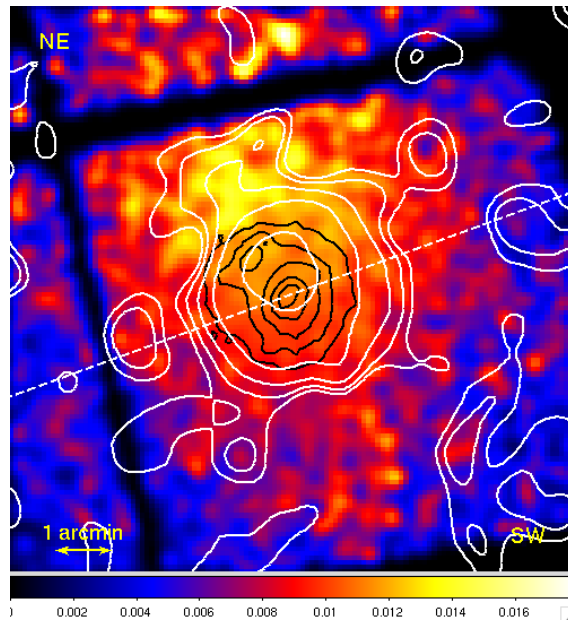


Figure 7.10: Hardness ratio map with energy splitting of 1.0 keV (bright is soft photon excess). The white line divides the cluster into the NE (upper) and SW (lower) parts. The contours are identical to Fig. 7.9 with white being weak gravitational lensing and black strong gravitational lensing.

7.3.2 LENSING MASS PROFILES

From weak lensing the one dimensional radial mass profile was obtained using aperture mass densitometry (Kaiser, 1995; Clowe et al., 2000; Fahlman et al., 1994). This method determines the mean surface mass density within an aperture minus the mean density in a surrounding annulus.

Hence, a lower limit to the projected mass of the lens inside the aperture can be found. The degree of underestimation of the true enclosed mass depends on the inner and outer radii and the slope of the projected mass density profile. For realistic projected density profiles (steeper than r^{-1} at large radii) the mass results presented here will be underestimated by less than 30% at all radii.

For strong gravitational lensing the mass map was integrated in radial bins of 1 arcsec centered on the peak of the X-ray emission, which coincides with the strong lensing mass peak.

For both weak and strong lensing we reconstructed two different radial mass profiles: one by integrating the whole surface density map and the other by integrating the SW half of the surface density map as in the X-ray analysis (multiplied by two to get a complete sphere).

7.3.3 LENSING RESULTS AND DISCUSSION

Both strong and weak lensing analyses show that Abell 1689 is not spherical, but has substructure in the NE direction on both small (180 kpc) and large scales (500 kpc).

The mass profiles of the SW part of Abell 1689 obtained from gravitational lensing are shown in Fig. 7.11. The dashed curves are the integration of the entire mass map and the solid curves are of the SW part only, but multiplied by a factor of two to get a full sphere. The strong lensing mass map is only valid within the Einstein radius (45 arcsec \approx 139 kpc).

For the strong lensing, the mass profile of the entire cluster is very similar to the SW profile, since the NE substructure at 180 kpc is negligible compared to the total mass of the cluster. For the weak lensing, the entire cluster gives a larger value due to the NE substructure also seen in the X-rays. The total mass within 1200 kpc is approximately $9 \times 10^{14} M_{\odot}$. The mass of the NE weak lensing substructure is determined to be $1.25 \pm 0.3 \times 10^{14} M_{\odot}$ within 1.56 arcmin.

In Fig. 7.12 the total cluster mass profiles are compared to earlier gravitational lensing studies of Abell 1689. There is good agreement between the strong lensing mass profiles for radii smaller than 100 kpc. Above 100 kpc, the profile of Dahle et al. (2009) is slightly lower than the earlier profiles (Broadhurst et al., 2005b; Halkola et al., 2007; Umetsu & Broadhurst, 2007).

Assuming the strong lensing mass profile to be the actual 2D projected mass profile of the inner part of Abell 1689 and the X-ray profile to be the actual 3D profile allows us to constrain the

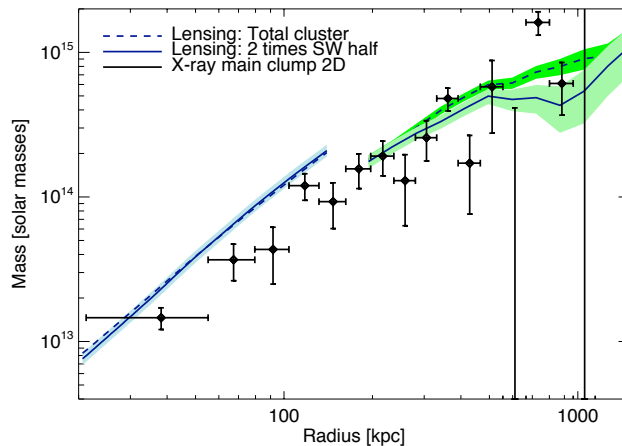


Figure 7.11: The 2D projected mass profile reconstructed from X-ray (black), strong gravitational lensing (blue) and weak gravitational lensing (green). The dashed lensing profile is for integration over the full cluster and the lower solid curve is for integration over the SW part multiplied by two. The width of the shaded regions corresponds to the one sigma errors on the lensing profiles.

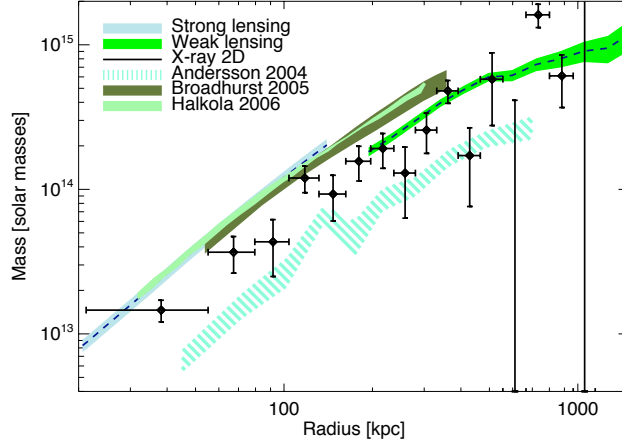


Figure 7.12: The weak and strong gravitational mass profiles (dashed navy) of the total cluster compared to earlier results by Broadhurst et al. (2005b, olive green) and Halkola et al. (2007, green). Our X-ray mass profile is shown (black crosses) together with the one obtained by Andersson & Madejski (2004, aquamarine dashed).

3D to 2D projection factor as a function of radius, which depends on the cuspsiness of the mass profile. The maximally allowed projection factors are $M_{2D}/M_{3D} = (2.8, 4.2, 3.1, 2.6)$ for radii of $r = (38, 67, 92, 188)$ kpc, which are all larger than the factors determined from the NFW-profile projection in Sec. 7.2.7.

7.3.4 REDSHIFT DISTRIBUTION OF CLUSTER GALAXIES

The redshift distribution of the galaxies within Abell 1689 is overall Gaussian (Duc et al., 2002; Teague et al., 1990; Czoske, 2002), but with irregularities (Łokas et al., 2006). The FWHM of the main structure is $\Delta z = 0.02$ corresponding to a line of sight velocity dispersion of nearly 2500 km/s. This is in contrast to other clusters where the value is 1000 – 1200 km/s. It suggests either that Abell 1689 is not in hydrostatic equilibrium or it is a structure with several clumps along the line of sight. The latter interpretation is favoured by Girardi et al. (1997) and by Łokas et al. (2006) who compared the velocity distribution of Abell 1689 to simulations and argued that the high velocity dispersion is due to several clumps along the line of sight. Removing what they found to be separate unbound structures, they got a total dynamical mass of $2 \times 10^{15} M_{\odot}$ within 3.5 Mpc.

Also Lemze et al. (2008) have studied the dynamics of Abell 1689. They derived the virial mass of the cluster to be $1.73 \pm 0.59 \times 10^{15} M_{\odot}$ using the velocity caustics of the cluster galaxies.

7.4 DISCUSSION

Comparing the X-ray hardness ratio maps with the weak and strong gravitational lensing mass maps (Fig. 7.10) we see a coincidence between the substructure in the X-ray emission and the bimodality in the lensing maps. The total X-ray emission (Fig. 7.2) features a slight elongation along the same axis as the secondary clump in the strong lensing map. Further from the centre, the position of the NE substructure in the hardness ratio map coincides with the position of a large substructure in the weak lensing map. On the opposite side, the SW part of the cluster appears circular and symmetric in all observations. From this we concluded that Abell 1689 consist of a spherical main clump and some substructure to the NE, which is interfering with the emission from the NE half of the main clump. The substructure does not have to be associated

with the cluster, but can just as well lie along the line of sight.

The NE half of the cluster is slightly brighter than the SW half at the distance of the weak lensing substructure (Fig. 7.3).

The mass of the substructure is $1.25 \pm 0.3 \times 10^{14} M_{\odot}$ within a radius of 1.56 arcmin determined from weak lensing. This is only a small fraction of the total cluster mass. The gas mass within the same radius has been estimated assuming sphericity and uniform gas density. The result of $9.7 \pm 0.3 \times 10^{12} M_{\odot}$ only contributes with a very small fraction to the total cluster mass. Nonetheless the X-ray emission from the substructure is bright enough to introduce a complication of the spectral analysis and thereby potentially introduce a mis-interpretation of the temperature of the cluster.

Reconstructing mass profiles from the SW half of the main clump only leads to unprecedentedly good agreement between weak and strong gravitational lensing, and the 2D projected X-ray mass profile, which supports the interpretation of Abell 1689 consisting of a spherical main clump and substructure to the NE.

We have quantified the deviation between the different mass profiles by comparing the relevant part of the 2D projected X-ray mass profile to the weak and strong lensing profiles separately. The values of one profile were compared to a linear interpolation of the other profile. The reduced χ^2 was determined to be 1.8 (4 d. o. f.) for the weak lensing and X-ray comparison and 1.2 (10 d. o. f.) for comparison of the strong lensing to the X-ray mass profile.

The cooler core indicates that Abell 1689 is not a recent merger and supports the claim that the SW main clump is in hydrostatic equilibrium. It indicates that the NE substructure is not leftovers from an early collision and maybe not gravitationally interacting with the main clump at all. If it is infalling, the merging is in an early state where the hydrostatic equilibrium of the SW part has not yet been significantly disturbed. The line of sight galaxy velocity distribution supports a scenario with several clumps along the line of sight, where the gas does not interact.

The hardness ratio maps were used as easy diagnostics for the thermal distribution of the cluster, which is related to any substructure. For Abell 1689 the substructure to the NE is visible in a hardness ratio map with an energy splitting of 1.0 keV and a resolution of 10 arcsec made from a 15 ksec subset of the 6930 observation. Many cluster observations have exposures of the order of 15 ksec so we propose to use hardness ratio maps in the selection process of relaxed clusters to be further studied.

7.5 CONCLUSIONS

The new X-ray data analysed here and compared with weak and strong gravitational lensing data show that on large scale the galaxy cluster Abell 1689 appears spherical, in agreement with earlier data. However, both temperature structure and gravitational lensing shows that Abell 1689 contains some substructure to the NE. The NE substructure has an excess emission of soft X-ray photons relative to hard photons. Only the SW half is not significantly influenced by substructure and appears regular.

We have determined the mass profile of the cluster from X-ray observations and compared to recent gravitational lensing results using the SW regular part. The obtained cluster mass within 875 kpc derived from X-rays alone is $6.4 \pm 2.1 \times 10^{14} M_{\odot}$ compared to a weak lensing mass of $8.6 \pm 3.0 \times 10^{14} M_{\odot}$ within the same radius. The profiles are in very good agreement out to 1200 kpc and the discrepancy between X-ray and lensing mass profiles has been significantly reduced due to high quality data.

A way to improve the cluster mass measurements is to combine with observations of the SZ effect, which provide an independent measure of the electron pressure along the line of sight. Unfortunately no SZ observations of Abell 1689 existed at the time of publishing.

THE PERFECT CLUSTER ABELL 1703

The work with Abell 1689 emphasised the importance of the assumptions of sphericity and hydrostatic equilibrium, when deriving the cluster mass from X-ray observations. From a lensing point of view, the galaxy cluster Abell 1703 seems to have these properties and consequently is ideal for studying discrepancies between different mass determinations. It has not been observed in X-rays which lead us to the decision of doing a proposal for *Chandra*. This chapter is based on the proposal submitted in March 2009 on which I was the PI. Unfortunately the proposal was rejected.

8.1 ABSTRACT

We proposed an 80 ksec observation of the cluster of galaxies Abell 1703 to measure its dark matter and gas mass profiles with same precision as obtained from gravitational lensing and compare the result to existing profiles from strong and weak lensing. The cluster appears unimodal and relaxed from lensing analyses, which makes it an exceptional candidate for a cluster fulfilling the assumption of hydrostatic equilibrium that is crucial in the X-ray mass determination.

8.2 INTRODUCTION

The standard Λ CDM cosmology¹ predicts the radial profiles of dark matter halos to be approximately self-similar on mass scales ranging from dwarf galaxies to galaxy clusters. In theory, galaxy clusters are ideal for studying these profiles because they are dark matter dominated apart from the very centre.

Several techniques exist to probe the mass profiles of galaxy clusters, each having certain advantages and disadvantages. The velocity dispersion of member galaxies provides a simple measurement of the total cluster mass. Gravitational lensing (weak and strong) probes the total mass along the line of sight regardless of type and internal distance. Observations of the SZ effect probe the cluster properties far from the center and can be combined with other observations to provide information on the line-of-sight morphology. The dark matter distribution can be investigated and parametrised by comparing to N-body simulations. Including baryonic physics in the simulations is complicated so an alternative approach is to disentangle the baryonic contribution from the observations. X-ray observations can supply the missing information on the baryonic content and at the same time provide an independent measurement of the combined mass.

A key assumption in the X-ray analysis is that the intra cluster medium is a hot plasma

¹ Λ CDM parameter values: $H_0 = 70 \text{ km sec}^{-1} \text{ Mpc}^{-1}$, $\Omega_M = 0.23$, and $\Omega_\Lambda = 0.73$



Figure 8.1: *Abell 1703 observed with HST (image size is approximately 3 arcmin \times 3 arcmin). Notice the very prominent arcs from gravitational lensing (Hubble Space Telescope, 2009).*

in hydrostatic equilibrium, which requires the cluster to be relaxed. Only a few clusters have been intensively studied combining several methods such as Abell 68 (e. g. Richard et al., 2007), Abell 1689 (e. g. Riemer-Sørensen et al., 2009), Abell 2218 (e. g. Elíasdóttir et al., 2007). None of them appear relaxed and they all contain complicated substructures.

Abell 1703 is well studied through weak and strong gravitational lensing and shows properties of being unimodal and relaxed. Therefore it is an excellent candidate for a detailed multi-method analysis potentially improving the understanding of the interplay between dark matter and baryons. The immediate science objectives are:

- Investigate the X-ray morphology of Abell 1703 to check the validity of the hydrostatic equilibrium used to recover the mass profile from X-ray data, and recover this profile (as in Riemer-Sørensen et al. (2009) and Donnarumma et al. (2009)).
- Compare the X-ray mass profile to existing lensing profiles. The two methods are independent and well understood. Consequently an eventual discrepancy between the profiles is possibly due to break down of underlying assumptions, which can be investigated.
- Determine the scale radius precisely. Its location is not sampled by either weak or strong gravitational lensing alone, but lies within the X-ray range.
- Perform a joint lensing and X-ray analysis to identify the best mass model e. g. by combining the probability distributions from lensing and X-ray or by enforcing the scale radius determined from X-ray in the lensing analysis.
- Determine the gas mass profile, which is the main contribution to the baryonic cluster content. Lensing does not distinguish between contributors, so this information can only be obtained from X-rays, and might be used to improve the strong lensing modelling.

On a longer time scale additional science will be possible with data available for multiple methods to study the cluster:

- Constrain the inner density profile slope.
- Investigate effects of gas turbulence.
- Improve the understanding of the interplay between dark matter and baryonic matter.
- Constrain cosmological parameters from a sample of well studied clusters.

8.3 CLUSTER PROPERTIES

Abell 1703 is a massive cluster ($M_{200} \approx 1.8 \times 10^{15} M_{\odot}$, Limousin et al., 2008) located at $z = 0.28$ (1 arcmin = 254 kpc) with a luminosity of $L_{0.1-2.4 \text{ keV}} \approx 5.6 \times 10^{44} \text{ erg sec}^{-1}$ determined from the ROSAT All-Sky Survey (RASS) (Böhringer et al., 2000). There exists good strong (Richard et al., 2009) and weak (Oguri et al., 2009) lensing analyses which shows Abell 1703 as unimodal with a slight elongation along the north-south axis and appearing to be relaxed.

8.3.1 X-RAY

We note that no *Chandra* or *XMM* observations of the cluster exist. Apart from the detection in RASS the only observation is a 8.8 ks ROSAT HRI (High Resolution Imager) exposure (see Fig. 8.2). The background-subtracted HRI observation contains approximately 500 counts which provides a rather noisy surface brightness profile. A β -model (Eqn. 4.1) fit to the surface brightness profile with β fixed to 0.6, gives $r_c = 0.78 \pm 0.56$ arcmin and a normalisation of $0.024 \pm 0.012 \text{ cts sec}^{-1} \text{ arcmin}^{-2}$. The quality of the data does not allow any detailed information on the X-ray azimuthal asymmetry or morphology to be extracted. The best fit $L - M$ relation in Reiprich & Böhringer (2001) implies a value of M_{200} that is about 60% of the strong lensing estimate. Note, however, that the strong lensing only provides reliable constraints on the mass distribution within $50 \text{ arcsec} \approx 0.1 R_{200}$. By adopting the X-ray extrapolation of $M_{200} \approx 1.0 \times 10^{15} h_{70}^{-1} M_{\odot}$ and using the $M - T$ relation of Arnaud et al. (2005), we obtain an estimated gas temperature of $T_{\text{gas}} = 8 \text{ keV}$ and $R_{200} = 1.9 \text{ Mpc}$.

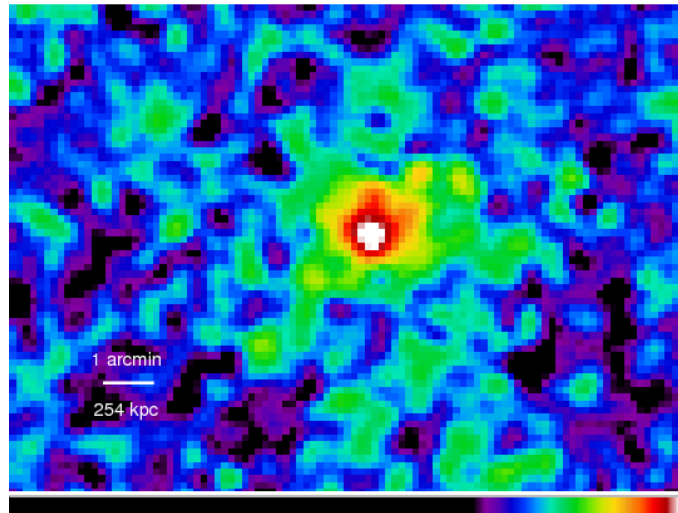


Figure 8.2: Only spatially resolved X-ray image available (ROSAT-HRI exposure).

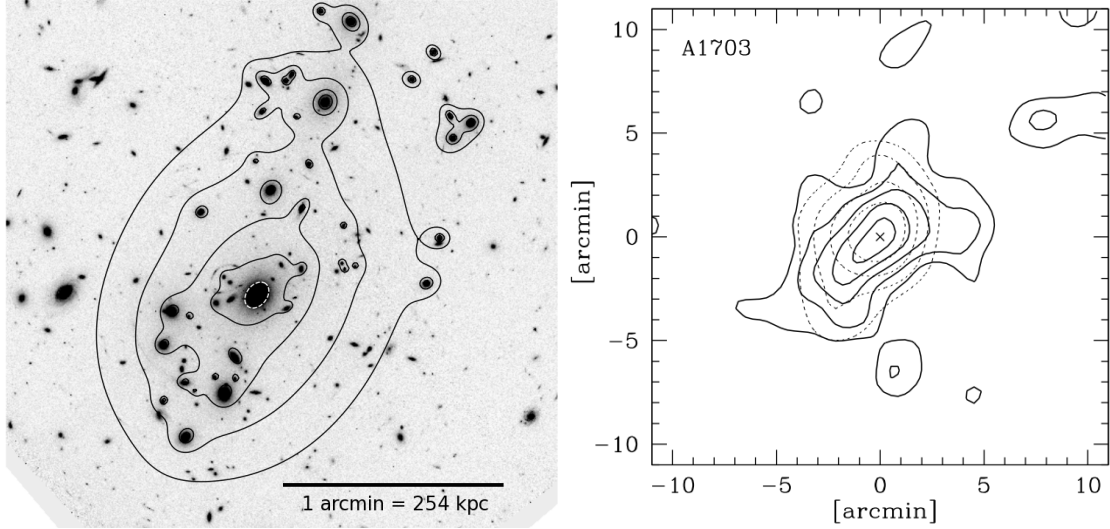


Figure 8.3: (Left) Strong lensing mass contours (solid) overlaid the HST/ACS F850W frame and the light distribution from the central cD galaxy (dashed). (Right) Two-dimensional mass maps (solid) reconstructed from weak lensing shear measurements (from Oguri et al., 2009) and contours of constant luminosity densities of red-sequence galaxies (dotted).

8.3.2 GRAVITATIONAL LENSING

Abell 1703 has been observed with the HST (total ACS exposure > 50 ksec) and with the Subaru and Keck telescopes. These unique observations have motivated several gravitational lensing analyses (Limousin et al., 2008; Saha & Read, 2009; Richard et al., 2009; Broadhurst et al., 2008; Oguri et al., 2009).

The most recent strong lensing study (Richard et al., 2009) incorporates spectroscopic redshifts for 10 out of a total of 16 multiply imaged systems, confirming and strengthening the results from previous works: From the geometrical configuration of its multiply imaged systems, in particular its giant arc located at approximately 35 arcsec from the centre, Abell 1703 appears overall spherically symmetric with the centre dominated by a giant elliptical cD galaxy. The best fit strong lensing model is a unimodal cluster with a single dark matter clump centered on the cD galaxy and a slight elongation along the north-south axis (see Fig. 8.3). Other well studied clusters with similar quality data such as Abell 1689 and Abell 2218 are clearly bi- or multi-modal. Moreover, in Abell 1703 the light distribution from the cD galaxy is consistent with the central part of the overall mass distribution. These facts suggest that Abell 1703 is a relaxed unimodal cluster, which is rare at these redshifts (Smith et al., 2005). Using the strong lensing model, Richard et al. (2009) predicted a large scale shear signal that is consistent with weak lensing measurements inferred from Subaru data out to $4h^{-1}$ Mpc, which is further evidence for a relaxed, unimodal cluster.

The contribution of the cluster gas is usually neglected in strong lensing modelling, so the addition of a well determined gas profile from X-ray might improve the modelling.

Recent weak lensing studies by Oguri et al. (2009) of Subaru Suprime-Cam images (g, r, i bands) confirms the unimodality and regular shape of the cluster out to approximately 5 arcmin as seen in Fig. 8.3.

The mild elongation of the cluster does not severely bias the X-ray analysis (Donahue et al., 2003; Gavazzi, 2005) and can be accounted for in the analysis.

8.3.3 SUNYAEV-ZEL'DOVICH EFFECT

Combining lensing and X-ray data with observations of the SZ effect in clusters, allows us to over-constrain the physical properties and thereby shed new light on the systematics introduced by the a-priori assumptions of hydrostatic equilibrium, spherical geometry and the absence of sub-structures. In particular, by comparing the observed SZ Compton parameter with that retrieved from X-ray, we can recover information on the 3D morphology of the cluster. The biases associated with the spectrally determined X-ray temperature (emission weighted) can be determined by comparing to the temperatures obtained from SZ (where the temperature is a mass-weighted temperature). Moreover, a joint X-ray, SZ and lensing analysis can be used to study the outer region of clusters well beyond the regions resolved by X-ray observations ($\approx 0.6R_{200}$), thanks to the strong sensitivity of the SZ effect on the electron pressure in the outer cluster regions. We will apply for a CARMA observation of Abell 1703.

8.4 FEASIBILITY

The objective is to derive a mass profile from X-ray with relative uncertainties smaller or comparable to those of the lensing profiles ($\approx 20\%$). We propose a 80 ksec timed observation with *Chandra* since it has the best combination of spatial resolution, sensitivity and field of view needed for the project.

The good spatial resolution is required both to identify point sources and to spatially resolve the spectroscopic properties of the inner 50 arcsec where the strong lensing model is valid. *XMM* would only marginally resolve the core radius due to its larger Point-Spread Function. The optimal instrument is ACIS-I due to its larger field of view and lower background with respect to ACIS-S (up to a factor of 2 in the 0.5 – 7.0 keV band). These characteristics will allow a reconstruction of the temperature and mass profile of Abell 1703 out to 4.9 arcmin $\approx R_{500} \approx 0.6R_{200}$.

In the following we have assumed the cluster emission to follow the ROSAT-HRI β -profile (scaled to *Chandra* using PIMMS, CXO Proposers' Observatory Guide, 2009), a galactic absorption of $1.2 \times 10^{20} \text{cm}^{-2}$, a metallicity of $0.3Z_{\odot}$ (Anders & Grevesse, 1989) and a mean temperature of $T_{gas} = 8 \text{keV}$.

For any given exposure there is a trade-off between the number of radial bins, the number of photons in each bin, and the exposure time.

The cluster mass can be determined from the temperature profile following the procedure described in Voigt & Fabian (2006) with the uncertainties obtained through standard error propagation. In order for the uncertainties to be smaller than 20%, the temperature of each bin must be determined to better than 10%.

The ROSAT luminosity predicts a total count rate of around 0.5cts sec^{-1} (and background of 0.02cts sec^{-1}). We require a minimum of two radial temperature bins within the central 50 arcsec where the strong lensing constraints are reliable to compare the shape of the mass profiles and a minimum of 5 bins in the resulting mass profile.

To determine the necessary number of counts in each bin, we have modelled realistic cluster spectra in Xspec using the thermal *mekal* model. From the model spectra we have simulated data with *fakedit* and the newest *Chandra* calibration data (version 4.1.1) and reconstructed the temperatures. At least 5000 counts is needed in each spectrum to obtain uncertainties of maximum 10%. With the above requirements we get a total of 8 radial bins extending to a maximum radius of 4.9 arcmin for an exposure of 80 ksec.

Reconstructing the mass profile from the simulated temperatures, we get the profile shown in Fig. 8.4 together with the best fit NFW mass profiles from lensing (Richard et al., 2009; Oguri et al., 2009).

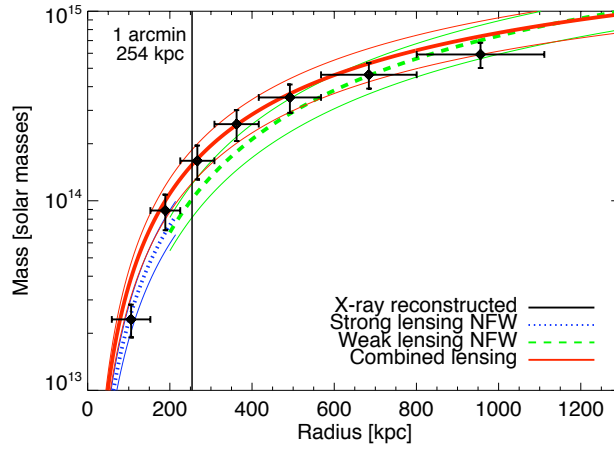


Figure 8.4: Reconstructed simulated mass profile from 80 ksec Chandra observation compared to the weak (dashed green), strong (dotted blue), and combined (solid red) lensing best fit NFW-profiles from Oguri et al. (2009); Richard et al. (2009). Thin lines indicate approximate lensing uncertainties.

With a shorter exposure time the mass can be reconstructed in fewer radial bins, which does not allow for a comparison to strong and weak lensing profiles independently.

Due to its regular shape and the impression of being relaxed, Abell 1703 is an outstanding candidate for a multi-wavelength study of the cluster mass distribution combining existing high quality weak and strong lensing analyses with the X-ray observation applied for here. The combination of strong and weak lensing, X-ray, and SZ analyses is a very promising technique to pinpoint the exact shape of the dark matter profile and improve the understanding of the interplay between dark matter and baryons (Mahdavi et al., 2007c).

9

CONCLUDING REMARKS

Despite large observational and theoretical efforts, the identity of the dark matter remains a mystery, with a myriad of possible candidates.

A well motivated candidate is the keV-mass sterile neutrino, which apart from a dark matter candidate also yields a natural solution for the active neutrino masses and oscillations, and the baryon asymmetry of the Universe. Via an allowed decay into an active neutrino and a photon, it provides a testable signature in the form of a mono-chromatic X-ray emission line. I have performed line searches in X-ray observations of several types of objects, with a negative result. The non-detection lead to very general constraints on the line emission from dark matter in the 0.3 – 10.0 keV range (Fig. 9.1). The flux constraints were converted to constraints in the mass-mixing angle parameter space for the sterile neutrinos (Fig. 9.1). Different objects such as the galactic halo, colliding galaxy clusters, and spheroidal dwarf galaxies gives similar constraints, which is very affirmative since they provide independent measurements. The Milky Way halo gives the best constraint on the flux alone. Nonetheless, the dwarf galaxies are most promising when it comes to strengthen the constraints on decay rate or the mass-mixing angle, since they are nearby, massive, dark matter dominated, and have very little X-ray emission. Combining the X-ray constraints with constraints on the structure formation history from observations of the Lyman α forest, the simplest production scenarios for the sterile neutrinos (Dodelson-Widrow) can

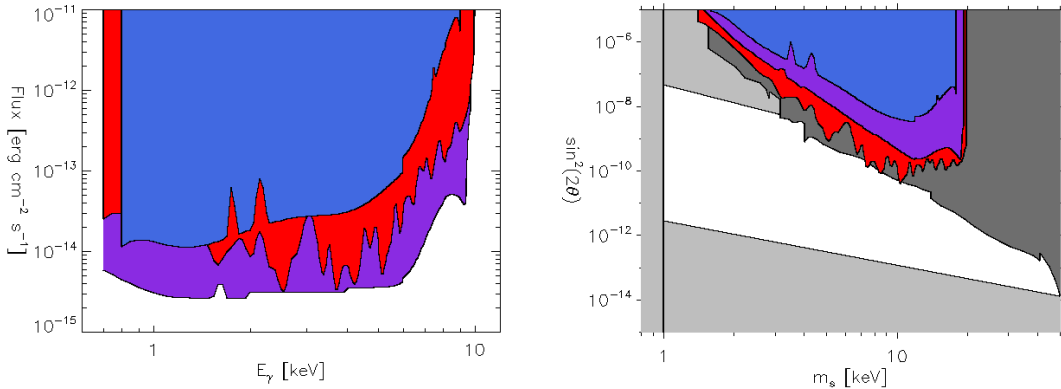


Figure 9.1: (Left) The obtained upper limits on the line emission flux as explained in Ch. 4: The Milky Way halo (violet), Draco (red), and Abell 520 (blue). (Right) The constraints in the $m_s - \sin^2(2\theta)$ parameter space for sterile neutrinos of the Majorana type (taken from Boyarsky et al., 2009d): Phase space considerations (grey below 1 keV), BBN (grey region in the bottom), oscillatory production giving $\Omega > \Omega_{DM}$ (grey region in the top), earlier observational constraints (dark grey), the Milky Way halo (violet), Draco (red), and Abell 520 (blue).

be ruled out. More complicated scenarios are likewise constrained by the X-ray observations, but cannot be ruled out with the current observations. A different statistical approach using stacked residual spectra and time series analysis methods has the potential of excluding the remaining parameter space without the need for new observations. This should be investigated further.

The X-ray analysis has also been extended to continuous emission from dark matter such as decaying axions. In this case, the resulting lifetime for a specific scenario of solar axions, was in clear contradiction to the one obtained from X-ray observations of the quiet Sun, thus ruling out the specific solar axion as a dark matter candidate.

The mass determination of galaxy clusters is a way to understand the dark matter clustering properties at large scale. Gravitational lensing and X-ray are independent methods for determining the mass profiles. I have carried out a case study of the galaxy cluster Abell 1689 for which earlier analyses reported a notable disagreement between the methods. High quality data allowed the identification of substructure in the North Eastern part of the cluster. Removing this substructure from the mass determination and assuming the remaining part of the cluster to be spherical and in hydrostatic equilibrium resulted in profiles that over the observed radii are consistent with the lensing profiles within the uncertainties (Fig. 9.2). The conclusion is that substructure easily confuses the analysis, so the best clusters to use for combining independent mass determination methods must be spherical and without substructure. Unfortunately it is well known, that clusters with significant substructure provides more multiple images and arches, making them more suited for lensing analyses even though they are less suited for X-ray analysis. Abell 1703 seems to be a very good candidate for a combined analysis since its alignment provide a giant arc to facilitate the lensing modelling and the best fitting lensing model is unimodal and almost circular, indicating hydrostatic equilibrium. These are ideal cluster properties for studying the origin of the discrepancies between the masses derived from gravitational lensing and X-ray. Open questions for the future are: What is the importance of hydrostatic equilibrium when deriving the mass from X-rays? Given an overall agreement between X-ray and lensing mass determination methods, can we use the X-ray data to study small scale structure and turbulence? Can the 3D shape of clusters be inferred from X-ray analysis alone? Observations of

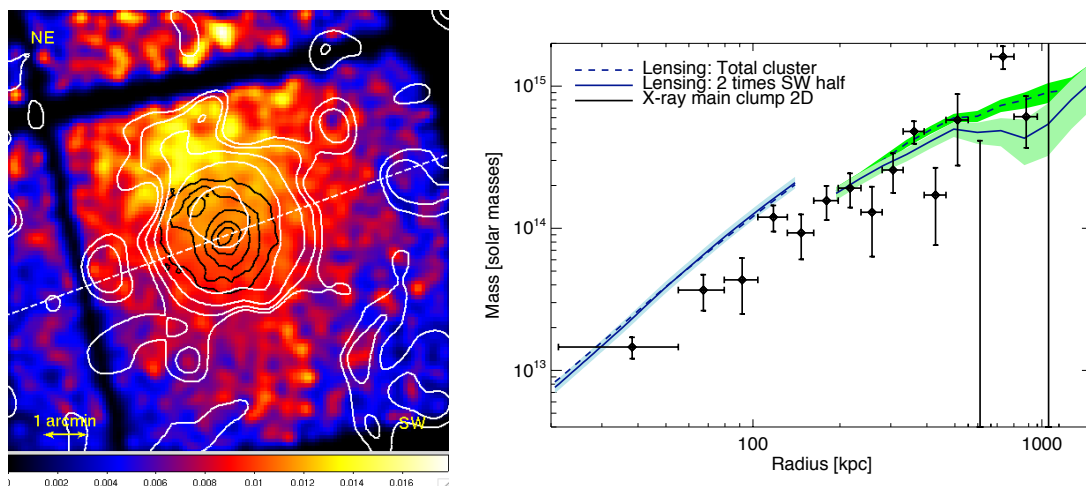


Figure 9.2: (Left) Hardness ratio map with energy splitting of 1.0 keV (bright is soft photon excess). The substructure in the upper left part is clearly visible in both the hardness ratio map and the weak gravitational lensing contours (white). Also the strong lensing (black) shows substructure but at a different length scale. (Right) The mass profiles reconstructed from X-ray (black), strong gravitational lensing (blue), and weak gravitational lensing (green) are in good agreement.

the SZ effect is a third independent method for mass determination, which combined with the lensing and X-ray data allows for a 3D mapping of the mass.

With this thesis I have not identified the dark matter or even finished the characterisation of its properties. Luckily this only makes the field more interesting for the future, where the fast development probably will continue...



Figure 9.3: *Piled Higher and Deeper*, Gorge Cham, November 19 2007

ACKNOWLEDGEMENTS

I would have liked to start my thesis with "I have always been fascinated by the night sky and dreamed of becoming an astrophysicist since I was a child", but that is very very far from the truth. Nevertheless, when I went to school my class mates actually called me "the astrophysicist" for a period. Not related to any interest in the Universe, but merely because it was the most difficult sounding and nerdy nickname they could come up with. Somehow it seems like they were more predictive than intended. Many years later I started studying particle physics and over the last years I have slightly changed focus so now I think of myself as astrophysicist (okay, with a twist of particle physics, so I do not get too bored with all the photons).

The path to becoming an astrophysicist has not been entirely straight, and I have received help and support from a lot of people. I have felt very privileged doing my PhD at the inspiring Dark Cosmology Centre with superb colleagues locally and abroad, supervisors who believed in me, all the support I needed from friends and family, and the most wonderful and supporting boyfriend.

COAUTHOR STATEMENTS

Paper I

Probing the nature of dark matter with cosmic x rays: Constraints from "dark blobs" and grating spectra of galaxy clusters

Signe Riemer-Sørensen, Kristian Pedersen, Steen H. Hansen & Håkon Dahle
Physical Review D (2007) 76 043524

Sec. 4.3 is based on this paper. Signe Riemer-Sørensen did the X-ray analysis and the calculations for the gratings. She also wrote most of the paper based on discussions with Kristian Pedersen and Steen Hansen, and made all of the figures. Håkon Dahle provided the lensing masses and the contours for Fig. 1.



Signe Riemer-Sørensen



Kristian Pedersen



Steen H. Hansen

Paper II

Searching for Decaying Axionlike Dark Matter from Clusters of Galaxies

Signe Riemer-Sørensen, Konstantin Zioutas, Steen H. Hansen, Kristian Pedersen, Håkon Dahle & Anastasios Liolios

Physical Review Letters (2007) **99** 131301

Ch. 5 is based on this paper. Konstantin Zioutas suggested to look for solar axions in X-ray observations of galaxy clusters. Signe Riemer-Sørensen did the entire X-ray analysis and the calculations of the lifetimes. Signe also wrote most of the paper based on discussions with Steen Hansen, Kristian Pedersen and Konstantin Zioutas, and made all of the figures. Håkon Dahle provided the lensing masses and contours for Abell 520. Anastasios Liolios did the section on the lifetime estimate from the total radiation density.



Signe Riemer-Sørensen



Kristian Pedersen



Steen H. Hansen

Paper III

Resolving the Discrepancy Between Lensing and X-Ray Mass Estimates of the Complex Galaxy Cluster Abell 1689

*Signe Riemer-Sørensen, Danuta Paraficz, Desiree D. M. Ferreira, Kristian Pedersen, Marceau Limousin
& Håkon Dahle*

Astrophysical Journal (2009) **693** 1570

Ch. 7 is based on this paper. Signe Riemer-Sørensen did the X-ray analysis apart from the de-projection which was done by Desiree D. M. Ferreira. Signe wrote most of the paper apart from the sections on gravitational lensing, which were mainly written by Danuta Paraficz. Signe made all of the figures. Marceau Limousin provided the strong lensing data which were analysed by Danuta Paraficz, and Håkon Dahle provided the weak lensing masses and contours. All authors contributed in various ways to the discussion and conclusions.



Signe Riemer-Sørensen



Danuta Paraficz



Marceau Limousin

Paper IV

Decaying dark matter in Draco

Signe Riemer-Sørensen & Steen H. Hansen
Astronomy and Astrophysics (2009) **500** L37

Sec. 4.5 is based on this paper. Signe Riemer-Sørensen did the entire analysis and made all of the figures while Steen H. Hansen helped writing the paper.



Signe Riemer-Sørensen



Steen H. Hansen

BIBLIOGRAPHY

- Abazajian, K. 2006, *Phys. Rev. D*, 73, 063506
- Abazajian, K., Fuller, G. M., & Patel, M. 2001a, *Phys. Rev. D*, 64, 023501
- Abazajian, K., Fuller, G. M., & Tucker, W. H. 2001b, *ApJ*, 562, 593
- Abazajian, K. & Koushiappas, S. M. 2006, *Phys. Rev. D*, 74, 023527
- Abazajian, K. N., Markevitch, M., Koushiappas, S. M., & Hickox, R. C. 2007, *Phys. Rev. D*, 75, 063511
- Abdo, A. A., The Fermi LAT Collaboration, et al. 2009, *Physical Review Letters*, 102, 181101
- Adriani, O., The PAMELA Collaboration, et al. 2009, *Nature*, 458, 607
- Aharonian, F., The H. E. S. S. Collaboration, et al. 2009, *arXiv:0905.0105*
- Allen, S. W., Schmidt, R. W., & Fabian, A. C. 2002, *MNRAS*, 334, L11
- Amsler, C., The Particle Data Group, et al. 2008, *Phys. Lett.*, B667, 1
- Anders, E. & Grevesse, N. 1989, *Geochim. Cosmochim. Acta*, 53, 197
- Andersson, K. E. & Madejski, G. M. 2004, *ApJ*, 607, 190
- Andersson, K. E., Peterson, J. R., & Madejski, G. M. 2007, *ApJ*, 670, 1010
- Angus, G. W. 2009, *arXiv:0907.1526*
- Argyriades, J., The NEMO-3 Collaboration, et al. 2009, *arXiv:0906.2694*
- Arkani-Hamed, N., Dimopoulos, S., & Dvali, G. 1998, *Physics Letters B*, 429, 263
- Arnaud, K., Dorman, B., & Gordon, C. 2009, *An X-Ray Spectral Fitting Package User's Guide for version 12.5.0*, from <http://heasarc.gsfc.nasa.gov/docs/xanadu/xspec/manual/manual.html>
- Arnaud, M. 2005, in *Background Microwave Radiation and Intracluster Cosmology*, ed. F. Melchiorri & Y. Rephaeli, 77
- Arnaud, M., Pointecouteau, E., & Pratt, G. W. 2005, *Astron. Astrophys.*, 441, 893
- Asaka, T., Blanchet, S., & Shaposhnikov, M. 2005, *Physics Letters B*, 631, 151
- Asaka, T., Laine, M., & Shaposhnikov, M. 2006a, *Journal of High Energy Physics*, 6, 53
- Asaka, T. & Shaposhnikov, M. 2005, *Physics Letters B*, 620, 17
- Asaka, T., Shaposhnikov, M., & Kusenko, A. 2006b, *Physics Letters B*, 638, 401
- Asaka, T., Shaposhnikov, M., & Laine, M. 2007, *Journal of High Energy Physics*, 1, 91
- Asztalos, S. J., Rosenberg, L. J., van Bibber, K., Sikivie, P., & Zioutas, K. 2006, *Annual Review of Nuclear and Particle Science*, 56, 293

- Barger, V., Phillips, R. J. N., & Sarkar, S. 1995, *Physics Letters B*, 352, 365
- Bergstrom, L. 2009, arXiv:0903.4849
- Bernabei, R., Belli, P., Cappella, F., Cerulli, R., Dai, C. J., D'Angelo, A., He, H. L., Incicchitti, A., Kuang, H. H., Ma, J. M., Montecchia, F., Nozzoli, F., Prospero, D., Sheng, X. D., & Ye, Z. P. 2008, *European Physical Journal C*, 167
- Biermann, P. L. & Kusenko, A. 2006, *Physical Review Letters*, 96, 091301
- Bode, P., Ostriker, J. P., & Turok, N. 2001, *ApJ*, 556, 93
- Bøhm, C., Riazuelo, A., Hansen, S. H., & Schaeffer, R. 2002, *Phys. Rev. D*, 66, 083505
- Böhringer, H., Voges, W., Huchra, J. P., McLean, B., Giacconi, R., Rosati, P., Burg, R., Mader, J., Schuecker, P., Simiç, D., Komossa, S., Reiprich, T. H., Retzlaff, J., & Trümper, J. 2000, *ApJS*, 129, 435
- Boyanovsky, D. 2008, *Phys. Rev. D*, 78, 103505
- Boyarsky, A., den Herder, J.-W., Neronov, A., & Ruchayskiy, O. 2007a, *Astroparticle Physics*, 28, 303
- Boyarsky, A., Iakubovskiy, D., Ruchayskiy, O., & Savchenko, V. 2008a, *MNRAS*, 387, 1361
- Boyarsky, A., Lesgourgues, J., Ruchayskiy, O., & Viel, M. 2009a, *Journal of Cosmology and Astro-Particle Physics*, 5, 12
- . 2009b, *Physical Review Letters*, 102, 201304
- Boyarsky, A., Malyshev, D., Neronov, A., & Ruchayskiy, O. 2008b, *MNRAS*, 387, 1345
- Boyarsky, A., Neronov, A., Ruchayskiy, O., & Shaposhnikov, M. 2006a, *MNRAS*, 370, 213
- . 2006b, *Phys. Rev.*, D74, 103506
- Boyarsky, A., Neronov, A., Ruchayskiy, O., Shaposhnikov, M., & Tkachev, I. 2006c, *Physical Review Letters*, 97, 261302
- Boyarsky, A., Nevalainen, J., & Ruchayskiy, O. 2007b, *A&A*, 471, 51
- Boyarsky, A., Ruchayskiy, O., & Iakubovskiy, D. 2009c, *Journal of Cosmology and Astro-Particle Physics*, 3, 5
- Boyarsky, A., Ruchayskiy, O., & Markevitch, M. 2008c, *ApJ*, 673, 752
- Boyarsky, A., Ruchayskiy, O., & Shaposhnikov, M. 2009d, arXiv:0901.0011
- Bringmann, T., Bergström, L., & Edsjö, J. 2008, *Journal of High Energy Physics*, 1, 49
- Broadhurst, T., Benítez, N., Coe, D., Sharon, K., Zekser, K., White, R., Ford, H., Bouwens, R., Blakeslee, J., Clampin, M., Cross, N., Franx, M., Frye, B., Hartig, G., Illingworth, G., Infante, L., Menanteau, F., Meurer, G., Postman, M., Ardila, D. R., Bartko, F., Brown, R. A., Burrows, C. J., Cheng, E. S., Feldman, P. D., Golimowski, D. A., Goto, T., Gronwall, C., Herranz, D., Holden, B., Homeier, N., Krist, J. E., Lesser, M. P., Martel, A. R., Miley, G. K., Rosati, P., Sirianni, M., Sparks, W. B., Steindling, S., Tran, H. D., Tsvetanov, Z. I., & Zheng, W. 2005a, *ApJ*, 621, 53
- Broadhurst, T., Takada, M., Umetsu, K., Kong, X., Arimoto, N., Chiba, M., & Futamase, T. 2005b, *ApJ*, 619, L143
- Broadhurst, T., Umetsu, K., Medezinski, E., Oguri, M., & Rephaeli, Y. 2008, *Astrophys. J.*, 685, L9
- Cabibbo, N. 1963, *Phys. Rev. Lett.*, 10, 531

- Carlstrom, J. E., Holder, G. P., & Reese, E. D. 2002, *ARA&A*, 40, 643
- Cash, W. 1979, *ApJ*, 228, 939
- Catena, R. & Ullio, P. 2009, arXiv:0907.0018
- CERN. 2009, CERN webpage, <http://cern.ch>
- Chang, J., Adams, J. H., Ahn, H. S., Bashindzhagyan, G. L., Christl, M., Ganel, O., Guzik, T. G., Isbert, J., Kim, K. C., Kuznetsov, E. N., Panasyuk, M. I., Panov, A. D., Schmidt, W. K. H., Seo, E. S., Sokolskaya, N. V., Watts, J. W., Wefel, J. P., Wu, J., & Zatsepin, V. I. 2008, *Nature*, 456, 362
- Chikashige, Y., Gelmini, G., Peccei, R. D., & Roncadelli, M. 1980, *Phys. Lett.*, B94, 499
- Clowe, D., Bradač, M., Gonzalez, A. H., Markevitch, M., Randall, S. W., Jones, C., & Zaritsky, D. 2006, *ApJ*, 648, L109
- Clowe, D., Luppino, G., Kaiser, N., & Gioia, I. 2000, *ApJ*, 539, 540
- CXO Proposers' Observatory Guide. 2008, *Chandra X-ray Centre* (Cambridge: *Chandra X-ray Centre*), <http://cxc.harvard.edu/proposers/POG/html>
- . 2009, *Chandra X-ray Centre* (Cambridge), <http://cxc.harvard.edu/toolkit/pimms.jsp>
- Czoske, O. 2002, PhD thesis, Université Paul Sabatier, Toulouse III, France
- Dahle, H., Kaiser, N., Irgens, R. J., Lilje, P. B., & Maddox, S. J. 2002, *ApJS*, 139, 313
- Dahle, H. et al. 2009, in preparation
- Dalcanton, J. J. & Hogan, C. J. 2001, *ApJ*, 561, 35
- D'Amico, G., Kamionkowski, M., & Sigurdson, K. 2009, arXiv:0907.1912
- Davis, T. M., Mörtzell, E., Sollerman, J., Becker, A. C., Blondin, S., Challis, P., Clocchiatti, A., Filippenko, A. V., Foley, R. J., Garnavich, P. M., Jha, S., Krisciunas, K., Kirshner, R. P., Leibundgut, B., Li, W., Matheson, T., Miknaitis, G., Pignata, G., Rest, A., Riess, A. G., Schmidt, B. P., Smith, R. C., Spyromilio, J., Stubbs, C. W., Suntzeff, N. B., Tonry, J. L., Wood-Vasey, W. M., & Zenteno, A. 2007, *ApJ*, 666, 716
- Davis, J. E. 2008, The S-lang webpage, <http://www.s-lang.org/>
- de Gouvea, A. 2005, *Phys. Rev.*, D72, 033005
- Diemand, J., Kuhlen, M., Madau, P., Zemp, M., Moore, B., Potter, D., & Stadel, J. 2008, *Nature*, 454, 735
- Dienes, K. R., Dudas, E., & Gherghetta, T. 2000, *Phys. Rev. D*, 62, 105023
- DiLella, L. & Zioutas, K. 2003, *Astroparticle Physics*, 19, 145
- Dodelson, S. & Liguori, M. 2006, *Physical Review Letters*, 97, 231301
- Dodelson, S. & Widrow, L. M. 1994, *Physical Review Letters*, 72, 17
- Dolgov, A. D. 2002, *Phys. Rep.*, 370, 333
- Dolgov, A. D. & Hansen, S. H. 2002, *Astroparticle Physics*, 16, 339
- Dolgov, A. D., Hansen, S. H., Pastor, S., Petcov, S. T., Raffelt, G. G., & Semikoz, D. V. 2002, *Nuclear Physics B*, 632, 363
- Dolgov, A. D., Hansen, S. H., Raffelt, G., & Semikoz, D. V. 2000, *Nuclear Physics B*, 590, 562
- Donahue, M., Gaskin, J. A., Patel, S. K., Joy, M., Clowe, D., & Hughes, J. P. 2003, *ApJ*, 598, 190

- Donato, F., Gentile, G., Salucci, P., Frigerio Martins, C., Wilkinson, M. I., Gilmore, G., Grebel, E. K., Koch, A., & Wyse, R. 2009, arXiv:0904.4054
- Donnarumma, A., Ettori, S., Meneghetti, M., & Moscardini, L. 2009, arXiv:0902.4051
- Duc, P.-A., Poggianti, B. M., Fadda, D., Elbaz, D., Flores, H., Chanial, P., Franceschini, A., Moorwood, A., & Cesarsky, C. 2002, *A&A*, 382, 60
- Duffy, L. D. & van Bibber, K. 2009, arXiv:0904.3346
- Dunkley, J., Komatsu, E., Nolta, M. R., Spergel, D. N., Larson, D., Hinshaw, G., Page, L., Bennett, C. L., Gold, B., Jarosik, N., Weiland, J. L., Halpern, M., Hill, R. S., Kogut, A., Limon, M., Meyer, S. S., Tucker, G. S., Wollack, E., & Wright, E. L. 2009, *ApJS*, 180, 306
- Ebeling, H., Edge, A. C., Bohringer, H., Allen, S. W., Crawford, C. S., Fabian, A. C., Voges, W., & Huchra, J. P. 1998, *MNRAS*, 301, 881
- Ehle, M., Breitfellner, M., Díaz Trigo, M., González Riestra, R., Guainazzi, M., Loiseau, N., Rodríguez, P., Santos-Lleó, M., Schartel, N., Tomás, L., Verdugo, E., & Dahlem, M. 2007, http://xmm2.esac.esa.int/external/xmm_user_support/documentation/uhb_2.5/index.html
- Elíasdóttir, Á., Limousin, M., Richard, J., Hjorth, J., Kneib, J.-P., Natarajan, P., Pedersen, K., Jullo, E., & Paraficz, D. 2007, arXiv:0710.5636
- Evrard, A. E., Metzler, C. A., & Navarro, J. F. 1996, *ApJ*, 469, 494
- Fabian, A. C. et al. 2000, *MNRAS*, 318, L65
- Fahlman, G., Kaiser, N., Squires, G., & Woods, D. 1994, *ApJ*, 437, 56
- Freeman, P., Doe, S., & Siemiginowska, A. 2001, in *Society of Photo-Optical Instrumentation Engineers (SPIE) Conference Series*, Vol. 4477, Society of Photo-Optical Instrumentation Engineers (SPIE) Conference Series, ed. J.-L. Starck & F. D. Murtagh, 76–87
- Fruscione, A., McDowell, J. C., Allen, G. E., Brickhouse, N. S., Burke, D. J., Davis, J. E., Durham, N., Elvis, M., Galle, E. C., Harris, D. E., Huenemoerder, D. P., Houck, J. C., Ishibashi, B., Karovska, M., Nicastro, F., Noble, M. S., Nowak, M. A., Primini, F. A., Siemiginowska, A., Smith, R. K., & Wise, M. 2006, in *Society of Photo-Optical Instrumentation Engineers (SPIE) Conference Series*, Vol. 6270, Society of Photo-Optical Instrumentation Engineers (SPIE) Conference Series
- Fukugita, M., Hogan, C. J., & Peebles, P. J. E. 1998, *ApJ*, 503, 518
- Fuller, G. M., Kusenko, A., Mocioiu, I., & Pascoli, S. 2003, *Phys. Rev. D*, 68, 103002
- Gavazzi, R. 2005, *A&A*, 443, 793
- Gilmore, G., Wilkinson, M., Kleyna, J., Koch, A., Evans, W., Wyse, R. F. G., & Grebel, E. K. 2007, *Nuclear Physics B Proceedings Supplements*, 173, 15
- Girardi, M., Fadda, D., Escalera, E., Giuricin, G., Mardirossian, F., & Mezzetti, M. 1997, *ApJ*, 490, 56
- Goldstone, J., Salam, A., & Weinberg, S. 1962, *Phys. Rev.*, 127, 965
- Gorbunov, D., Khmelnsky, A., & Rubakov, V. 2008, *Journal of Cosmology and Astro-Particle Physics*, 10, 41
- Gorbunov, D. & Shaposhnikov, M. 2007, *Journal of High Energy Physics*, 10, 15
- Halkola, A., Seitz, S., & Pannella, M. 2006, *MNRAS*, 372, 1425
- . 2007, *ApJ*, 656, 739

- Halzen, F. & Martin, A. D. 1984, Quarks and Leptons: Introductory Course in Modern Particle Physics (John Wiley & Sons)
- Hannestad, S., Mirizzi, A., & Raffelt, G. 2005, Journal of Cosmology and Astro-Particle Physics, 7, 2
- Hannestad, S. & Raffelt, G. G. 2002, Physical Review Letters, 88, 071301
- . 2004, Phys. Rev. D, 69, 029901
- Haynes, M. P. 2009, From <http://www.astro.cornell.edu/academics/courses/astro201/coma.htm>
- Hecht, E. 2001, Optics 4th edition (Addison Wesley)
- Hinshaw, G., Weiland, J. L., Hill, R. S., Odegard, N., Larson, D., Bennett, C. L., Dunkley, J., Gold, B., Greason, M. R., Jarosik, N., Komatsu, E., Nolte, M. R., Page, L., Spergel, D. N., Wollack, E., Halpern, M., Kogut, A., Limon, M., Meyer, S. S., Tucker, G. S., & Wright, E. L. 2009, ApJS, 180, 225
- Hofmann, S., Schwarz, D. J., & Stöcker, H. 2001, Phys. Rev. D, 64, 083507
- Horvat, R., Krčmar, M., & Lakić, B. 2004, Phys. Rev. D, 69, 125011
- Hubble Space Telescope. 2009, <http://www.spacetelescope.org>
- Irby, B. 2008a, The fv webpage, <http://heasarc.gsfc.nasa.gov/docs/software/ftools/fv/>
- . 2008b, The ftools webpage, HeaSoft, http://heasarc.gsfc.nasa.gov/docs/software/ftools/ftools_menu.html
- Jeltema, T. E. & Profumo, S. 2008, ApJ, 686, 1045
- Jullo, E. et al. 2007, New J. Phys., 9, 447
- Kaiser, N. 1995, ApJ, 439, L1
- Kaiser, N., Squires, G., & Broadhurst, T. 1995, ApJ, 449, 460
- Karttunen, H., Kröger, P., Oja, H., Poutanen, M., & Donner, K. J. 1996, Fundamental Astronomy (Springer)
- Kayser, B. 2008, arXiv:0804.1497
- Kim, J. E. & Carosi, G. 2008, arXiv:0807.3125
- Kishimoto, C. T. & Fuller, G. M. 2008, Phys. Rev. D, 78, 023524
- Klypin, A., Zhao, H., & Somerville, R. S. 2002, ApJ, 573, 597
- Kobayashi, M. & Maskawa, T. 1973, Progress of Theoretical Physics, 49, 652
- Komatsu, E., Dunkley, J., Nolte, M. R., Bennett, C. L., Gold, B., Hinshaw, G., Jarosik, N., Larson, D., Limon, M., Page, L., Spergel, D. N., Halpern, M., Hill, R. S., Kogut, A., Meyer, S. S., Tucker, G. S., Weiland, J. L., Wollack, E., & Wright, E. L. 2009, ApJS, 180, 330
- Koposov, S. E., Yoo, J., Rix, H.-W., Weinberg, D. H., Macciò, A. V., & Escudé, J. M. 2009, ApJ, 696, 2179
- Kusenko, A. 2004, Int. J. Mod. Phys., D13, 2065
- Kusenko, A. 2009, arXiv:0906.2968
- Kusenko, A. & Segrè, G. 1997, Physics Letters B, 396, 197
- Laine, M. & Shaposhnikov, M. 2008, Journal of Cosmology and Astro-Particle Physics, 6, 31
- LaRoque, S. J., Carlstrom, J. E., Reese, E. D., Holder, G. P., Holzzapfel, W. L., Joy, M., & Grego, L. 2002, ArXiv Astrophysics e-prints

Lattanzi, M. & Silk, J. 2009, *Phys. Rev. D*, 79, 083523

Lemze, D., Barkana, R., Broadhurst, T. J., & Rephaeli, Y. 2008, *MNRAS*, 386, 1092

Lemze, D., Broadhurst, T., Rephaeli, Y., Barkana, R., & Umetsu, K. 2008, arXiv:0810.3129

Lesgourgues, J. & Pastor, S. 2006, *Phys. Rep.*, 429, 307

Lewis, A. & Bridle, S. 2002, *Phys. Rev. D*, 66, 103511

Liedahl, D. A., Osterheld, A. L., & Goldstein, W. H. 1995, *ApJ*, 438, L115

Limousin, M., Richard, J., Jullo, E., Kneib, J.-P., Fort, B., Soucail, G., Elíasdóttir, Á., Natarajan, P., Ellis, R. S., Smail, I., Czoske, O., Smith, G. P., Hudelot, P., Bardeau, S., Ebeling, H., Egami, E., & Knudsen, K. K. 2007, *ApJ*, 668, 643

Limousin, M., Richard, J., Kneib, J.-P., Brink, H., Pelló, R., Jullo, E., Tu, H., Sommer-Larsen, J., Egami, E., Michałowski, M. J., Cabanac, R., & Stark, D. P. 2008, *A&A*, 489, 23

Lin, D. N. C. & Faber, S. M. 1983, *ApJ*, 266, L21

Loeb, A. & Mao, S. 1994, *ApJ*, 435, L109

Loewenstein, M., Kusenko, A., & Biermann, P. L. 2009, *ApJ*, 700, 426

Lokas, E. L., Prada, F., Wojtak, R., Moles, M., & Gottloeber, S. 2006, *MNRAS*, 366, L26

Maggiore, M. 2003, *A Modern Introduction to Quantum Field Theory* (Oxford University Press)

Mahdavi, A., Hoekstra, H., Babul, A., Balam, D. D., & Capak, P. L. 2007a, *ApJ*, 668, 806

Mahdavi, A., Hoekstra, H., Babul, A., & Henry, J. P. 2007b, preprint, arXiv:0710.4132 [astro-ph]

Mahdavi, A., Hoekstra, H., Babul, A., Sievers, J., Myers, S. T., & Henry, J. P. 2007c, *ApJ*, 664, 162

Mapelli, M. & Ferrara, A. 2005, *MNRAS*, 364, 2

Markevitch, M. 2002, arXiv:astro-ph/0205333

Markevitch, M., Bautz, M. W., Biller, B., Butt, Y., Edgar, R., Gaetz, T., Garmire, G., Grant, C. E., Green, P., Juda, M., Plucinsky, P. P., Schwartz, D., Smith, R., Vikhlinin, A., Virani, S., Wargelin, B. J., & Wolk, S. 2003, *ApJ*, 583, 70

Markevitch, M., Gonzalez, A. H., Clowe, D., Vikhlinin, A., Forman, W., Jones, C., Murray, S., & Tucker, W. 2004, *ApJ*, 606, 819

Markevitch, M., Govoni, F., Brunetti, G., & Jerius, D. 2005, *ApJ*, 627, 733

Mazzotta, P., Rasia, E., Moscardini, L., & Tormen, G. 2004, *MNRAS*, 354, 10

McKenzie, D. 2002, YOHHOH webpage, <http://www.lmsal.com/SXT/homepage.html>

Merritt, D., Graham, A. W., Moore, B., Diemand, J., & Terzić, B. 2006, *AJ*, 132, 2685

Mewe, R., Gronenschild, E. H. B. M., & van den Oord, G. H. J. 1985, *A&AS*, 62, 197

Mikheev, S. P. & Smirnov, A. Y. 1985, *Sov. J. Nucl. Phys.*, 42, 913

Miralda-Escude, J. & Babul, A. 1995, *ApJ*, 449, 18

Moore, B., Ghigna, S., Governato, F., Lake, G., Quinn, T., Stadel, J., & Tozzi, P. 1999, *ApJ*, 524, L19

Nambu, Y. 1960, *Phys. Rev.*, 117, 648

- Narayanan, V. K., Spergel, D. N., Davé, R., & Ma, C.-P. 2000, *ApJ*, 543, L103
- NASA. 2007, *Chandra* webpage http://www.nasa.gov/mission_pages/chandra/spacecraft/index.html
- NASA. 2007, n_H tool of HeaSoft, <http://heasarc.gsfc.nasa.gov>
- . 2008, HEASARC, <http://heasarc.gsfc.nasa.gov/docs/archive.html>
- NASA/WMAP Science Team. 2008, <http://map.gsfc.nasa.gov/media/080997/index.html>
- Navarro, J. F., Frenk, C. S., & White, S. D. M. 1996, *ApJ*, 462, 563
- Oguri, M., Hennawi, J. F., Gladders, M. D., Dahle, H., Natarajan, P., Dalal, N., Koester, B. P., Sharon, K., & Bayliss, M. 2009, *ApJ*, 699, 1038
- Okabe, N. & Umetsu, K. 2008, *PASJ*, 60, 345
- Okura, Y., Umetsu, K., & Futamase, T. 2008, *ApJ*, 680, 1
- Pal, P. B. & Wolfenstein, L. 1982, *Phys. Rev. D*, 25, 766
- Peccei, R. D. & Quinn, H. R. 1977, *Physical Review Letters*, 38, 1440
- Peng, E. ., Andersson, K., Bautz, M. W., & Garmire, G. P. 2009, arXiv:0906.4153
- Petraki, K. 2008, *Phys. Rev. D*, 77, 105004
- Petraki, K. & Kusenko, A. 2008, *Phys. Rev. D*, 77, 065014
- Randall, S. W., Markevitch, M., Clowe, D., Gonzalez, A. H., & Bradač, M. 2008, *ApJ*, 679, 1173
- Reale, F., Peres, G., & Orlando, S. 2001, *ApJ*, 557, 906
- Regis, M. & Ullio, P. 2008, *Phys. Rev. D*, 78, 043505
- Reiprich, T. H. & Böhringer, H. 2001, in *Mining the Sky*, ed. A. J. Banday, S. Zaroubi, & M. Bartelmann, 208–+
- Richard, J., Kneib, J.-P., Jullo, E., Covone, G., Limousin, M., Ellis, R., Stark, D., Bundy, K., Czoske, O., Ebeling, H., & Soucail, G. 2007, *ApJ*, 662, 781
- Richard, J., Pei, L., Limousin, M., Jullo, E., & Kneib, J. P. 2009, *A&A*, 498, 37
- Riemer-Sørensen, S. & Hansen, S. H. 2009, *A&A*, 500, L37
- Riemer-Sørensen, S., Hansen, S. H., & Pedersen, K. 2006, *ApJ*, 644, L33
- Riemer-Sørensen, S., Paraficz, D., Ferreira, D. D. M., Pedersen, K., Limousin, M., & Dahle, H. 2009, *ApJ*, 693, 1570
- Riemer-Sørensen, S., Pedersen, K., Hansen, S. H., & Dahle, H. 2007a, *Phys. Rev. D*, 76, 043524
- Riemer-Sørensen, S., Zioutas, K., Hansen, S. H., Pedersen, K., Dahle, H., & Liolios, A. 2007b, *Physical Review Letters*, 99, 131301
- Riess, A. G. et al. 1998, *Astron. J.*, 116, 1009
- Ryden, B. 2003, *Introduction to cosmology* (Addison Wesley)
- Saha, P. & Read, J. I. 2009, *Astrophys. J.*, 690, 154
- Sarazin, C. L. 1988, *X-ray emission from clusters of galaxies* (Cambridge University Press available at <http://nedwww.ipac.caltech.edu/level5/March02/Sarazin/frames.html>)

- Savage, C., Gelmini, G., Gondolo, P., & Freese, K. 2009, *Journal of Cosmology and Astro-Particle Physics*, 4, 10
- Schmidt, R. W., Allen, S. W., & Fabian, A. C. 2001, *MNRAS*, 327, 1057
- Seljak, U., Makarov, A., McDonald, P., & Trac, H. 2006, *Physical Review Letters*, 97, 191303
- Shaposhnikov, M. 2007, *Nucl. Phys.*, B763, 49
- Shaposhnikov, M. 2008, *Journal of High Energy Physics*, 8, 8
- Shaposhnikov, M. & Tkachev, I. 2006, *Physics Letters B*, 639, 414
- Shi, X. & Fuller, G. M. 1999, *Physical Review Letters*, 82, 2832
- SkyView, N. 2009, <http://skyview.gsfc.nasa.gov/>
- Smith, G. P., Kneib, J.-P., Ebeling, H., Czoske, O., & Smail, I. 2001, *ApJ*, 552, 493
- Smith, G. P., Kneib, J.-P., Smail, I., Mazzotta, P., Ebeling, H., & Czoske, O. 2005, *MNRAS*, 359, 417
- Smithsonian Astrophysical Observatory. 2009, The ds9 webpage, <http://hea-www.harvard.edu/RD/ds9/>
- Spekkens, K., Giovanelli, R., & Haynes, M. P. 2005, *AJ*, 129, 2119
- Springel, V., Frenk, C. S., & White, S. D. M. 2006, *Nature*, 440, 1137
- Springel, V., White, S. D. M., Frenk, C. S., Navarro, J. F., Jenkins, A., Vogelsberger, M., Wang, J., Ludlow, A., & Helmi, A. 2008, *Nature*, 456, 73
- Strigari, L. E., Bullock, J. S., Kaplinghat, M., Simon, J. D., Geha, M., Willman, B., & Walker, M. G. 2008, *Nature*, 454, 1096
- Strigari, L. E., Koushiappas, S. M., Bullock, J. S., & Kaplinghat, M. 2007, *Phys. Rev. D*, 75, 083526
- Sunyaev, R. A. & Zel'dovich, Y. B. 1970, *Comments on Astrophysics and Space Physics*, 2, 66
- Taoso, M., Bertone, G., & Masiero, A. 2008, *Journal of Cosmology and Astro-Particle Physics*, 3, 22
- tcl.tk. 2009, The main Tcl Developer Xchange site, <http://www.tcl.tk/>
- Teague, P. F., Carter, D., & Gray, P. M. 1990, *ApJS*, 72, 715
- The SDSS Collaboration. 2009, <http://www.sdss.org/>
- Tremaine, S. & Gunn, J. E. 1979, *Physical Review Letters*, 42, 407
- Tu, H. et al. 2007, preprint, arXiv:0710.2246 [astro-ph]
- Turner, E. L. 2002, *Nature*, 417, 905
- Umetsu, K. & Broadhurst, T. 2007, preprint, arXiv:0712.3441 [astro-ph]
- Viel, M., Becker, G. D., Bolton, J. S., Haehnelt, M. G., Rauch, M., & Sargent, W. L. W. 2008, *Physical Review Letters*, 100, 041304
- Viel, M., Lesgourgues, J., Haehnelt, M. G., Matarrese, S., & Riotto, A. 2005, *Phys. Rev. D*, 71, 063534
- . 2006, *Physical Review Letters*, 97, 071301
- Vikhlinin, A., Kravtsov, A., Forman, W., Jones, C., Markevitch, M., Murray, S. S., & Van Speybroeck, L. 2006, *ApJ*, 640, 691
- Voigt, L. M. & Fabian, A. C. 2006, *Mon. Not. Roy. Astron. Soc.*, 368, 518

- Watson, C. R., Beacom, J. F., Yüksel, H., & Walker, T. P. 2006, *Phys. Rev. D*, 74, 033009
- Wilkinson, M. I., Kleyana, J. T., Evans, N. W., Gilmore, G. F., Irwin, M. J., & Grebel, E. K. 2004, *ApJ*, 611, L21
- Wolfenstein, L. 1978, *Phys. Rev. D*, 17, 2369
- Wright, E. L. 2004, <http://www.astro.ucla.edu/wright/Lyman-alpha-forest.html>
- Chandra* X-ray Centre. 2009a, CIAO 4.1 Science Threads, <http://cxc.harvard.edu/ciao/threads/all.html>
- . 2009b, CIAO 4.1 Science Threads, http://cxc.harvard.edu/ciao/threads/filter_ltrcv/index.sl.html
- . 2009c, CIAO 4.1 Science Threads, http://cxc.harvard.edu/ciao/threads/spectra_grouping/
- . 2009d, CIAO 4.1 Science Threads, http://cxc.harvard.edu/ciao/threads/detect_overview/
- . 2009e, CIAO 4.1 Science Threads, <http://cxc.harvard.edu/ciao/threads/createL2/>
- . 2009f, CIAO 4.1 Science Threads, <http://cxc.harvard.edu/ciao/threads/acisbackground/index.sl.html>
- Xue, S.-J. & Wu, X.-P. 2002, *ApJ*, 576, 152
- Zavattini, E., Zavattini, G., Ruoso, G., Polacco, E., Milotti, E., Karuza, M., Gastaldi, U., di Domenico, G., Della Valle, F., Cimino, R., Carusotto, S., Cantatore, G., & Bregant, M. 2006, *Physical Review Letters*, 96, 110406
- Zavattini, E., Zavattini, G., Ruoso, G., Raiteri, G., Polacco, E., Milotti, E., Lozza, V., Karuza, M., Gastaldi, U., di Domenico, G., Della Valle, F., Cimino, R., Carusotto, S., Cantatore, G., & Bregant, M. 2008, *Phys. Rev. D*, 77, 032006
- Zhang, Y.-Y., Finoguenov, A., Böhringer, H., Kneib, J.-P., Smith, G. P., Kneissl, R., Okabe, N., & Dahle, H. 2008, *A&A*, 482, 451